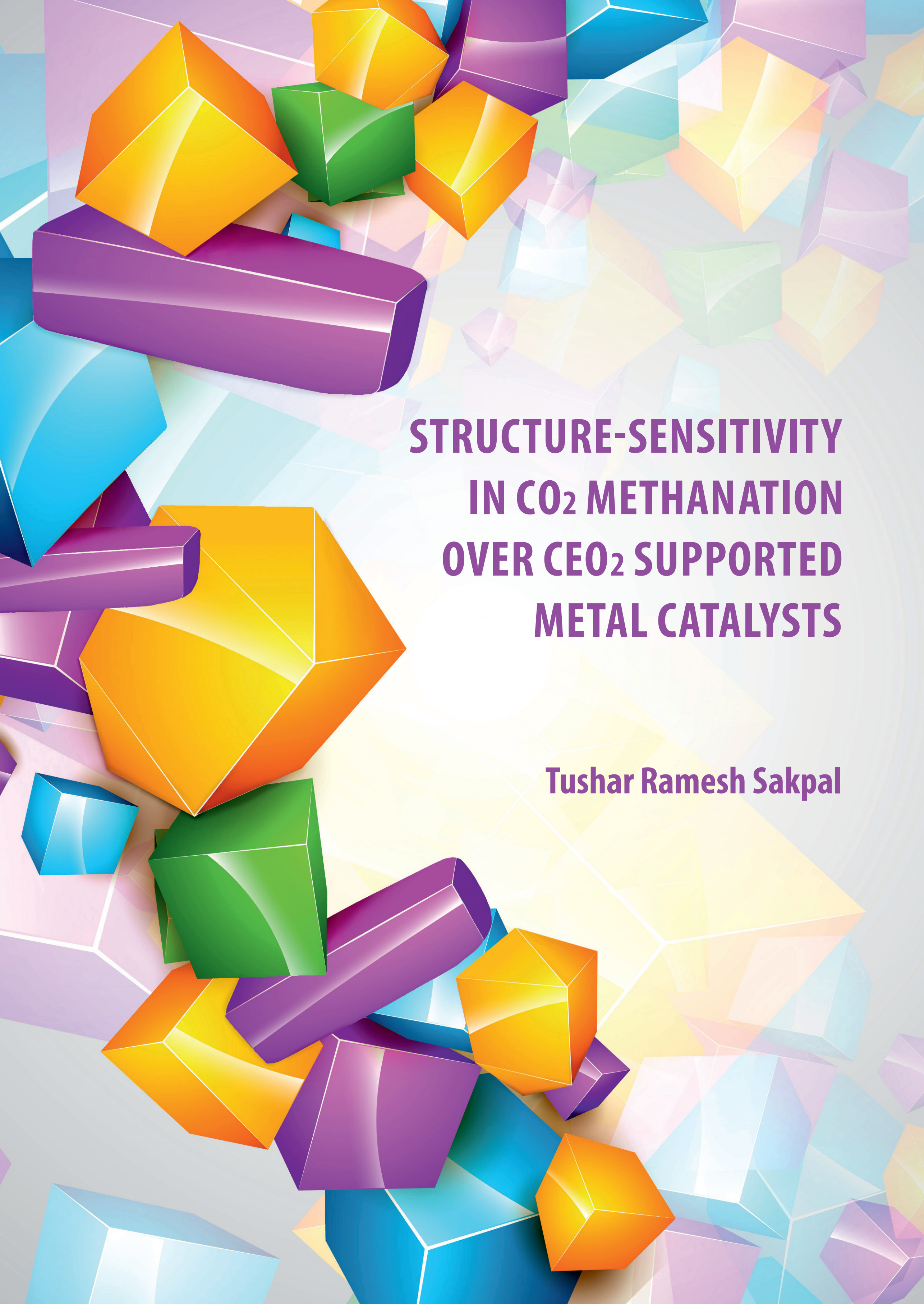

STRUCTURE-SENSITIVITY IN CO_2 METHANATION OVER CEO_2 SUPPORTED METAL CATALYSTS

Tushar Ramesh Sakpal

Structure-sensitivity in CO_2 methanation over CeO_2 supported metal catalysts

Tushar Ramesh Sakpal

Graduation committee:

Chainman: Prof. dr. J. L. Herek	University of Twente
Promoter: Prof. dr. ir. L. Lefferts	University of Twente
Referee: Dr. ir. J. A. Faria Albanese	University of Twente
Prof. dr. ir. J. E. ten Elshof	University of Twente
Prof. dr. G. Mul	University of Twente
Prof. dr. ir. B. M. Weckhuysen	Utrecht University
Prof. dr. ir. E. J. M. Hensen	Technical University of Eindhoven
Prof. dr. J-D. Grunwaldt	Karlsruhe Institute for Technology

The research describe in this thesis was carried out at the Catalytical Processes and Materials (CPM) group of the University of Twente, the Netherlands. This work is part of the research programme "Plasma Power to Gas (PP2G)" with project number 13581, which is financed by the Netherlands Organization for Scientific Research (NWO).

NWO | Applied and Engineering Sciences

Cover design: Tushar Sakpal
Printed by: Gildeprint, Enschede, the Netherlands.

ISBN: 978-90-365-4781-9
DOI: 10.3990/1.9789036547819

Email of the author: tusharsakpal0@gmail.com

Structure-sensitivity in CO_2 methanation over CeO_2 supported metal catalysts

DISSERTATION

to obtain
the degree of doctor at the University of Twente
on the authority of the rector magnificus,
Prof. dr. T.T.M. Palstra,
on account of the decision of the Doctorate Board
to be publicly defended
on Friday 7th June 2019 at 16.45.

by

Tushar Ramesh Sakpal

born on 2nd August 1988
in Pen, Maharashtra, INDIA.

This thesis has been approved by:

Prof. dr. ir. L. Lefferts (promotor)

Table of Contents

Summary

The CO_2 methanation reaction often attracts attention in the energy sector, since combined water electrolysis and methanation can store the surplus renewable electrical energy into chemical energy. This reaction was first introduced in 1902 and has been studied extensively since then. A catalyst is required to obtain a better efficiency of CO_2 methanation reaction. It has been established that Ni and Ru are the best performing metals in terms of activity, selectivity, and stability. Highly dispersed nanoparticles of these metals on support (usually, thermally stable metal oxide) are generally used during the reaction. There are two types of supports, namely reducible supports, and non-reducible supports. Reducible supports (e.g. CeO_2, TiO_2) are more active than non-reducible supports (e.g. Al_2O_3, SiO_2) since they provide additional sites for CO_2 activation.

CeO_2 can easily switch between 4+ and 3+ oxidation without phase change, which results in the formation of abundant oxygen vacancies. As a result of this unique property, CeO_2 supported catalysts show excellent activity for CO_2 methanation reaction compared to other supported catalysts. In the last decade, significant research was done in studying the CeO_2 nano-shapes, with well-controlled crystal planes, such as rods, cubes, and octahedra. Variation in the shape of CeO_2 results in variation in properties and activities of these materials. Previous publications reporting on the effect of CeO_2 morphology on the activity for CO_2 methanation, as well as other reactions, often neglected the effect of metal particle size.

Therefore, this study reports the effect of metal (Ni and Ru) particle size on the activity of catalysts. Moreover, we also studied the morphology effect of CeO_2 nano-shapes by keeping identical metal particle size on all three supports. The thesis is mainly divided into two parts, studying the morphology and particle size effects using Ru/CeO_2 (chapter 2 and 3) and Ni/CeO_2 (chapter 4) catalysts.

In **chapter 1**, the reader is provided with the motivation for renewable-energy storage, possible ways to store energy, fundamentals of CO_2 methanation reaction and properties of materials tested. Last part of chapter summarizes the goals of the thesis.

Chapter 2 compares the performance of rod, octahedra, and cube-shaped CeO_2 supported Ru catalysts, with constant Ru particle size, for CO_2 methanation. Rod-shaped Ru/CeO_2 catalysts exhibit the highest activity of 11.0×10^{-8} mol $s^{-1}m^{-2}_{Ru}$. H_2-TPR, Raman and XPS results reveal that the addition of Ru increases the reducibility of CeO_2, lowering reduction temperature and generating more oxygen vacancies. Diffusion of these oxygen vacancies into bulk is concluded based on H_2-TPR data. Rod-shaped Ru/CeO_2 possess higher oxygen vacancy concentration than cubes and octahedra, after oxidative as well as reductive conditions. The catalyst with the highest activity also possesses maximum oxygen vacancies, implying that the oxidation of CeO_2 via CO_2 adsorption is a rate-determining step of the redox cycle.

In **chapter 3** we studied the effect of Ru particle size on the activity for CO_2 methanation using rod-shaped catalysts. The activity of the catalysts shows a significant effect of Ru particle size, where 4.8nm Ru/CeO_2 catalyst exhibits the highest activity of 0.0045 mol $h^{-1}m^{-2}_{Ru}$ at 215^{o}C. The primary reason behind the structure-sensitivity in Ru/CeO2 catalysts is the particle size of Ru itself. There is also an effect of particle size on the reducibility of CeO_2, contributing to the structure-sensitivity of Ru/CeO_2 catalysts. Dissolution of Ru^{4+} increases with metal loading, while it decreases with increasing reduction temperature. The trend in Ru dissolution agrees well with the trend in activity per Ru surface area, suggesting that the presence of Ru opens a fast pathway to activate CO_2 via formation of a HCOO* intermediate. Therefore, based on chapter 2 and 3, we can conclude that the activity of the catalyst for CO_2 methanation depends on the Ru particle size. Hence, it is required to keep the Ru particle size identical while studying the effect of CeO_2 morphology. Moreover, there are two rate-determining steps influencing the overall reaction rate, one on Ru and one on CeO_2 surface respectively.

Chapter 4 of this book reports the effect of CeO_2 morphology as well as Ni particle size on CO_2 methanation activity using a series of Ni/CeO_2 catalysts. Catalysts with different Ni particle size (2.5-4.7 nm) shows different activity, with 2.9nm Ni catalysts showing the maximum activity of 7.54×10^{-3} mol $h^{-1} m_{Ni}^{-2}$ at 270°C. The highest activity of 2.9nm Ni particles is attributed to the intermediate strength of Ni-CO interaction. The CO is one of the intermediate species formed on the active metal surface during the reaction. With the help of literature, it is established that weak Ni-CO interaction on small Ni particle cause insufficient activation of the CO bond, while CO poisoning is caused on large Ni particles due to the stronger interaction between Ni-CO.

Furthermore, the effect of CeO_2 morphology was studied by keeping identical Ni particle size (3nm). The maximum activity was observed for rods-shaped catalysts. Characterization techniques reveal the presence of two types of oxygen vacancies: ones created by Ni^{2+} dissolution (redox inactive), and ones formed during the reduction process via H-spillover (redox-active). The concentration of redox-active oxygen vacancies increases with increasing NiO loading and Ni/CeO_2 rods showed the highest concentration of oxygen vacancy.

Rod-shaped Ni/CeO_2 exhibits the highest activity as well as possess maximum oxygen vacancies, implying that activation of CO_2 on oxygen vacancies is a rate-determining step. Although, the impact of the Ni particle size of activity also indicates that a hydrogenation step of a carbon-containing species on the Ni surface also influences the overall activity. The presence of two rate-determining steps on Ni/CeO_2 catalysts is consistent with the conclusions for Ru/CeO_2 catalysts, reported in chapter 2 and 3.

Based on this work, we conclude that the CO_2 methanation activity of catalysts influenced significantly by variation in metal (Ni and Ru) particle size. Therefore it is very important to maintain identical metal particle size while comparing the nano-shapes of CeO_2 for CO_2 methanation as well as other reactions.

Samenvatting

De CO_2 methanatie reactie krijgt veel aandacht binnen de energiesector, aangezien het overschot aan duurzame elektrische energie omgezet kan worden in chemische energie doormiddel van water elektrolyse en methanatie. Deze reactie werd voor het eerst geïntroduceerd in 1902 en sindsdien is CO_2 methanatie uitgebreid bestudeerd. Een katalysator is nodig voor een energie-efficiënte CO_2 methanatie reactie. Het is bekend dat Ni en Ru de beste metalen voor CO_2 methanatie zijn in termen van activiteit, selectiviteit, en stabiliteit. Nanodeeltjes van deze metalen met een hoge dispersie op een drager (vaak een thermisch stabiele metaal oxide) worden veelal gebruikt gedurende de reactie. Er zijn twee soorten dragers, namelijk reduceerbare dragers, en niet-reduceerbare dragers. Reduceerbare dragers (zoals CeO_2, TiO_2) zijn meer actief dan niet-reduceerbare dragers (zoals Al_2O_3, SiO_2), aangezien deze additionele plekken voor CO_2 activatie verschaffen.

CeO_2 wisselt gemakkelijk tussen de 4+ en 3+ oxidatiestaten zonder een fase verandering, hetgeen resulteert in de formatie van grote hoeveelheid zuurstof deficiënties. Een resultaat van deze unieke eigenschap is dat CeO_2 gedragen katalysatoren een erg hoge activiteit voor CO_2 methanatie geven in vergelijking met andere gedragen katalysatoren. In de afgelopen tien jaar zijn er veel studies gedaan met verschillende CeO_2 nano-structuren, met goed gecontroleerde kristal facetten, zoals staven, kubussen, en achtkantige structuren. De variatie in de CeO_2 structuren resulteert in een variatie in eigenschappen en activiteiten van deze materialen. Voorgaande publicaties hebben gerapporteerd over het effect van de CeO_2 morfologie op de activiteit voor CO_2 methanatie, evenals voor andere reacties, waarbij veelal het effect van de deeltjesgrootte van het metaal wordt verwaarloosd.

Vandaar rapporteert deze studie het effect van de deeltjesgrootte van het metaal (Ni en Ru) op de activiteit van de katalysatoren. Bovendien hebben we het effect van de morfologie van de CeO_2 nano-structuren bestudeerd met identieke deeltjesgrootte van de metalen op de drie dragers. Het proefschrift is verdeeld in twee delen, namelijk de studie van de morfologie en de deeltjesgrootte van het metaal voor Ru/CeO_2 (hoofdstuk 2 en 3) en Ni/CeO_2 (hoofdstuk 4) katalysatoren.

In **hoofdstuk 1** krijgt de lezer een motivatie omtrent duurzame energie opslag, de mogelijke manieren om energie op te slaan, een achtergrond van de CO_2 methanatie reactie, en de eigenschappen van de eigenschappen van de geteste materialen. In het laatste deel van het hoofdstuk worden de doelen van de thesis samengevat.

In **hoofdstuk 2** wordt de activiteit van Ru katalysatoren gedragen op staven, kubussen, en achtkantige structuren van CeO_2 vergeleken voor CO_2 methanatie met een constante Ru deeltjesgrootte. Ru/CeO_2 katalysatoren met een staaf-structuur geven de hoogste activiteit van 11.0×10^{-8} mol $s^{-1}m_{Ru}^{-2}$. De H_2-TPR, Raman en XPS resultaten onthullen dat de toevoeging van Ru de reduceerbaarheid van CeO_2 verhogen, hetgeen de reductietemperatuur verlaagt, terwijl het aantal zuurstof deficiënties toeneemt. De diffusie van zuurstof deficiënties naar de bulk is vastgesteld aan de hand van H_2-TPR data. Ru/CeO_2 katalysatoren met staaf-structuren bevatten hogere zuurstof deficiëntie concentraties dan kubussen en achtkantige structuren, zowel na oxiderende als na reducerende condities. De katalysatoren met de hoogste activiteit hebben ook de maximale hoeveelheid zuurstof deficiënties, hetgeen impliceert dat de oxidatie van CeO_2 via CO_2 adsorptie de snelheidsbepalende stap is in de redox cyclus.

In **hoofdstuk 3** hebben we het effect van de Ru deeltjesgrootte on de activiteit voor CO_2 methanatie bestudeerde voor katalysatoren met staaf-structuren. De activiteit van de katalysatoren vertoont een sterk verband met de Ru deeltjesgrootte, waarbij de 4.8nm Ru/CeO_2 katalysator de hoogste activiteit vertoont (0.0045 mol $h^{-1}m_{Ru}^{-2}$ bij een temperatuur van 215°C). De voornaamste reden voor de structuur-sensitiviteit voor Ru/CeO_2 katalysatoren is de deeltjesgrootte van Ru. Verder is er een effect van de deeltjesgrootte op de reduceerbaarheid van CeO_2, hetgeen bijdraagt aan de structuur-sensitiviteit van Ru/CeO_2 katalysatoren. De oplossing van Ru^{4+} neemt toe met metaal belading, terwijl dit afneemt met toenemende reductietemperatuur. De trend in oplossing van Ru is in overeenstemming met de activiteit per Ru oppervlakte, hetgeen de suggestie wekt dat de aanwezigheid van Ru een versneld pad naar de activatie van CO_2 verschaft via de formatie van een HCOO* tussenproduct. Gebaseerd op hoofdstuk 2 en 3 kunnen we concluderen dat de activiteit van de katalysator voor CO_2 methanatie afhankelijk is van de Ru deeltjesgrootte. De Ru deeltjesgrootte moet dus constant gehouden worden wanner het effect van de CeO_2 morfologie wordt bestudeerd. Daarnaast zijn er twee snelheidsbepalende stappen die de totale reactiesnelheid bepalen, één over Ru en één over het CeO_2 oppervlak.

In **hoofdstuk 4** van dit proefschrift wordt het effect van de CeO_2 morfologie en de Ni deeltjesgrootte voor de CO_2 methanatie activiteit gerapporteerd, met een serie Ni/CeO_2 katalysatoren. Katalysatoren met verschillende Ni deeltjesgrootte (2.5-4.7 nm) vertonen verschillende activiteiten, waarbij 2.9nm Ni katalysatoren de hoogste activiteit vertonen met een maximale activiteit van 7.54×10^{-3} mol $h^{-1}m_{Ni}^{-2}$ op een temperatuur van 270°C. De hoogste activiteit van 2.9nm Ni deeltjes kan worden toegeschreven aan de gemiddelde sterkte van de Ni-CO interactie. CO is een van de tussenproducten gevormd op het oppervlak van het actieve metaal tijdens de reactie. Met de hulp van literatuur kan het worden vastgesteld dat een zwakke Ni-CO interactie op kleine Ni deeltjes voor onvoldoende activatie van de CO bond zorgt, terwijl te sterk geadsorbeerde CO op grote Ni deeltjes wordt veroorzaakt door een sterkere Ni-CO interactie.

Verder is het effect van de CeO_2 morfologie onderzocht met een constante Ni deeltjesgrootte (3nm). Katalysatoren met staaf-structuren gaven de hoogste activiteit. Verschillende karakterisatie-technieken leggen bloot dat er twee soorten zuurstof deficiënties zijn: één gevormd tijdens N^{2+} oplossing (redox-inactief), en één gevormd tijdens het reductieproces via H-overloopeffecten (redox-actief). De concentratie van redox-actieve zuurstof deficiënties neemt toe met toenemende NiO lading en Ni/CeO_2 met staaf-structuren hebben de hoogste concentraties van zuurstof deficiënties.

Ni/CeO_2 met staaf-structuren hebben de hoogste activiteit en de hoogste concentratie van zuurstof deficiënties, hetgeen impliceert dat de activatie van CO_2 op zuurstof deficiënties de snelheidsbepalende stap is. Echter, de afhankelijkheid van de Ni deeltjesgrootte voor de activiteit geeft een indicatie dat ook de hydrogenatie stappen van de koolstof-houdende stoffen op het Ni oppervlak de algehele activiteit beïnvloeden. De aanwezigheid van twee snelheidsbepalende stappen over Ni/CeO_2 katalysatoren is consistent met de conclusies voor de Ru/CeO_2 katalysatoren, zoals gerapporteerd in hoofdstuk 2 en 3.

Op basis van dit werk kunnen we concluderen dat de CO_2 methanatie activiteit van katalysatoren significant wordt beïnvloed door de variatie in metaal (Ni en Ru) deeltjesgrootte. Het is dus erg belangrijk om de metaal deeltjesgrootte identiek te houden wanneer verschillende nano-structuren van CeO_2 vergeleken worden voor de CO_2 methanatie reactie, evenals voor andere reacties.

Chapter 1

General Discussion

Abstract

The scope of this chapter is to give a broad overview of this thesis, including the motivation for renewable-energy storage, possible ways to store energy, fundamentals of CO_2 methanation reaction and properties of materials tested. Substitution of energy generation using coal, oil, and natural gas is a must and renewable sources (wind and solar) is the best-known solution for it. These sources are sustainable, but at the same time they are intermittent, requiring efficient energy storage. The surplus electricity can be stored as chemical energy in the form of methane, which can be easily liquefied, stored safely, and distributed using existing infrastructure. For the efficient conversion of electricity to methane, a catalyst with high activity, selectivity and stability is required. The fundamental understanding of the role of catalysts in the CO_2 methanation reaction is compulsory to achieve highly efficient catalysts. Keeping this in mind, this study focuses on the role of the morphology of support material and particle size of metal on the performance of catalysts. Various properties such as reducibility, oxygen vacancies, and metal particle size are studied to explore the structure-dependent activity of CeO_2 based catalysts. The mechanisms for CO_2 methanation on CeO_2-supported catalysts is also presented. The chapter ends with the scope and outline of the thesis.

1.1. Renewable energy and its storage

It is well-known that fossil fuels are depleting and are the main source of anthropogenic global warming. On the other hand, nuclear energy also has unsolved problems like waste disposal. Carbon capture and storage (CCS) minimizes the greenhouse gas (GHG) emission to a certain extent, hence it cannot reduce fossil fuel dependency. The CO_2 concentration in the atmosphere has already reached the 400ppm mark, therefore energy production with zero carbon emission is requisite.

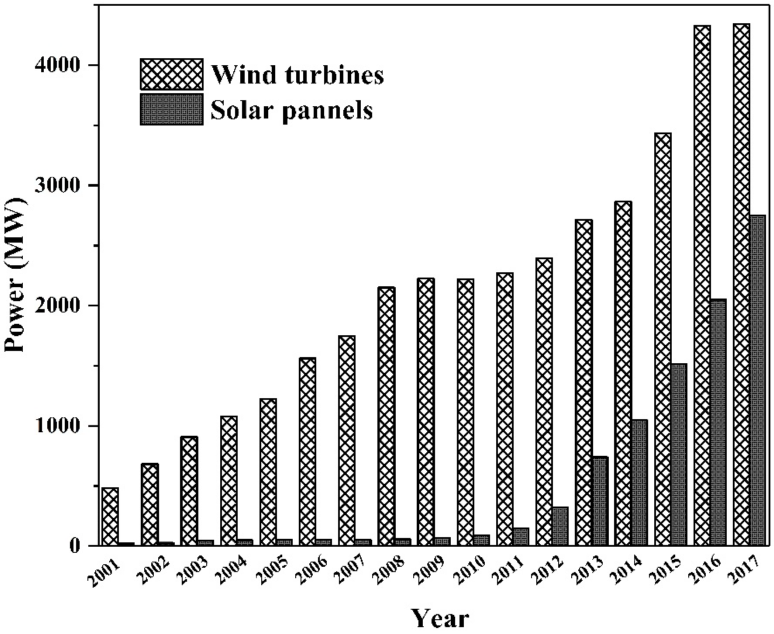

Figure 1.1: Year-wise production of wind and solar energy (cumulative) in the Netherlands (source: GWEC Global Wind Report 2017 and Wikipedia).

Energy production from renewable sources (e.g. wind and solar) emerges as a potential candidate to replace the existing fossil fuels. The roadmap of the European Commission for 2020 has set the goal of 20% of renewable energy in the overall energy mix, which increases to 27% in 2030 (1). Thus, renewable energy sources are going to play a key role in electric power generation. In the Netherlands as well, electricity production from wind and solar has been increased significantly in the last 15 years (Figure 1.1). Although, the electricity generation from renewable sources is often fluctuating. Hence, an efficient way to store this surplus energy is requisite.

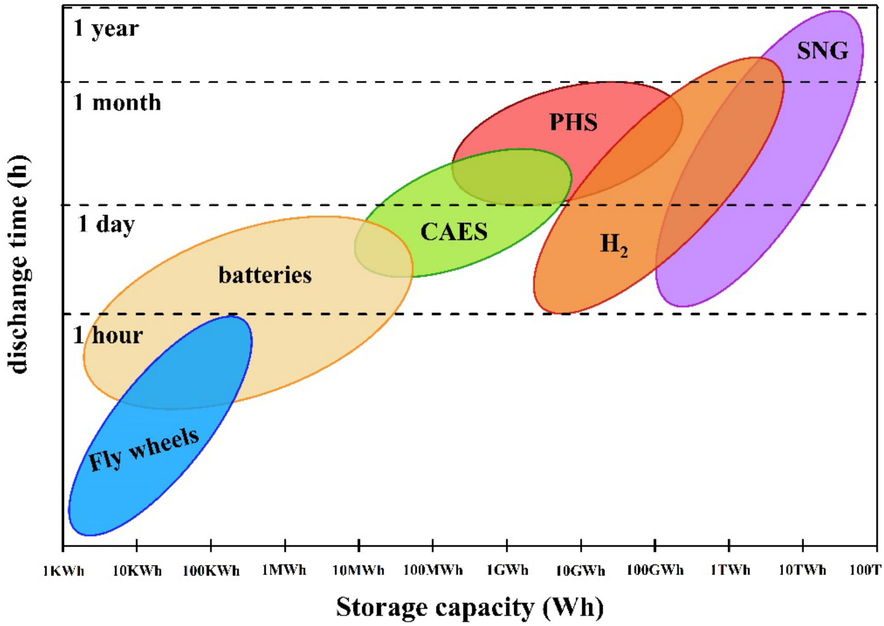

Figure 1.2: Charge/discharge period and the storage capacity of different electricity storage systems. CAES: compressed air energy storage, PHS: pumped hydro storage, SNG: synthetic natural gas. Reproduced from reference 2.

The surplus energy from renewable sources can be stored as potential energy (Pumped Hydroelectric Storage), mechanical energy (Compressed air reservoir or flywheel energy system) or chemical energy (batteries) (2). Furthermore, electrical energy can be converted into chemical energy by transferring it into fuels such as hydrogen, synthetic natural gas (SNG), or methanol (3). The comparison of these technologies in terms of storage capacity and discharge time is shown in figure 1.2. It is obvious from the figure that the conversion of energy into fuels is the potential option to store energy in large quantity for a longer period of time.

Power-to-Methane (PtM, Figure 1.3) is a concept that converts electricity into chemical energy using CO_2 and H_2O. The concept brings the possibility of connecting the power grid to different sectors where CH_4 is needed, such as mobility and industry (4). The conversion of electricity into chemical energy via water electrolysis to produce H_2 is the first part of the PtM process chain (5). The dissociation of water using plasma (generated by renewable electricity) is another alternative to water electrolysis (6) since plasma dissociation is a highly efficient process that can produce H_2 at a lower price than conventional electrolysis, also it does not require the water to be purified (ref). In the second conversion step of the PtM process chain, CH_4 is formed by the reaction of H_2 with CO_2. In the methanation process, H_2 and CO_2 are converted to CH_4 and H_2O, which can be carried out chemically using a catalyst or biologically using highly specialized microorganisms such as Archaea (ref).

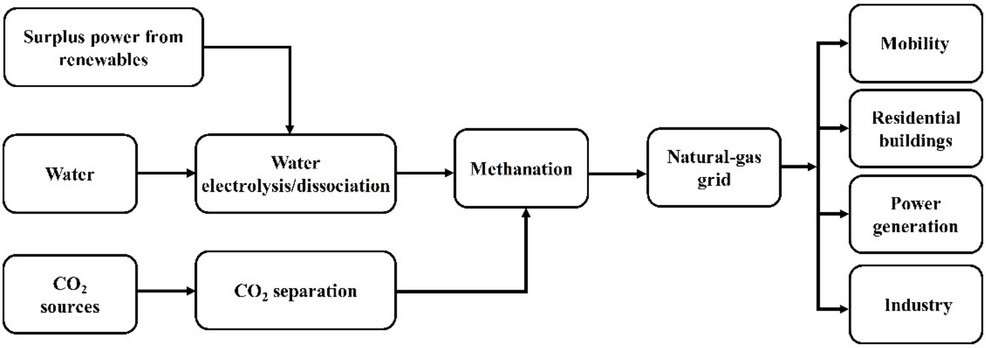

Figure 1.3: Principle of the power-to-methane concept and its applications. Adapted from reference 4.

1.2. Catalytic CO_2 methanation

CO_2 methanation, also known as the Sabatier reaction, was first introduced in 1902 by French scientist Paul Sabatier and it has been studied extensively thereafter. Apart from its use in the energy sector, the reaction also has an application in reclaiming oxygen in the International Space Station via electrolysis of water.

$$CO_2 + 4H_2 \rightarrow CH_4 + 2H_2O \qquad \Delta H\ (298K) = -164.75 kJ/mol$$

1.2.1. Thermodynamic analysis

CO_2 methanation is a highly exothermic reaction. The thermodynamic analysis of CO_2 hydrogenation was performed using the Gibbs free energy minimization method available from the HSC

Chemistry. As shown in figure 1.4, all the results are presented in terms of the mole equilibrium fraction of each component. It can be concluded from the figure that the methanation process is favorable at the low reaction temperature, high pressure, and high H_2/CO_x ratio (7). Also, above 600°C, the formation of CO via reverse water gas shift reaction dominates over CH_4. Meanwhile, the formation of carbon deposits can be prohibited to a great extent.

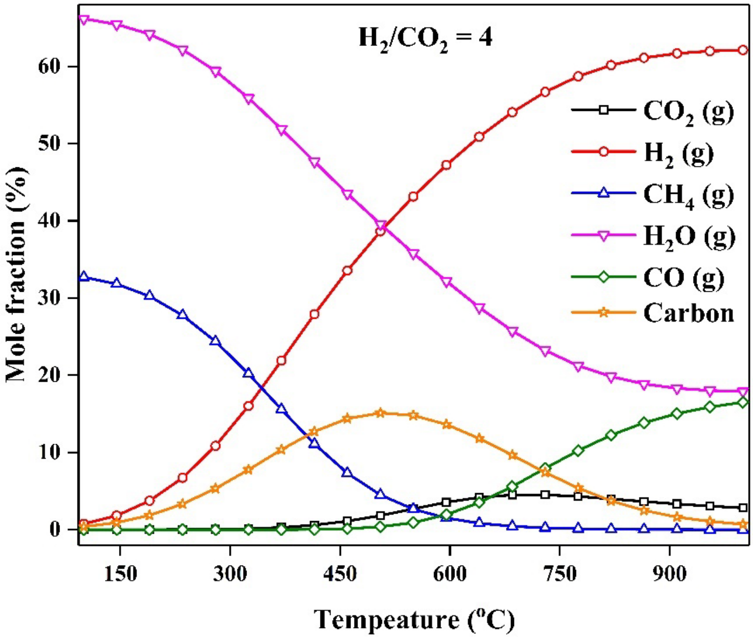

Figure 1.4: The equilibrium composition of components as a function of reaction temperature in the CO_2 hydrogenation reaction at 1 bar pressure. Values were calculated using HSC Chemistry 6 software and applying the Gibbs free energy minimization method.

1.2.2. Catalysis

1.2.2.1. Classical catalysis

Even though the Sabatier reaction is thermodynamically favorable, it has significant kinetic limitations as it occurs through an eight-electrons process (7). Therefore, a catalyst is required to overcome these kinetic barriers. Noble metals such as Ru, Rh, and

Pd supported on metal oxide (e.g., TiO_2, Al_2O_3, CeO_2) are active for this reaction at mild operating conditions (8, 9). However, noble metals are expensive which makes them less attractive for practical applications (10). Non-noble metal catalysts are best substitutes for above-mentioned catalysts since they have comparable activity to noble metals with lower cost (11, 12). Graf et. al. (13) reported Ru and Ni are the most active and selective metals for CO_2 methanation.

The catalytic activity can be influenced by different properties including the support material. Hence, selection of the right carrier for active metal is an important factor to achieve efficient catalysts for CO_2 methanation. Different supports, including aluminium oxide (Al_2O_3) (14), silicon dioxide (SiO_2) (15), zirconium dioxide (ZrO_2) (16), cerium oxide (CeO_2) (17), lanthanum oxide (La_2O_3) (18), magnesium oxide (MgO) (19), titanium dioxide (TiO_2) (20), carbon materials (21), and zeolites (22), have been reported previously for this reaction. Kowalczyk et al. (23) studied the effect of different supports on the activity of Ru catalysts for CO_2 methanation and obtained following order of TOFs ($x10^3$ s^{-1}): Ru/Al_2O_3 (16.5) > Ru/$MgAl_2O_4$ (8.8) > Ru/MgO (7.9) > Ru/C (2.5). In another study (24), Gao et.al. reported the CO_2 methanation activity over Ni catalysts supported on mesoporous materials, decreasing on the order Ni/ZSM-5 > Ni/SBA-15 > Ni/Al_2O_3 > Ni/MCM-41.

Deactivation of catalysts during CO_2 methanation can occur due to sintering, fouling or poisoning (25). Sintering is the most common cause of deactivation where catalysts lose its active surface area due to agglomeration of metal nanoparticles. This is possible when catalysts experience high temperatures for a long period of time. Another cause of catalysts deactivation is blocking of the active metal surface by means of carbon, this phenomenon is known as coking. Active sites can also be blocked by gaseous species as well, via irreversible adsorption, decreasing the activity of catalysts. This phenomenon is referred as poisoning of catalysts (26).

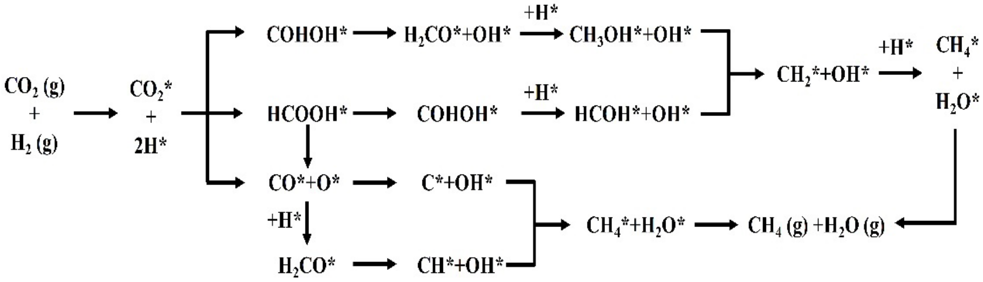

Figure 1.5: Representatives of proposed reaction schemes for the conversion of CO_2 to CH_4. Adapted from reference 27. * represent active site on metal.

Even after extensive research, the mechanism for this reaction is still under debate. Su et. al (27) reported the general mechanism involving all different routes and intermediates (Figure 1.5). The reaction mechanism has been classified into two categories. The first one, called the CO route, involves the formation CO* and O* (Figure 1.5) and subsequently following the CO methanation mechanism. The other mechanism, called formate route, involves the formation formate (HCOOH*, Figure1.5) as the main intermediate which then dissociates to C via CO before hydrogenating to CH_4. Figure 1.5 presents the general mechanism of CO_2 methanation on metal catalysts supported on non-reducible oxides, where adsorption of reactants and generation of intermediates takes place on the metal surface. The mechanism of CO_2 methanation on metal catalysts supported on reducible oxides is discussed later in this chapter.

1.2.2.2. Single-atom catalysis

Figure 1.6 shows that the electronic and geometric structures of a single atom are different than that of metal clusters or nanoparticles (28). Catalysts containing isolated atoms or metal ions dispersed on solid supports are known as single atom catalysts (SAC). Reducible supports like CeO_2 and TiO_2 are used for synthesizing and stabilizing single atoms sites. SAC with Al_2O_3 and carbon-based materials are also known (28). Single-atom catalysts have been shown to be highly active in a variety of chemical reactions including water gas shift, oxidation, selective hydrogenation, and photocatalysis (29, 30). Although, study about SAC for CO_2 methanation is still limited due to the fact that SAC have low activity than supported nanoparticles for CO_2 methanation activity (31, 32). Guan et. al. (31) used spectroscopic characterization tools to propose that the H_2 dissociation is not favorable on isolated Rh atoms, and this leads to low CO_2 methanation activity of Rh/TiO_2 catalysts. Liu et. al. (32) used theoretical calculations to report that the geometric structures of Cu_4 clusters are different than conventional Cu nanoparticles, which make Cu_4 clusters unfavorable for CO_2 methanation due to higher activation barrier.

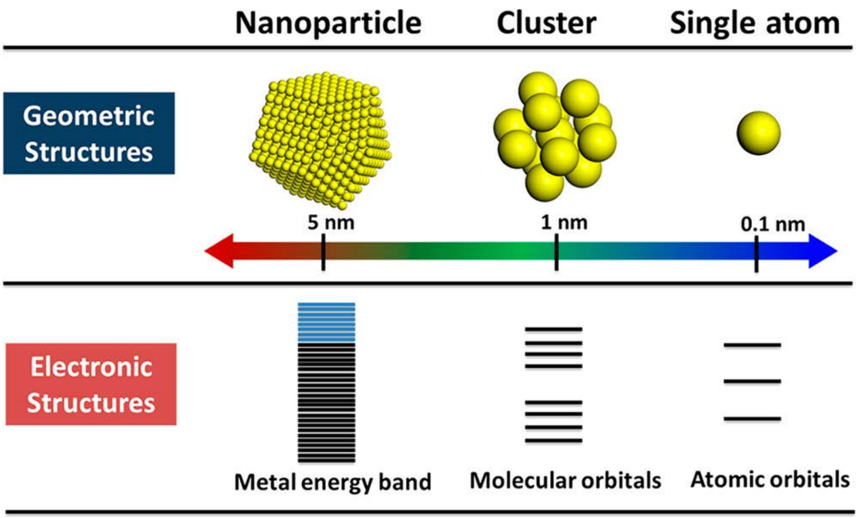

Figure 1.6: Geometric and electronic structures of a single atom, clusters, and nanoparticles. Reproduced from reference 28.

1.3. CeO_2

Focus on cerium oxide (CeO_2), also known as cerium dioxide or ceria, as a catalytic material has increased significantly due to its fundamental interest and potential commercial applications. Figure 1.7 shows the increasing number of publications per year, since 1998, in the field of “CeO_2” and “CeO_2 + catalysis”. The state-of-the-art in the field of CeO_2 catalysis has been discussed in several review articles (33-41). Also, there are many original research articles about CeO_2 are available in the field of energy and environment processes, biology (42) and medicine (43). Further, we will provide the reader with a general view on the properties of CeO_2-based materials and their various applications.

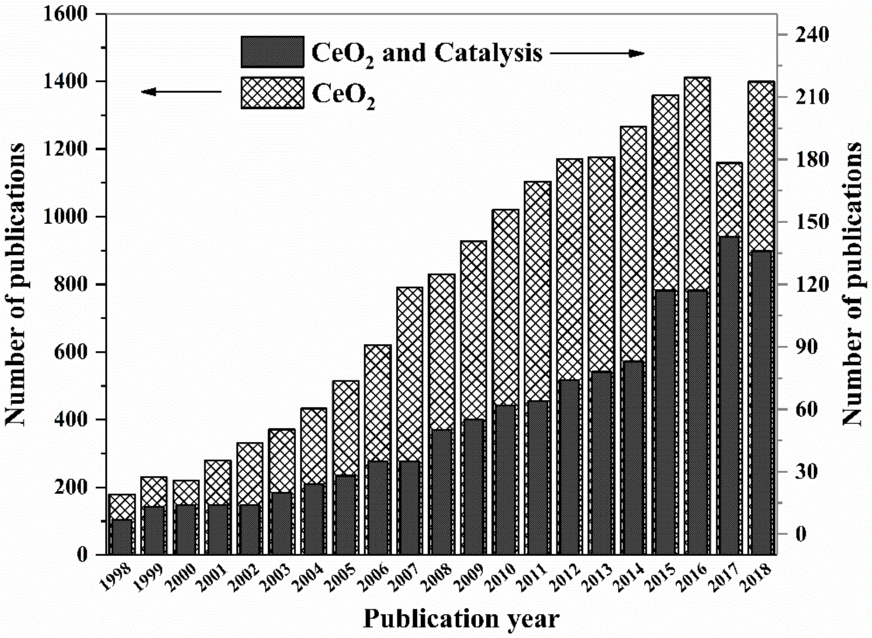

Figure 1.7: Histogram of the number of publications on CeO_2 and publications on CeO_2 associated with catalysis from 1998 to 2018 (Source: Web of Science)

CeO_2 has an important role in two of the most important commercial catalytic processes in terms of economic relevance and capacity: three-way catalysis (TWC) and fluid catalytic cracking (FCC) (44). The role of CeO_2 in three-way catalysts (TWC) for the control of gaseous exhaust emissions has variously been described as (a) oxygen storage under transient conditions; (b) catalytic promoter of precious metals for certain reactions such as water gas shift; (c) structural promoter for the stabilization of precious metals and alumina against particle growth (45). In FCC processes, CeO_2 is used to depollute the noxious compounds, such as Sox, from gaseous streams. CeO_2 is also one of the most valuable catalysts for the oxidation of carbon soot from diesel engine exhaust (46) and for the removal of organics from wastewaters (catalytic wet oxidation) (44).

1.3.1. Structural and non-stoichiometric properties

CeO_2 is pale yellow/white colored cerium compound, formed via calcination of cerium oxalate or hydroxide. It is commonly used as a catalyst or a carrier of catalysts. CeO_2 has fluorite (CaF_2) crystal structure with Fm3m space group in its fully oxidized form (47). Figure 1.8 shows that the Ce cations are arranged in a face-centered cubic structure while the O anions are embedded within the unit cell in a simple cubic arrangement. The Ce cations are bonded to eight O nearest neighbors while the O anions are tetrahedrally bonded to four Ce nearest neighbors.

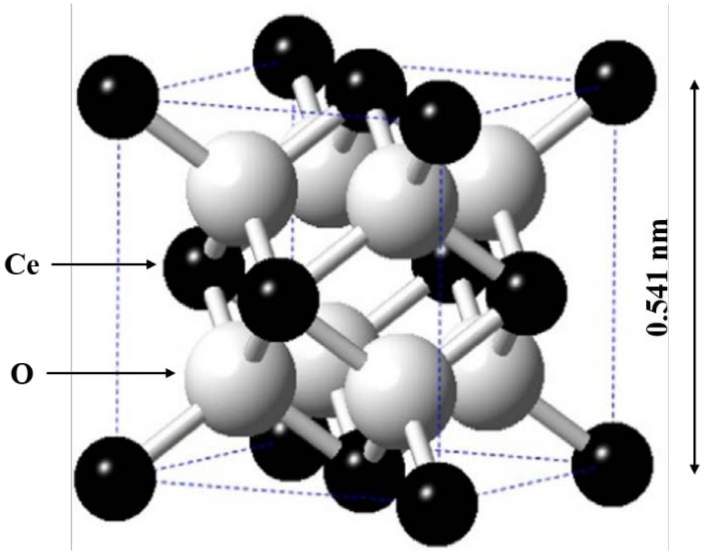

Figure 1.8: The unit cell of CeO_2. The black spheres are Ce and the white spheres are O. Note that the spheres have been drawn at 50% space-filling so that the Ce–O bonding could be shown. Re-produced from reference 48.

A number of different phases can be formed using cerium and oxygen, which depends on temperature and oxygen pressure. CeO_2

can release oxygen from its lattice to reduce Ce(IV) to Ce(III), which leads to the formation of non-stoichiometric CeO_{2-x} with oxygen vacancies within the crystal structure. Fully reduced CeO_2 can form sesquioxide (Ce_2O_3), which has a hexagonal structure with P3ml space group. In this structure, the Ce cations are coordinated to seven O anions, with four oxygen closer than the other three. The reaction can be expressed, following the Kröger-Vink notation (equation 1) as,

$$2Ce_{Ce}+O_{O}\rightarrow V_{O}^{\blacksquare\blacksquare}+2Ce_{Ce}^{'}+\frac{1}{2}O_2 \text{ .... (1)}$$

1.3.2. Solid solutions of CeO_2

The fluorite structure of CeO_2 can form a solid solution with different oxides. Mixing of CeO_2 with other isovalent/aliovalent cations changes many of it's bulk and surface properties, as it stabilizes the surface area and crystallite size of pure CeO_2 (36, 49). Furthermore, the doping of CeO_2 also facilitates the formation of more oxygen vacancies, enhanced oxygen mobility and ionic conductivity (50, 51). The most commonly used cations to form solid solutions are Zr (52), Ti (53), and Mg (54).

1.3.3. Redox properties and OSC

The unique property of CeO_2 to switch between its two most stable oxidation state, i.e. between Ce^{3+} and Ce^{4+}, is known as oxygen storage capacity (OSC). OSC measurements generally help to evaluate the redox properties of metal catalysts supported on reducible oxides. Simple techniques such as temperature programmed reductions (TPR) and re-oxidation can be used to get detailed information about total OSC. Addition of metal nanoparticles to the support is known to have an enhancing effect on the OSC of catalysts, reducing the surface of CeO_2 via H-spillover, generating abundant oxygen vacancies (55).

1.3.4. Nanostructured CeO_2

Preparation of CeO_2 nanostructures with controlled morphology is studied extensively in last decade and there are plenty of reports published, claiming improvement in the activity of CeO_2 catalysts due to its morphology (56, 57). This improved activity is caused by the exposure of well-defined crystal planes of nano-shaped CeO_2. The most stable form of CeO_2 crystal plane is (111), while CeO_2 with less stable (110) and (100) terminations are also reported (36, 39, 58). Furthermore, the energy of formation of oxygen vacancies on different surface planes of CeO_2 vary, following the order (110) < (100) < (111) (59).

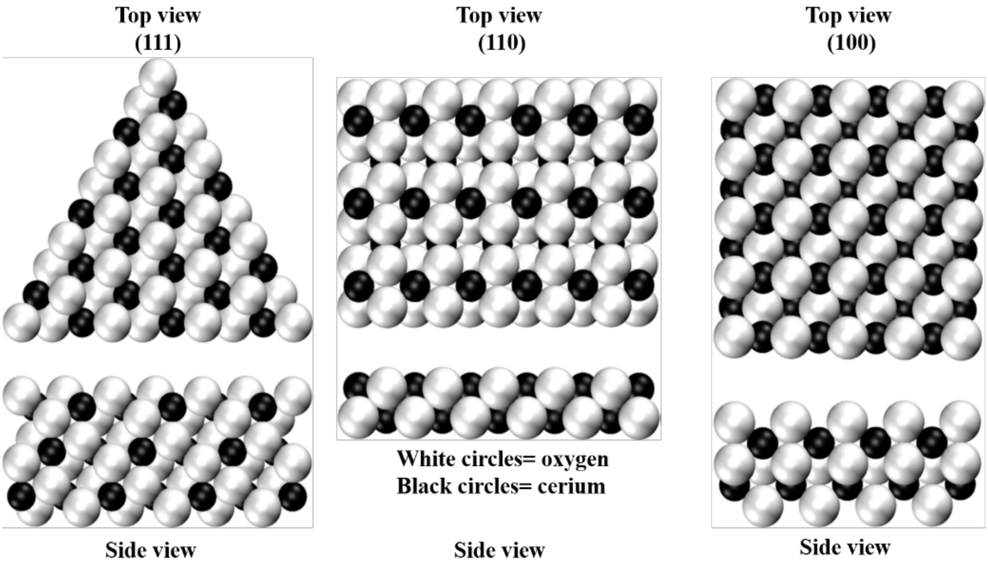

Figure 1.9: CeO_2 (111), CeO_2 (110), and CeO_2 (100) depicted as an unreconstructed Tasker Type 1 surface (60). The black spheres are Ce and the white spheres are O. The spheres have been drawn at 100% space-filling to indicate accessibility to subsurface sites. Reproduced from reference 48.

Three most common low-indexed lattice planes of CeO_2 are presented in figure 1.9. The (111) plane of CeO_2 has an open structure with a top layer of oxygen followed by an accessible cerium layer. On the other hand, the (110) plane of CeO_2 contains both cerium and oxygen atoms in the top layer. Whereas, CeO_2 (100) plane is oxygen terminated while cerium is positioned below the oxygen layer, making cerium inaccessible. This makes the (100) surface polar and unstable (61, 62). Different planes have different numbers of nearest bonded neighbors for Ce and O on the exposed surface. For example, in the (111) plane, Ce:O coordination number is 7:3; while for (110) and (100), it is 6:3 and 6:2, respectively (63). The different coordination numbers lead to differences in the relative stability of these surfaces, decreasing in the order (111) > (110) > (100).

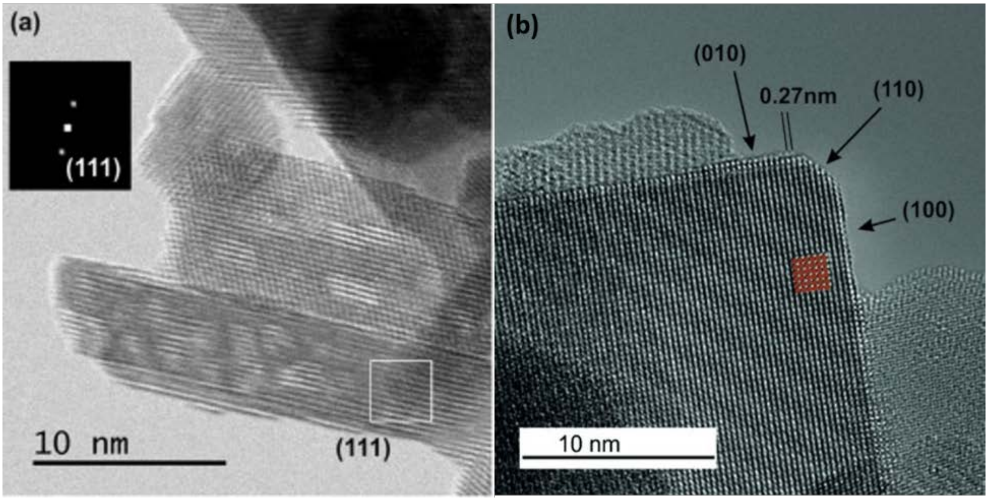

Figure 1.10: Aberration-corrected TEM images of (a) CeO_2 rods and (b) cubes. Reproduced from reference 64.

In the last decade, researchers have successfully achieved control over the morphology of CeO_2, resulting in different shapes such as cubes, rods, wire, tubes, and spheres (65, 66, 67). These shapes of CeO_2 are known to expose different crystal plane on the surface. The most studied nano-shapes of CeO_2, i.e. rods and cubes, for different catalytic reactions are shown in figure 1.10. Generally, CeO_2 rods and cubes expose (111) and (100) facets, respectively. Although, there is no general agreement about the assignment of these planes to the specific shape of CeO_2.

1.3.5. Applications

Due to the unique property to switch between Ce^{3+} and Ce^{4+}, CeO_2 and CeO_2 based materials are studied extensively for a variety of reaction, including CO oxidation, CO_2 hydrogenation, and the production of hydrogen via water gas shift and reforming reactions. A brief overview of these studies is tabulated at the end of this chapter (Table S1.1).

1.3.5.1 CO oxidation

CO oxidation has great technological importance in the field of pollution control and fuel cells. Its main utility lies in the removal of carbon monoxide (CO) from the fuel cell's feed gas; the process is known as preferential oxidation (PROX). The Pt/CeO_2 catalyst shows excellent activity for this reaction (68, 69) since the electronic properties of Pt are affected by the interaction with CeO_2 which improves its catalytic activity (68). On Pt/CeO_2, a strong interaction with the CeO_2 support under oxidative conditions leads to partial oxidation of the Pt particles while Pt reduced under excess CO feed to give maximum activity (68). The co-deposition of Pt and CeO_2 nanoparticles on TiO_2 (110) produces catalysts with extreme activity for CO oxidation, due to a very active Pt/CeO_2 interface (70, 71).

The major drawback of noble metal catalysts is fast deactivation during the reaction (72), therefore non-noble metals have attracted a lot of attention in the last few years. Among non-noble metal catalysts, copper supported on the CeO_2 has been reported most active catalysts, for oxidation of CO in hydrogen-rich (PROX) (73) and regular streams (74, 75). The important factor which decides the activity of CeO_2-based catalysts is the existence of Ce^{3+} sites at the oxide-metal interface, binding O atoms weaker than the Ce^{3+} sites of bulk CeO_2 (76).

1.3.5.2 Water Gas Shift (WGS)

Water gas shift, in combination with CO oxidation, is a critical reaction in order to achieve clean hydrogen (77). CeO_2 can dissociate water on the oxygen vacancies or Ce^{3+} sites and hence CeO_2 supported metal (Au, Cu, Ni, and Pt) catalysts are proved to be excellent catalysts for WGS (78, 79, 80). The activity of Pt/CeO_2 was found higher compared to Cu/CeO_2 and Au/CeO_2 catalysts at low metal loading (79). Although, the trend in activity was reversed at high metal loading. It was suggested that metal-support interactions prevent carbon formation and enhance the forward WGS on Pt/CeO_2 (111) at low Pt loading (79). The strong metal support interaction is also observed for Ni/CeO_2 (111) catalysts, which suppresses the ability of Ni to perform the CO methanation reaction and favor the WGS process (80).

1.3.5.3 Methanol synthesis

Methanol is a key material in the chemical industry since it can be used to synthesize liquid fuels such as hydrocarbons and dimethyl ether. Many catalysts have been developed and tested for this reaction in recent time. Traditionally, Cu/ZnO catalysts are used for this reaction, but highly active $Cu–CeO_2$ and $Cu–CeO_2–TiO_2$ catalysts as an efficient alternative are also reported recently (82). This suggests that the metal surface is not the only active site and CeO_2 surface also acts as an active site which enhances the catalytic activity of methanol synthesis. This to some extent also highlights the fundamental role of the metal/oxide interface as the active site (81).

1.3.5.4 Dry reforming of methane (DRM)

DRM, also known as CO_2 reforming of methane, is an interesting route to convert two greenhouse gases to synthesis gas. Wang et. al. (83) used CeO_2 as a promoter to improve the catalytic activity, stability, and carbon resistance of catalysts. Researchers have also studied the strong metal support interaction in the Ni/CeO_2 system (84). If the nickel particles are flattened and strongly stabilized on the partially reduced CeO_2 surface under strongly reducing conditions, it results in enhanced stability for CO_2 reforming of CH_4 (84). Even though CeO_2-based catalysts had shown high catalytic activities for DRM reaction, further development of superior catalyst with high carbon resistance, is urgently needed to satisfy the demands of the industrial application.

1.3.5.5 CO_2 methanation

Ru and Ni supported on CeO_2 are the most effective catalysts for this reaction. Tada et.al. (85) have reported that Ni supported on CeO_2 are more active than Ni supported on α-Al_2O_3, TiO_2, and MgO. Generally, on supports like alumina and silica, activation of CO_2 and H_2 happens on the active metal surface. However, it is also reported that CeO_2 can act as an active site of CO_2 activation while the active metal surface acts as a supplier of atomic hydrogen (86, 87, 88, 89). Pan et. al (90) found higher CO_2 methanation activity for $Ni/Ce_{0.5}Zr_{0.5}O_2$ compared to γ-Al_2O_3 supported nickel catalysts. It is suggested that $Ce_{0.5}Zr_{0.5}O_2$ provides unique medium basic sites for CO_2 adsorption and subsequent conversion to carbonate and monodentate formate, which undergo hydrogenation more quickly than bidentate formate (90).

Doping CeO_2 with other metals is an effective approach to improve its reduction degree and the concentration of oxygen vacancies. Ocampo et. al. (91) observed improved activity upon incorporation of Zr, attributed to the high oxygen storage capacity of $Ce_xZr_{1-x}O_2$ and high dispersion of Ni. Reduced Ru-doped CeO_2 shows higher catalytic activity compared to Ni, Co, and Pd doped CeO_2, since Ru facilitates the reduction of CeO_2 at mild temperature, resulting in more oxygen vacancies (86).

The mechanism for CO_2 methanation on metal catalysts supported on reducible oxides, such as CeO_2, follows either via the formate route or the CO route (92, 93). However, there are three steps which are common in both routes (Figure 1.11): 1. Adsorption of CO_2 on oxygen vacancy of CeO_2 (oxidizing CeO_2) and H_2 adsorption on a metal surface, 2. Formation of intermediate on a metal surface, and 3. Re-generation of oxygen vacancy via H-spillover (reducing CeO_2). Generally, the rate of reaction and concentration of oxygen vacancies depends on the rate constants of oxidation (step 1) and a reduction reaction (step 3).

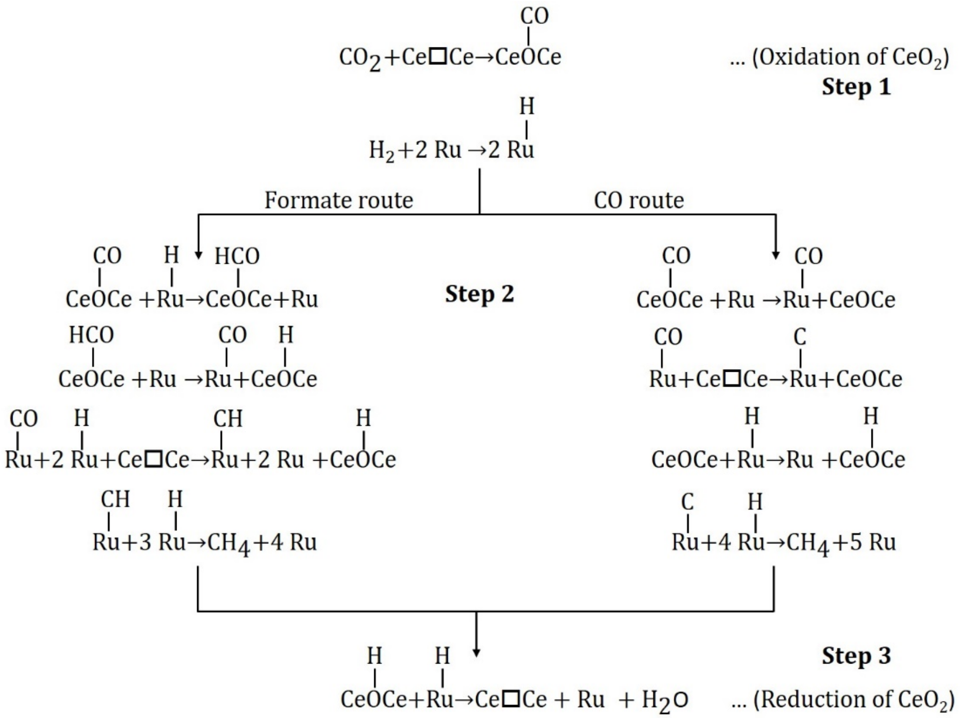

Figure 1. 11: Formate and CO pathways for the mechanism of CO_2 methanation (Ru is an active metal site, □ is oxygen vacancy). Adapted from our previous publication (17).

Effect of CeO_2 nano-shapes on the activity of CO_2 methanation is also studied using Ni and Ru catalysts. Wang et. al. (9) reported that the activity of Ru supported on cube-shaped CeO_2 is higher than rods shaped- CeO_2. However, the opposite trend in activity is reported by Bian et. al. (94) using supported Ni catalysts. Clearly, the overall activity is not determined by only CeO_2 morphology. It should be noted that the metal dispersion in both the studies was not kept constant and might have influenced the catalytic activity.

In the case of structure-sensitive reactions, the reaction rate per surface atom depends on the size of the metal particles. The structure sensitivity results from the geometric arrangement of surface atoms and the coordination number of surface metal atoms. Sometimes, electronic effects are presented as an alternative interpretation for such particle size effects. In general, figure 1.12 presents three types of structure sensitivity discussed by Che and Bennet (95). Type I reactions are structure-insensitive, where every surface atom is equally active. In type II, the turnover rate of a reaction decreases with increasing particle size. While in type III, the initial turnover rate increases with particle size and remains constant for bigger particles. Finally, the type IV is very similar to type III, where turnover rate increases initially and then decreases for bigger particles, forming a volcano-type curve.

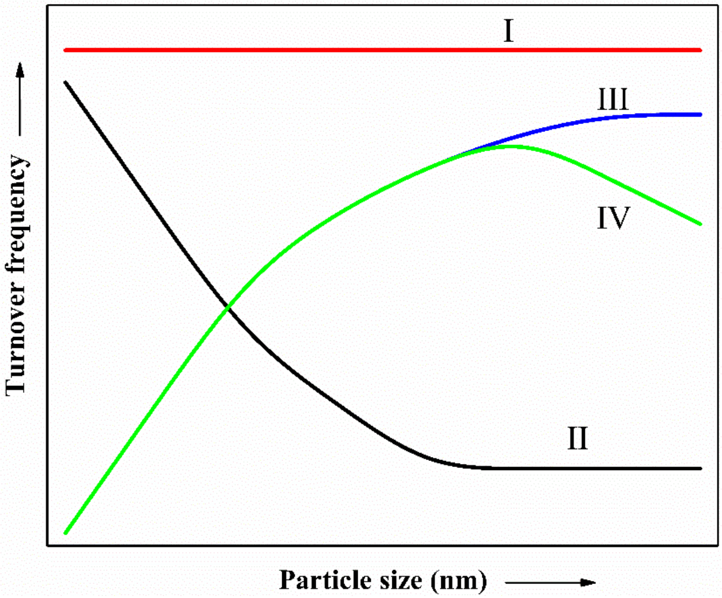

Figure 1.12: Three types of particle size-performance relationship. The figure is adapted from 95.

The effect of metal particle size on most common catalytic reaction has already been reported previously. For instance, Iablokov et. al. (96, 97) studied the effect of particle size using MCF-17 supported Co (3.5-12.2 nm) and Fe (1.8-9 nm) catalysts for CO oxidation and CO hydrogenation reaction respectively. It is reported that the reaction rate of smaller and larger particles was minimum, while catalysts with 5nm Co showed maximum activity for CO oxidation (96). Whereas, increasing turnover frequencies were observed with increasing Fe particle size for CO hydrogenation (97). Particle size effect of SiO_2 supported Ni catalysts on CO_2 methanation is also discussed recently (15, 98). Vogt et al. (15) reported maximum TOF for 2.5nm Ni catalysts, while Chen et. al. (98) shows decreasing activity from 2.4 to 4.7nm. Interestingly, both report the highest CO_2 methanation activity for catalysts with ~2.4nm particle size. Other reactions, namely propane oxidation (99), Fischer-Tropsch synthesis (100), water gas shift (101) and hydrodeoxygenation of m-Cresol (102), also known to have a significant effect of a size of metal particles.

1.4. Aims and scope of this thesis

As mentioned earlier, the application of CeO_2 as catalyst support with well-defined facets has been studied for a variety of reactions, e.g. oxidation, reforming, and hydrogenation. However, while comparing the performance of CeO_2 with different shapes, researchers have frequently overlooked the effect of metal particle size which also contributes to the total activity of catalysts. A complete overview of literature reporting on the structure-dependent activity of CeO_2 supported metal catalysts for different reactions is presented in Table S1.1. In order to report on the influence of the structure of the support, rates are preferably based on differential experiments, the metal surface area should be constant if rates are reported per gram catalysts (determined by loading and dispersion) or the rate is to be reported per m^2 surface area of metal. In addition, the metal particle size should be constant in order to rule out any effects based on structure sensitivity. Two reports (9, 94) published for CO_2 methanation observed the opposite trend in activity for different nano-shapes of CeO_2 when metal particle size was not kept constant. That raises the question over the actual trend of activity of catalyst supported on CeO_2 nano-shapes for CO_2 methanation reaction.

In this thesis, we present the importance of constant metal particle size when studying the morphology-dependent activity of hydrogenation reaction. The thesis also shows, experimentally, that activity of CO_2 methanation is particle size dependent in case of Ru and Ni catalysts. In short, this thesis carefully elucidates the role of metal (Ru and Ni) particle size and CeO_2 morphology on the activity of CO_2 methanation.

In **chapter 2**, Ru catalysts supported on rods, cubes, and octahedra shaped CeO_2 were prepared. Particle size was controlled and kept constant on all three catalysts. Here, we report on the effect of Ru on the redox properties of the different CeO_2 nano-shapes and on the correlation of these redox properties with the performance of the catalysts in CO_2 methanation.

In **chapter 3**, we studied the effect of Ru particle size on the performance of CO_2 methanation to prove the hypothesis made in chapter 2. Ru/CeO_2 catalysts with different Ru particle size is synthesized by varying RuO_2 loading and reduction temperature. The catalysts are characterized using H_2 & CO chemisorption, X-ray diffraction, electron microscopy, Raman spectroscopy, and hydrogen temperature programmed reduction (H_2-TPR). The results show that the activity per surface area of Ru depends on the particle size. The influence of Ru dissolution in CeO_2 is also discussed. The results of chapter 2 and 3 suggests that there are two rate-determining steps: one on Ru surface and other on CeO_2 support.

In **chapter 4**, we report that the activity of Ni on CeO_2 depends indeed on particle size. Thus, we studied the effect of the CeO_2 nano-shapes with a catalyst with identical metal particle sizes, which then allows to correlate the activity of the catalyst with the redox properties of the support. This work clarifies the effect of CeO_2 morphology on the performance of Ni/CeO_2 catalysts in CO_2 methanation. Also, the effect of the redox properties of CeO_2 support on catalyst performance is discussed. Finally, two steps are suggested to be rate-determining; 1. adsorption of CO_2 on oxygen vacancy and 2. hydrogenation of a carbon-containing intermediate on the Ni surface. Presence of two rate-determining steps is in good agreement with the Ru/CeO_2 catalysts reported in chapter 2 and 3.

In **chapter 5**, all the results generated during this research are summarized and the perspective for future research is provide.

References

1. EU Roadmap, Mapping Renewable Energy Pathways towards 2020, EREC (2011).

2. Tanja Schaaf, Jochen Grünig, Markus Roman Schuster, Tobias Rothenfluh, Andreas Orth. *Energ Sustain Soc* **2014**, 4:2.

3. Harry L. Tuller. *Mater Renew Sustain Energy* **2017**, 6:3.

4. Karim Ghaib, Fatima-Zahrae Ben-Fares. *Renewable Sustainable Energy Rev.* **2018**, 81, 433-446.

5. Alexander Buttler, Hartmut Spliethoff. *Renewable Sustainable Energy Rev.* **2018**, 82, 2440-2454.

6. Yong Jung, Soo Jang, Hyun You. *Chinese Phys. Lett.* **2013**, 30, 065204.

7. Saeed Sahebdelfar, Maryam Ravanchi. *J. Petrol. Sci. Eng.* **2015**, 134, 14-22.

8. Qingquan Lin, Xiao Yan Liu, Ying Jiang, Yong Wang, Yanqiang Huang, Tao Zhang. *Catal. Sci. Technol.* **2014**, 4, 2058-2063.

9. Fei Wang, Changming Li, Xiaoyu Zhang, Min Wei, David G. Evans, Xue Duan. *J. Catal.* **2015**, 329, 177-186.

10. Robert D. Hetterley, Richard Mackey, James T.A. Jones, Yaroslav Z. Khimyak, Andrew M. Fogg, Ivan V. Kozhevnikov. *J. Catal.* **2008**, 258, 250-255.

11. Wei Wang, Wei Chu, Ning Wang, Wen Yang, Chengfa Jiang. *Int. J. Hydrogen Energy* **2016**, 41, 967-975.

12. Guilin Zhou, Tian Wu, Hongmei Xie, Xuxu Zheng. *Int. J. Hydrogen Energy* **2013**, 38, 10012-10018.

13. F. Graf, M. Gotz, M. Henel, T. Schaaf, R. Tichler. Techno-okonomische Studie von Power-to-Gas-Konzepten, Final report,

Deutscher Verein des Gas- und Wasserfaches (DVGW), Bonn **2014**. DOI: 10.13140/RG.2.1.2001.9366.

14. A. Erhan Aksoylu, A. Nilgün Akin, Z. İlsen Önsan, David L. Trimm. *Appl. Catal. A* **1996**, 145, 185-193.

15. Charlotte Vogt, Esther Groeneveld, Gerda Kamsma, Maarten Nachtegaal, Li Lu, Christopher Kiely, Peter Berben, Florian Meirer, Bert Weckhuysen. *Nat. Catal.* **2018**, 1, 127–134.

16. Mengdie Cai, Jie Wen, Wei Chu, Xueqing Cheng, Zejun Li. *J. Nat. Gas Chem.* **2011**, 20, 318-324.

17. Tushar Sakpal, Leon Lefferts. *J. Catal.* **2018**, 367, 171-180.

18. Huanling Song, Jian Yang, Jun Zhao, Lingjun Chou. *Chin. J. Catal.* **2010**, 31, 21-23.

19. Yanrong Li, Gongxuan Lu, Jiantai Ma. *RSC Adv.* **2014**, 4, 17420-17428.

20. Ara Kim, Damien P. Debecker, François Devred, Vincent Dubois, Clément Sanchez, Capucine Sassoye. *Appl. Catal. B* **2018**, 220, 615-625.

21. M. Romero-Sáez, A. B. Dongil, N. Benito, R. Espinoza-González, N. Escalona, F. Gracia. *Appl. Catal. B* **2018**, 237, 817-825.

22. Andreas Borgschulte, Noris Gallandat, Benjamin Probst, Riccardo Suter, Elsa Callini, Davide Ferri, Yadira Arroyo, Rolf Erni, Hans Geerlings, Andreas Züttel. *Phys. Chem. Chem. Phys.* **2013**, 15, 9620-9625.

23. Zbigniew Kowalczyk, Kazimierz Stołecki, Wioletta Pilecka, Elżbieta Miśkiewicz, Ewa Wilczkowska, Zbigniew Karpiński. *Appl. Catal.* A **2008**, 342, 35-39.

24. Takayuki Abe, Masaaki Tanizawa, Kuniaki Watanabe, Akira Taguchi. *Energy Environ. Sci.* **2009**, 2, 315-321.

25. Calvin H. Bartholomew. *Appl. Catal. A* **2001**, 212, 17-60.

26. O. Levenspiel, Chemical Reaction Engineering, 3rd edition, John Wiley and Sons, **1998**.

27. Xiong Su, Jinghua Xu, Binglian Liang, Hongmin Duan, Baolin Hou, Yanqiang Huang. *J. Energy Chem.* **2016**, 25, 553-565.

28. Lichen Liu and Avelino Corma. *Chem. Rev.* **2018**, 118, 4981-5079.

29. Botao Qiao, Jin-Xia Liang, Aiqin Wang, Cong-Qiao Xu, Jun Li, Tao Zhang, Jingyue Jimmy Liu. *Nano res.* **2015**, 8, 2913–2924.

30. Xiao-Feng Yang, Aiqin Wang, Botao Qiao, Jun Li, Jingyue Liu, Tao Zhang. *Acc. Chem. Res.* **2013**, 46, 1740-1748.

31. Hongling Guan, Jian Lin, Botao Qiao, Shu Miao, Ai-Qin Wang, Xiaodong Wang, Tao Zhang. *AIChE J.* **2017**, 63, 2081-2088.

32. Cong Liu, Bing Yang, Eric Tyo, Soenke Seifert, Janae DeBartolo, Bernd von Issendorff, Peter Zapol, Stefan Vajda, Larry A. Curtiss. *J. Am. Chem. Soc.* **2015**, 137, 8676-8679.

33. Joachim Paier, Christopher Penschke, Joachim Sauer. *Chem. Rev.* **2013**, 113, 3949−3985.

34. Mogens Mogensen, Nigel M. Sammes, Geoff A. Tompsett. *Solid State Ionics* **2000**, 129, 63-94.

35. Liangdong Fan, Chengyang Wang, Mingming Chen, Bin Zhu. *J. Power Sources* **2013**, 234, 154-174.

36. Chunwen Sun, Hong Li, Liquan Chen. *Energy Environ. Sci.* **2012**, 5, 8475-8505.

37. Weixin Huang and Yuxian Gao. *Catal. Sci. Technol.* **2014**, 4, 3772-3784.

38. Laurence Vivier, Daniel Duprez. *ChemSusChem* **2010**, 3, 654 – 678.

39. Dengsong Zhang, Xianjun Du, Liyi Shi, Ruihua Gao. *Dalton Trans.* **2012**, 41, 14455-14475.

40. Alessandro Trovarelli. *Catal. Rev.* **1996**, 38, 439-520.

41. Tiziano Montini, Michele Melchionna, Matteo Monai, Paolo Fornasiero. *Chem. Rev.* **2016**, 116, 5987−6041.

42. Bryant C. Nelson, Monique E. Johnson, Marlon L. Walker, Kathryn R. Riley, Christopher M. Sims. *Antioxidants* **2016**, 5, 15.

43. Can Xu, Youhui Lin, Jiasi Wang, Li Wu, Weili Wei, Jinsong Ren, Xiaogang Qu. *Adv. Healthcare Mater.* **2013**, 2, 1591–1599.

44. Alessandro Trovarelli, Carla de Leitenburg, Marta Boaro, Giuliano Dolcetti. *Catal. Today* **1999**, 50, 353-367.

45. A. F. Diwell, R. R. Rajaram, H. A. Shaw, T. J. Truex. *Stud. Surf. Sci. Catal.* **1991**, 71, 139-152.

46. Lluís Soler, Albert Casanovas, Carlos Escudero, Virginia Pérez-Dieste, Eleonora Aneggi, Alessandro Trovarelli, Jordi Llorca. *ChemCatChem* **2016**, 8, 2748 –2751.

47. R.W.G. Wyckoff. Crystal Structures–volume 1. 2nd edition, New York: Interscience publisher, **1963**.

48. David R. Mullins. *Surf. Sci. Rep.* **2015**, 70, 42-85.

49. Damma Devaiah, Takuya Tsuzuki, Thirupathi Boningari, Panagiotis G. Smirniotis, Benjaram M. Reddy. *RSC Adv.* **2015**, 5, 30275-30285.

50. A. Bueno-López, K. Krishna, M. Makkee, J. A. Moulijn. *J. Catal.* **2005**, 230, 237-248.

51. Kyung Joo Lee, Yongseon Kim, Jae Hwa Lee, Sung June Cho, Ja Hun Kwak, Hoi Ri Moon. *Chem. Mater.* **2017**, 29, 2874−2882.

52. Damma Devaiah, Lankela H. Reddy, Sang-Eon Park, Benjaram M. Reddy. *Catal. Rev.* **2018**, 60, 177–277.

53. Wei Deng, Qiguang Dai, Yijie Lao, Bingbing Shi, Xingyi Wang. *Appl. Catal. B* **2016**, 181, 848-861.

54. Maria Ventura, Francesco Lobefaro, Elvira de Giglio, Monica Distaso, Francesco Nocito, Angela Dibenedetto. *ChemSusChem* **2018**, 11, 1305 –1315.

55. Claude Descorme, Rachid Taha, Najat Mouaddib-Moral, Daniel Duprez. *Appl. Catal. A* **2002**, 223, 287-299.

56. Kebin Zhou, Yadong Li. *Angew. Chem. Int. Ed.* **2012**, 51, 602 – 613.

57. Andreas Tschöpe, Wei Liu, Maria Flytzani-Stephanopoulos, Jackie Ying. *J. Catal.* **1995**, 157, 42-50.

58. Quan Yuan, Hao-Hong Duan, Le-Le Li, Ling-Dong Sun, Ya-Wen Zhang, Chun-Hua Yan. *J. Colloid Interface Sci.* **2009**, 335, 151-167.

59. Zili Wu, Meijun Li, Jane Howe, Harry M. Meyer III, Steven H. Overbury. *Langmuir* **2010**, 26, 16595-16606.

60. P W Tasker. *J. Phys. C: Solid State Phys.* **1979**, 12, 4977.

61. David Mullins, Peter Albrecht, Florencia Calaza. *Top. Catal.* **2013**, 56, 1345–1362.

62. Peter M. Albrecht and David R. Mullins. *Langmuir* **2013**, 29, 4559−4567.

63. M. Verónica Ganduglia-Pirovano, Alexander Hofmann, Joachim Sauer. *Surf. Sci. Rep.* **2007**, 62, 219-270.

64. Shilpa Agarwal, Leon Lefferts, Barbara Mojet, D. A. J. Michel Ligthart, Emiel Hensen, David Mitchell, Willem Erasmus, Bruce G. Anderson, Ezra J. Olivier, Johannes H. Neethling, Abhaya K. Datye. *ChemSusChem* **2013**, 6, 1898–1906.

65. Hao-Xin Mai, Ling-Dong Sun, Ya-Wen Zhang, Rui Si, Wei Feng, Hong-Peng Zhang, Hai-Chao Liu, Chun-Hua Yan. *J. Phys. Chem. B* **2005**, 109, 24380-24385.

66. Chengsi Pan, Dengsong Zhang, Liyi Shi, Jianhui Fang. *Eur. J. Inorg. Chem.* **2008**, 2429–2436.

67. Wei-Wei Wang, Wen-Zhu Yu, Pei-Pei Du, Hui Xu, Zhao Jin, Rui Si, Chao Ma, Shuo Shi, Chun-Jiang Jia, Chun-Hua Yan. *ACS Catal.* **2017**, 7, 1313-1329.

68. Andre Kaftan, Fabian Kollhoff, Thanh-Son Nguyen, Laurent Piccolo, Mathias Laurina, Jörg Libuda. *Catal. Sci. Technol.* **2016**, 6, 818-828.

69. Y. Suchorski, R. Wrobel, S. Becker, H. Weiss. *J. Phys. Chem. C* **2008**, 112, 20012-20017.

70. Joon B. Park, Jesus Graciani, Jaime Evans, Dario Stacchiola, Sanjaya D. Senanayake, Laura Barrio, Ping Liu, Javier Fdez. Sanz, Jan Hrbek, José A. Rodriguez. *J. Am. Chem. Soc.* **2010**, 132, 356-363.

71. Joon B. Park, Jesus Graciani, Jaime Evans, Dario Stacchiola, Shuguo Ma, Ping Liu, Akira Nambu, Javier Fernández Sanz, Jan Hrbek, José A. Rodriguez. *PNAS* **2009**, 106, 4975-4980.

72. José A. Rodriguez, David C. Grinter, Zongyuan Liu, Robert M. Palominoa, Sanjaya D. Senanayake. *Chem. Soc. Rev.* **2017**, 46, 1824-1841.

73. A. Hornés, A. B. Hungría, P. Bera, A. López Cámara, M. Fernández-García, A. Martínez-Arias, L. Barrio, M. Estrella, G. Zhou, J. J. Fonseca, J. C. Hanson, J. A. Rodriguez. *J. Am. Chem. Soc.* **2010**, 132, 34-35.

74. Xiucheng Zheng, Shuping Wang, Shurong Wang, Shoumin Zhang, Weiping Huang, Shihua Wu. *Catal. Commun.* **2004**, 5, 729-732.

75. P. V. Snytnikov, M. M. Popova, Y. Men, E. V. Rebrov, G. Kolb, V. Hessel, J. C. Schouten, V. A. Sobyanin. *Appl. Catal. A* **2008**, 350, 53-62.

76. Fan Yang, Jesús Graciani, Jaime Evans, Ping Liu, Jan Hrbek, Javier Fdez. Sanz, José A. Rodriguez. *J. Am. Chem. Soc.* **2011**, 133, 3444-3451.

77. Robbie Burch. *Phys. Chem. Chem. Phys.* **2006**, 8, 5483-5500.

78. José A. Rodriguez, Ping Liu, Jan Hrbek, Jaime Evans, Manuel Pérez. *Angew. Chem. Int. Ed.* **2007**, 46, 1329–1332.

79. Albert Bruix, José A. Rodriguez, Pedro J. Ramírez, Sanjaya D. Senanayake, Jaime Evans, Joon B. Park, Dario Stacchiola, Ping Liu, Jan Hrbek, Francesc Illas. *J. Am. Chem. Soc.* **2012**, 134, 8968-8974.

80. Sanjaya D. Senanayake, Jaime Evans, Stefano Agnoli, Laura Barrio, Tsung-Liang Chen, Jan Hrbek, José A. Rodriguez. *Top. Catal.* **2011**, 54, 34–41.

81. Michele Aresta, Carbon Dioxide as Chemical Feedstock. 1st edition, Wiley-VCH, New York, **2010**.

82. Sanjaya Senanayake, Pedro Ramírez, Iradwikanari Waluyo, Shankhamala Kundu, Kumudu Mudiyanselage, Zongyuan Liu, Zhi Liu, Stephanus Axnanda, Dario Stacchiola, Jaime Evans, José Rodriguez. *J. Phys. Chem. C* **2016**, 120, 1778-1784.

83. Shaobin Wang, G. Q (Max) Lu. *Appl. Catal. B* **1998**, 19, 267-277.

84. Victor M. Gonzalez-DelaCruz, Juan P. Holgado, Rosa Pereñíguez, Alfonso Caballero. *J. Catal.* **2008**, 257, 307-314.

85. Shohei Tada, Teruyuki Shimizu, Hiromichi Kameyama, Takahide Haneda, Ryuji Kikuchi. *Int. J. Hydrogen Energy* **2012**, 37, 5527-5531.
86. Sudhanshu Sharma, Zhenpeng Hu, Peng Zhang, Eric W. McFarland, Horia Metiu. *J. Catal.* **2011**, 278, 297-309.
87. D. Chester Upham, Alan R. Derk, Sudanshu Sharma, Horia Metiu, Eric W. McFarland. *Catal. Sci. Technol.* **2015**, 5, 1783-1791.
88. Hongwei Zhu, Rauf Razzaq, Chunshan Li, Yaseen Muhmmad, Suojiang Zhang. *AIChE J.* **2013**, 59, 2567-2576.
89. Rauf Razzaq, Chunshan Li, Nadeem Amin, Suojiang Zhang, Kenzi Suzuki. *Energy Fuels* **2013**, 27, 6955-6961.
90. Qiushi Pan, Jiaxi Peng, Tianjun Sun, Sheng Wang, Shudong Wang. *Catal. Commun.* **2014**, 45, 74-78.
91. Fabien Ocampo, Benoit Louis, Anne Roger. *Appl. Catal. A* **2009**, 369, 90-96.
92. Fei Wang, Shan He, Hao Chen, Bin Wang, Lirong Zheng, Min Wei, David G. Evans, Xue Duan. *J. Am. Chem. Soc.* **2016**, 138, 6298-6305.
93. Alfredo Solis-Garcia, Jose F. Louvier-Hernandez, Armando Almendarez-Camarillo, Juan C. Fierro-Gonzalez. *Appl. Catal. B* **2017**, 218, 611-620.
94. Zhoufeng Bian, Yi Meng Chan, Yang Yu, Sibudjing Kawi. *Catal. Today* **2018**, DOI: 10.1016/j.cattod.2018.04.067.
95. Michel Che, Carroll O. Bennett. *Adv. Catal.* **1989**, 36, 55-172.
96. Viacheslav Iablokov, Roland Barbosa, Glenn Pollefeyt, Isabel Van Driessche, Sergey Chenakin, Norbert Kruse. *ACS Catal.* **2015**, 5, 5714-5718.

97. Viacheslav Iablokov, Yizhi Xiang, Anca Meffre, Pier-Francesco Fazzini, Bruno Chaudret, Norbert Kruse. *ACS Catal.* **2016**, 6, 2496-2500.

98. Ching-Shiun Chen, Canggih Setya Budi, Hung-Chi Wu, Diganta Saikia, Hsien-Ming Kao. *ACS Catal.* **2017**, 7, 8367-8381.

99. Zong Hu, Xiaofei Liu, Dongmei Meng, Yun Guo, Yanglong Guo, Guanzhong Lu. *ACS Catal.* **2016**, 6, 2265-2279.

100. Yao Chen, Xin Li, Mehar Nisa, Jing Lv, Zhenhua Li. *Fuel* **2019**, 241, 802-812.

101. C. M. Kalamaras, D. D. Dionysiou, A. M. Efstathiou. *ACS Catal.* **2012**, 2, 2729-2742.

102. Feifei Yang, Dan Liu, Yuntao Zhao, Hua Wang, Jinyu Han, Qingfeng Ge, Xinli Zhu. *ACS Catal.* **2018**, 8, 1672-1682.

Appendix

Table S1.1: Overview of literature reporting on the structure-dependent activity of CeO_2 supported metal catalysts for different reactions. In order to report on the influence of the structure of the support, rates are preferably based on differential experiments, the metal surface area should be constant if rates are reported per gram catalysts (determined by loading and dispersion) or the rate is to be reported per m^2 metal surface area. In addition, the metal particle size should be constant in order to rule out any effects based on structure sensitivity.

Reference	**reaction**	**Activity trend**	**Units**	**conditions**	**Metal (wt%)**	**Particle size (nm)**		
						cubes	**rods**	**O/P/S**
Bian et.al.[1]	CO_2 methanation	Rods>cubes	CO_2 conv. (%)	Differential	Ni (5%)	na	na	na
Wang et.al.[2]	CO_2 methanation	Cubes>octa>rods	Mol/g_{cat}/s	Differential	Ru TEM/PSD	1.7 (±1.23)	3.2 (±0.9)	2 (±1.0)
Torrente-Murciano et.al.[3]	WGS	Rods>cubes	Mol/kg_{cat}/h	Differential	Pt (1.5%) CO chemisorp.	1.5	1	0.8
Lin et.al.[4]	WGS	cubes≈rods	Conversion	Integral	Au (3-5nm) TEM/PSD	3 (±1.0)	-	5 (±1.5)
Ma et.al.[5]	Ammonia Synthesis	Rods>cubes>particle	mmol/g_{cat}/h	unknown	Ru CO chemisorp.	5.7	3.3	3.7
Lin et.al.[6]	Ammonia Synth.	Rods>cubes	Mol/g_{cat}/h	Differential	Ru (2-3.6nm) TEM+H_2 Chem.	2	-	3.6
Soykal et.al.[7]	Ethanol steam reforming	Cubes>rods	conversion	integral	Co (10%) N_2O chem.	4.8	14.5	-
Boucher et.al.[8]	steam reforming of methanol	Rods>cubes	mmol/m^2_{ceria}/s	Differential	Au (1-3nm) TEM/no PSD	3	1	-
Araiza et.al.[9]	steam reforming of ethanol	Rods>cubes>particle	Conversion	Integral	Ni (10%) N_2O chem.	22.2	6	25.4

Wang et.al.[10]	Ethanol steam reforming	NP>rods	conversion	integral	Co (6.5-20nm) TEM/no PSD		10-30	5-8
Du et.al.[11]	DRM	Rods>octa	Conversion (%)	integral	Ni (5%)	na	na	na
Liu et.al.[12]	NO reduction by CO	Rods>octa>cubes	Mol/g/s	Differential	Cu (No info)	na	na	na
Savereide et.al.[13]	reduction of NO by CO	Rods>cubes	mmol/g_{cat}/s	Unknown	Cu (1%)	na	na	na
Zabilskiy et.al.[14]	N_2O decomposition	Cubes>octa>rods	Ea (kJ/mol)	Differential	Cu (2.1-5.1nm) N_2O chem.	5.1	2.4	2.1
Wang et.al.[15]	Dehydrogenation: ammonia borane	Cubes>rods>octa	Ea (kJ/mol)	differential	Ru (1.8%)	na	na	na
Ciftci et.al.[16]	formic acid decomposition	Rods>cubes	Mol/mol_{Au}/h	Differential	Au (2.1%) H_2 chemi.	5.5	0.8	-
Huang et.al.[17]	combustion of chlorobenzene	Rods>cubes>octa	mmol/m^2_{ceria}/min	Differential	Ru TEM typ. PS	6-8	6-8	10
Tong et.al.[18]	hydrogenolysis of furfuryl alcohol	Cubes>octa>rods	Yield (%)	Integral	Pt TEM/PSD	4.1 (±3.0)	2.4 (±1.8)	5.9 (±3.8)
Han et.al.[19]	Reduction of NO with NH3	Rods>octa	TOF (s^{-1})	Differential	Fe (3%)	na	na	na
Cui et.al.[20]	carbonate hydrogenation	Rods>particle>cubes	Conversion	Integral	Cu N_2O Chemi.	15.3	2.7	2.1
Carraro et.al.[21]	Methanol Decomposition	Rods>cubes	Conversion	Integral	Pd (5%)	10 (±3.0)	5 (±2.0)	-
Singhania et.al.[22]	CO oxidation	Rods>cubes>octa	Mol/g/s	Differential	Pt (5%)	2-3 nm (typical, no PSD)		
Hu et.al.[23]	CO oxidation	Rods>cubes>octa	TOF (s^{-1})	Differential	Pd (1.9-4.6nm) CO chem.	2.9	1.9	4.6
Wang et.al.[24]	CO Oxidation	Rods>spheres	Mol/g_{cat}/s	Differential	Cu (1-1.2%)	31%	Disp.	100%
Kunming et.al.[25]	CO oxidation	Rods>cubes	Conversion	integral	Au (1%)	na	na	na

Lykaki et.al.[26]	CO oxidation	Rods>octa>cubes	nmol/g_{cat}/s	differential	Cu (7.2-7.6%)			
Huang et.al.[27]	CO oxidation	Rods>NP	Mol/g_{cat}/h	differential	Au (1%)			
Chang et.al.[28]	CO oxidation	cubes≈rods	mol/mol_{Ag}/s	Differential	Ag (3%)	Cubes>rods (UV-Vis)		
Spezzati et.al.[29]	CO oxidation	Rods>cubes	Conversion	Integral	Pd (1%) TEM	2nm	Not seen	-
Han et.al.[30]	PROX CO	Octa>rods>cubes	conversion	integral	Cu (4%)	na	na	na
Gamarra et.al.[31]	PROX CO	Cubes>rods≈spheres	Mol/g_{cat}/min	differential	Cu (1%)	na	na	na
Carltonbird et.al.[32]	PROX CO	Rods>cubes>octa	conversion	integral	Au (1%)	na	na	na
Guo et.al.[33]	PROX CO	Rods>cubes	CO conv. (%)	Diff+Int.	Cu (5%)	na	na	na
Yi et.al.[34]	PROX CO	Rods>octa>cubes	conversion	integral	Au (1%)	Na	na	na
Yi et.al.[35]	PROX CO	Rods>octa>cubes	Mol/g_{Au}/s	differential	Au (1%)	na	na	na
Gao et.al.[36]	PROX CO	Rods>cubes>octa	mmol/mol_{Pt}/s	differential	Pt (1.5-2nm) TEM/PSD	1.5 (±0.3)	2.0 (±0.3)	1.7 (±0.5)
Zhang et.al.[37]	Propane oxidation	Rods>cubes	TOF (min^{-1})	Differential	Ni (1%)	na	na	na
Tan et.al.[38]	Formaldehyde Oxidation	Cubes>octa>rods	conversion	integral	Pd (1-2nm, 1%) no PSD	1-	1-2	1-2
Mei et.al.[39]	Dibromomethane oxidation	Rods>plates>cubes	Conversion	Integral	Co (10-16nm)	19.7	10.4	13.2
Peng et.al.[40]	oxidation of toluene	Rods>octa>cubes	mol/g_{cat}/s	Differential	Pt TEM/typical	2.8-4.5	2.8-4.5	2.8-4.5
Yu et.al.[41]	oxidation of HCHO	Rods>cubes>octa	mmol/m^2_{ceria}/s	Integral	Ag (4.7%) TEM/no PSD	~4.0	~4.0	~4.0
Araiza et.al.[42]	Partial oxidation of methanol	Rods>cubes	Conversion	Integral	Cu N_2O chemi.	6.9	2.1	2.1
Lei et.al.[43]	lean methane combustion	Octa>cubes>rods	mol/m^2_{ceria}/s	Differential	Pd (1.8%)	na	na	na

Na= not available, PSD= particle size distribution, O= octahedra, P= particles, S= spheres.

References

1. Zhoufeng Bian, Yi Meng Chan, Yang Yu, Sibudjing Kawi. *Catal. Today* **2018**, DOI: 10.1016/j.cattod.2018.04.067.
2. Fei Wang, Changming Li, Xiaoyu Zhang, Min Wei, David G. Evans, Xue Duan. *J. Catal.* **2015**, 329, 177–186.
3. Laura Torrente-Murciano, Francisco Javier Garcia-Garcia. *Catal. Commun.* **2015**, 71, 1–6.
4. Yuyuan Lin, Zili Wu, Jianguo Wen, Kunlun Ding, Xiaoyun Yang, Kenneth R. Poeppelmeier, Laurence D. Marks. *Nano Lett.* **2015**, 15, 5375-5381.
5. Zhanwei Ma, Shengli Zhao, Xiaoping Pei, Xumao Xiong, Bin Hu. *Catal. Sci. Technol.* **2017**, 7, 191-199.
6. Bingyu Lin, Yi Liu, Lan Heng, Xiuyun Wang, Jun Ni, Jianxin Lin, Lilong Jiang. *Ind. Eng. Chem. Res.* **2018**, 57, 28, 9127-9135.
7. I. Ilgaz Soykal, Burcu Bayram, Hyuntae Sohn, Preshit Gawade, Jeffrey T. Miller, Umit S. Ozkan. *Appl. Catal., A* **2012**, 449, 47-58.
8. Matthew B. Boucher, Nan Yi, Forrest Gittleson, Branko Zugic, Howard Saltsburg, Maria Flytzani-Stephanopoulos. *J. Phys. Chem. C* **2011**, 115, 1261-1268.
9. Daniel G. Araiza, Antonio Gómez-Cortés, Gabriela Díaz. *Catal. Today* **2018**, DOI:10.1016/j.cattod.2018.03.016.
10. Hong Wang, Lijuan Zhang, Miao Li, Yuan Liu, Xue Bai. *J. Rare Earths* **2013**, 31, 565-571.
11. Xianjun Du, Dengsong Zhang, Liyi Shi, Ruihua Gao, Jianping Zhang. *J. Phys. Chem. C* **2012**, 116, 18, 10009-10016.
12. Lianjun Liu, Zhijian Yao, Yu Deng, Fei Gao, Bin Liu, Lin Dong. *ChemCatChem* **2011**, 3, 978-989.
13. Louisa Savereide, Scott L. Nauert, Charles A. Roberts, Justin M. Notestein. *J. Catal.* **2018**, 366, 150-158.
14. Maxim Zabilskiy, Petar Djinović, Elena Tchernychova, Olga P. Tkachenko, Leonid M. Kustov, Albin Pintar. *ACS Catal.* **2015**, 5, 5357-5365.
15. Ruyue Wang, Yong Wang, Mengqi Ren, Guoxin Sun, Daowei Gao, Yap Ray Chin Chong, Xu Li, Guozhu Chen. *Int. J. Hydrogen Energy* **2017**, 42, 6757-6764.

16. Aysegul Ciftci, D. A. J. Michel Ligthart, Pietro Pastorino, Emiel J. M. Hensen. *Appl. Catal., B* **2013**, 130–131, 325-335.
17. Hao Huang, Qiguang Dai, Xingyi Wang. *Appl. Catal., B* **2014**, 158–159, 96-105.
18. Tao Tong, Xiaohui Liu, Yong Guo, Mohammad Norouzi Banis, Yongfeng Hu, Yanqin Wang. *J. Catal.* **2018**, 365, 420-428.
19. Jin Han, Jittima Meeprasert, Phornphimon Maitarad, Supawadee Nammuangruk, Liyi Shi, Dengsong Zhang. *J. Phys. Chem. C* **2016**, 120, 1523-1533.
20. Yuanyuan Cui, Wei-Lin Dai. *Catal. Sci. Technol.* **2016**, 6, 7752-7762.
21. Francesco Carraro, Adebayo Fapohunda, Maria C. Paganini, Stefano Agnoli. *ACS Appl. Nano Mater.* **2018**, 1, 1492-1501.
22. Nisha Singhania, E. A. Anumol, N. Ravishankar, Giridhar Madras. *Dalton Trans.* **2013**, 42, 15343-15354.
23. Zong Hu, Xiaofei Liu, Dongmei Meng, Yun Guo, Yanglong Guo, Guanzhong Lu. *ACS Catal.* **2016**, 6, 2265-2279.
24. Wei-Wei Wang, Wen-Zhu Yu, Pei-Pei Du, Hui Xu, Zhao Jin, Rui Si, Chao Ma, Shuo Shi, Chun-Jiang Jia, Chun-Hua Yan. *ACS Catal.* **2017**, 7, 1313-1329.
25. Kunming Jia, Huili Zhang, Wencui Li. *Chin. J. Catal.* **2008**, 29, 1089-1092.
26. Maria Lykaki, Eleni Pachatouridou, Sónia A. C. Carabineiro, Eleni Iliopoulou, Chrysanthi Andriopoulou, N. Kallithrakas-Kontos, Soghomon Boghosian, Michalis Konsolakis. *Appl. Catal., B* **2018**, 230, 18-28.
27. Xin-Song Huang, Hao Sun, Lu-Cun Wang, Yong-Mei Liu, Kang-Nian Fan, Yong Cao. *Appl. Catal., B* **2009**, 90, 224-232.
28. Sujie Chang, Mo Li, Qing Hua, Lijuan Zhang, Yunsheng Ma, Bangjiao Ye, Weixin Huang. *J. Catal.* **2012**, 293 195–204.
29. Giulia Spezzati, Angelica D. Benavidez, Andrew T. DeLaRiva, Yaqiong Su, Jan P. Hofmann, Shunsuke Asahina, Ezra J. Olivier, Johannes H. Neethling, Jeffrey T. Miller, Abhaya K. Datye, Emiel J. M. Hensen. *Appl. Catal., B* **2019**, 243, 36-46.

30. Jaeman Han, Hyung Jun Kim, Sangwoon Yoon, Hyunjoo Lee. *J. Mol. Catal. A: Chem.* **2011**, 335, 82-88.
31. Daniel Gamarra, Antonio López Cámara, Manuel Monte, Søren Birk Rasmussen, Lidia Chinchilla, Ana Belén Hungría, Guillermo Munuera, Nóra Gyorffy, Zoltán Schay, Vicente Cortés Corberán, Jose Conesa, Arturo Martínez-Arias. *Appl. Catal., B* **2013**, 130–131, 224–238.
32. Mike Carltonbird, Srisin Eaimsumang, Sangobtip Pongstabodee, Supakorn Boonyuen, Siwaporn Meejoo Smith, Apanee Luengnaruemitchai. *Chem. Eng. J.* **2018**, 344, 545-555.
33. Xiaolin Guo, Renxian Zhou. *Catal. Sci. Technol.* **2016**, 6, 3862-3871.
34. Guangquan Yi, Zhongning Xu, Guocong Guo, Ken Tanaka, Youzhu Yuan. *Chem. Phys. Lett.* **2009**, 479, 128-132.
35. Guangquan Yi, Hongwei Yang, Bodong Li, Haiqiang Lin, Ken-ichi Tanaka, Youzhu Yuan. *Catal. Today* **2010**, 157, 83-88.
36. Yuxian Gao, Wendong Wang, Sujie Chang, Weixin Huang. *ChemCatChem* **2013**, 5, 3610–3620.
37. Xuanyu Zhang, Rui You, Dan Li, Tian Cao, Weixin Huang. *ACS Appl. Mater. Interfaces* **2017**, 9, 35897-35907.
38. Hongyi Tan, Jin Wang, Shuzhen Yu, Kebin Zhou. *Environ. Sci. Technol.* **2015**, 49, 8675-8682.
39. Jian Mei, Yu Ke, Zhongjue Yu, Xiaofang Hu, Zan Qu, Naiqiang Yan. *Chem. Eng. J.* **2017**, 320, 124-134.
40. Ruosi Peng, Xibo Sun, Shujun Li, Limin Chen, Mingli Fu, Junliang Wu, Daiqi Ye. *Chem. Eng. J.* **2016**, 306, 1234–1246.
41. Lian Yu, Ruosi Peng, Limin Chen, Mingli Fu, Junliang Wu, Daiqi Ye. *Chem. Eng. J.* **2018**, 334, 2480-2487.
42. Daniel G. Araiza, Antonio Gómez-Cortés, Gabriela Díaz. *Catal. Today* **2017**, 282, 185-194.
43. Yanyan Lei, Wenzhi Li, Qingchuan Liu, Qizhao Lin, Xusheng Zheng, Qifu Huang, Shengnan Guan, Xinhua Wang, Chengxin Wang, Fengyu Li. *Fuel* **2018**, 233, 10-20.

Chapter 2

Structure-dependent activity of CeO_2 supported Ru catalysts for CO_2 methanation

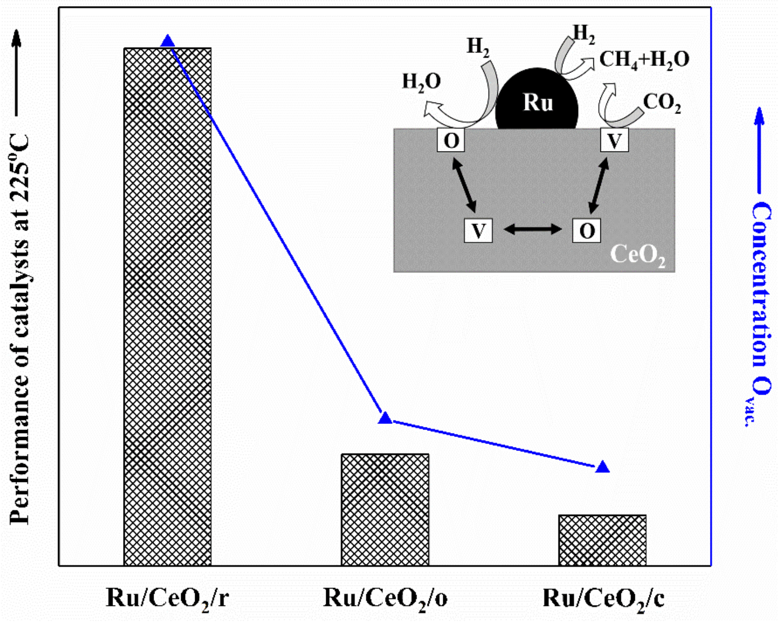

This chapter has been published as,
T. Sakpal and L. Lefferts. Structure-dependent activity of CeO_2 supported Ru catalysts for CO_2 methanation. *J. Catal.*, 367, **2018**, 171-180.

Abstract

In this study, CeO_2 rods (CeO_2/r), cubes (CeO_2/c) and octahedra (CeO_2/o) supported catalysts with identical Ru particles size were prepared. Trend in the activity of these catalysts for CO_2 methanation was compared with the trend in their oxygen vacancy concentration measured after calcination. Ru/CeO_2/r outperforms the other two catalysts with a reaction rate of 11.0×10^{-8} mol $s^{-1}m^{-2}_{Ru}$ and selectivity to methane of 99% at 250°C. Temperature-programmed reduction (TPR), Raman and X-ray photoemission spectroscopy (XPS) results confirms that Ru addition enhances reduction of CeO_2. Also, Ru/CeO_2/r is more reducible and contains more oxygen vacancies as compared to Ru/CeO_2/o and Ru/CeO_2/c, both after calcination as well as under reducing conditions. H_2 consumption during TPR shows removal of oxygen equivalent to about 3 monolayers, implying diffusion of vacancies into the subsurface or bulk of CeO_2. The catalyst with the highest concentration of oxygen vacancies is also the most active catalyst, suggesting that reactive adsorption CO_2 at an oxygen vacancy is the rate determining step.

2.1. Introduction

Cerium oxide (CeO_2) is widely used in many catalytic systems for a variety of applications. Ford Motor Company first used CeO_2 as an oxygen storage component in a car exhaust catalytic convertors 40 years ago (1). Since then, CeO_2 has been studied in fuel cells (2), CO oxidation (3), reforming reactions (4), photo-catalysis (5), water-gas-shift reaction (6) and fluid-catalytic-cracking (7). The wide spread of CeO_2 in many catalytic applications is a consequence of its ability to vary the oxygen concentration without changing phase, providing a large and stable capacity for oxygen storage. Hence, CeO_2 not only acts as a catalyst support but it also provides active sites for the adsorption and activation of oxygen-containing molecules.

Well-controlled CeO_2 nanoparticles with very specific shapes are known, including rods (8), cubes (9), wires (10), tubes (11), and spheres (12). In general, these materials allow control over the structure of the exposed surfaces of nanoparticles. CeO_2 cubes (CeO_2/c) with {100}, CeO_2 rods (CeO_2/r) with {111} and CeO_2 octahedra (CeO_2/o) with {111} facets (13) have been most studied for catalytic applications. Catalytic activity of many reactions, including oxidation of organic compounds (14, 15), steam reforming (16), WGS (13), and ammonia synthesis (17) are reported to depend on the morphology and the exposed planes.

In Renewable Energy Roadmap 21, the European Commission is aiming at a 20% share of renewable energy (wind and solar) in the overall energy mix by 2020 (18). However, production of wind and solar energy are often fluctuating and intermittent. Hence, it is required to store this surplus energy for long period of time. Power-to-Gas (PtG) technology is a potential candidate to tackle this issue, since it links the power grid to the existing gas grid by converting surplus electricity into CH_4. There are basically two main steps in this process: H_2 production from H_2O, usually via electrolysis (19) or alternatively plasma-driven dissociation (20) and conversion of H_2 using CO_2 to CH_4 via methanation. Therefore, methanation of CO_2 has become a popular research subject recently (21).

CO_2 methanation is an exothermic reaction ($\Delta H = -165$ kJ/mol) and thermodynamically limited. Low temperature operation not only maximizes conversion but also avoids formation of CO as a product (22). Various metals (Ni, Ru, Co, Rh) and supports (CeO_2, TiO_2, Al_2O_3, SiO_2, ZrO_2, MgO) have been studied for this reaction. Ni and Ru are reported to have maximum activity, selectivity and stability (23). The activity of Ru on reducible supports (CeO_2, TiO_2, ZrO_2) is higher than that on non-reducible supports (Al_2O_3, SiO_2) (24). Lin et. al. (25) reported that Ru on rutile-TiO_2 is more active and stable for CO_2 methanation than Ru on anatase-TiO_2. Le el. al. (26) studied Ni catalyst on various supports (γ-Al_2O_3, SiO_2, TiO_2, CeO_2, and ZrO_2) and reported that the Ni on CeO_2 is most active.

Two types of mechanisms have been suggested for CO_2 methanation. In first route, CO is formed as an intermediate while the second route involves formation of formate as an intermediate, as shown in scheme 2.1. Wang et al (27) observed that, in presence of oxygen vacancies (Ru/CeO_2 catalyst), reaction follows the formate route to form CH_4 via methanol. But in absence of oxygen vacancies (Ru/Al_2O_3 catalyst), reaction proceeds via the CO route. In another study (28), Ren and co-workers studied the mechanism on Ni (111) using DFT and found that the CO route is energetically favorable for CO_2 methanation. In case of Ru-substituted $Ce_{0.95}Ru_{0.05}O_2$, characterization results and DFT calculation predicated that the plausible reaction pathway follows CO route (29). On contrary, Solis-Garcia et. al. (30) proposed that the formate route is favorable in case of Ni/ZrO_2 catalysts. Independent of the two routes suggested, there is a general agreement that reducible supports increase catalytic activity by providing a route for CO_2 activation via interaction with oxygen vacancies (24, 27) which are being restored via reduction of the oxide surface in order to close the catalytic cycle, as shown in scheme 2.1.

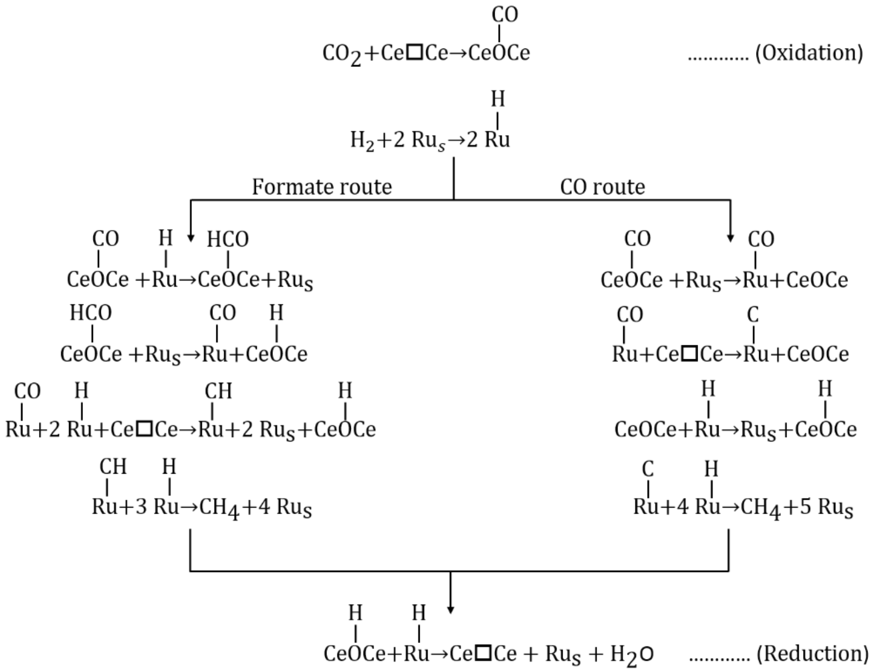

Scheme 2.1: Formate and CO pathways for the mechanism of CO_2 methanation (Ru_s is active site on metal, ☐ is oxygen vacancy).

Wang et. al. (31) studied the structure-activity relationship of Ru/CeO_2 catalysts for CO_2 methanation, reporting that $Ru/CeO_2/c$ is more active than $Ru/CeO_2/r$ and $Ru/CeO_2/o$. In that study, the particle size of Ru on the different shaped CeO_2 nanoparticles was not constant, which may have influenced the results.

In this work, we synthesized CeO_2 with two different morphologies (CeO_2/r and CeO_2/c), exposing facets with {111} and {100} orientation respectively. Commercial CeO_2 (CeO_2/o), mainly exposing {111} facets, is used as a reference (13). To minimize differences in the average Ru particle sizes, the concentration of Ru was adjusted according to the surface area of the support. The catalysts were characterized using electron microscopy (EM), H_2-chemisorption, hydrogen temperature-programmed-reduction (H_2-TPR), Raman spectroscopy, X-ray photoemission spectroscopy (XPS) and carbon dioxide temperature programmed desorption (CO_2-TPD). Here, we report on the effect of Ru on the redox properties of the different CeO_2 nano-shapes and on the correlation of these redox properties with the performance of the catalysts in CO_2 methanation.

2.2. Experimental

2.2.1. Materials

Chemicals including $Ru(acac)_3$ (97%), $Ce(NO_3)_3.H_2O$ (99%) were purchased from Sigma-Aldrich and NaOH (99%) was purchased from Merck Millipore. All the materials were used as received. Deionized water was used in all the experimental processes.

2.2.2. Preparation of CeO_2

Synthesis of CeO_2 was performed using the hydrothermal process reported previously (9, 13). In a typical synthesis, 2.17g of $Ce(NO_3)_3.H_2O$ and 24g of NaOH were dissolved separately in 5ml and 35ml of water respectively. The solutions were mixed slowly and stirred for 30 min. The resulting milky slurry was then transferred into a teflon bottle (125 ml) and filled 80% with water. A teflon bottle was packed in tightly sealed autoclave and hydrothermally treated for 24h at 180^oC or 100^oC to obtain CeO_2/c and CeO_2/r respectively. The resulting precipitate was separated and washed thoroughly with water (until pH became 7) and with ethanol. The samples were dried at 100^oC for 4h, followed by calcination at 500^oC (heating rate: $5^oC/min$) for 5h in air (flow rate: 100 ml/min). CeO_2/o with an average particle size below 50 nm was obtained from Sigma-Aldrich. CeO_2/o was also calcined, at 500^oC (heating rate: $5^oC/min$) for 5h in air (flow rate: 100 ml/min), before use.

2.2.3. Preparation of Ru/CeO_2

Ru/CeO_2 catalysts were prepared by wet impregnation method. Various concentrations of $Ru(acac)_3$ were used, according to the surface area of CeO_2. In a typical synthesis of $Ru/CeO_2/r$, 3g of CeO_2 was dried overnight at 100^oC and added to 40 ml water under stirring. Subsequently, 0.59g of $Ru(acac)_3$ was added and the mixture was stirred at room temperature for 3h. The precipitate obtained was centrifuged and dried at 100°C for 4h. Sample was calcined in flowing air (100 ml/min) at 500°C for 5h at a heating rate of 5°C/min. Two other catalysts were also prepared following the same procedure but using different amounts of $Ru(acac)_3$ (0.38g for $Ru/CeO_2/o$ and 0.25g for $Ru/CeO_2/c$). Identical drying and calcination procedures were used for all three catalysts and the samples were stored under ambient conditions.

2.2.4. Characterization of catalysts

Surface area was determined by N_2-adsorption at -196°C using the BET isotherm (Micromeritics Tristar). The samples were out-gassed in vacuum at 300°C for 24 h prior to analysis. X-ray diffraction (XRD) patterns were recorded using a Bruker D2 powder diffractometer equipped with a position-sensitive detector over a 2θ range between 10° and 90° using Cu Kα radiation, $\lambda = 0.1544$nm. Catalyst morphology was studied by scanning electron microscopy (SEM) ZEISS MERLIN HR-SEM at a working voltage of 1.4 kV. TEM images were obtained on a Philips CM300ST-FEG electron microscope operated at an acceleration voltage of 300kV. Samples for TEM measurements were ultrasonically dispersed in ethanol, and droplets of the suspension were deposited on a copper grid coated with carbon. The Ru loading on the supports was determined by X-ray fluorescence (XRF, Bruker S8 tiger). Raman spectroscopy measurements were performed using a Bruker Senterra Raman spectrometer, equipped with a cooled charge-coupled-device (CCD) detector. Spectra were recorded using a 532nm laser under ambient conditions. The power of the incident beam was 2mW with the exposure time of 1 second. XPS was performed using a PHI QUANTERA SXM spectrometer.

H_2-TPD and H_2-TPR were performed using in-house plug-flow reactor with in-line TCD. For H_2-TPR, about 20mg of sample was placed in a quartz tube and heated to 150°C in Ar. The sample was kept at that temperature for 1h to remove moisture and adsorbed gases. After cooling down to ambient, temperature was again increased to 650°C at 5°C/min in 5%H_2/Ar. H_2 uptake was monitored continuously using a TCD, which was calibrated using NiO as the standard. For H_2-TPD, the catalyst was reduced at 250°C in 5%H_2/Ar during 30 minutes followed by flushing in Ar at the same temperature for 30 minutes. The sample was then cooled down and H_2 was adsorbed at 30°C for 30 min before the gas was changed to Ar to remove physically adsorbed H_2. Finally, the sample was heated to 500°C (heating rate: 20°C/min) in Ar and desorption of H_2 was monitored. Ru particle size, dispersion and surface area were calculated using following equations (32):

Ru metal surface area per gram of catalyst:

$$SA_{Ru}(m^2/g)= \frac{V_{ad}\times SF\times N\times RA}{W_s\times V_m}$$

Ru metal specific surface area per gram of Ru:

$$SA_{Ru}(m^2/g\text{-}Ru)=\frac{SA_{Ru}(m^2/g)}{F_{Ru}}$$

Ru metal dispersion (%):

$$D= \frac{V_{ad}}{W_s}\times\frac{FW_{Ru}\times SF}{F_{Ru}\times V_m}\times 100$$

Ru metal particle size (nm) assuming hemispherical particles:

$$PS=\frac{6\times 10^3}{SA_{Ru}(m^2/g\text{-}Ru)\times d_{Ru}}$$

where V_{ad} is the volume of H_2 adsorbed (ml), SF is stoichiometric factor 0.5 assuming every Ru atom at the surface adsorbs one H atom, N is Avogadro's number, RA is the atomic cross-sectional area of Ru (0.0613 nm^2), W_s is catalyst weight (g), V_m is molar volume of H_2 (22414 ml mol^{-1}), F_{Ru} is weight fraction of Ru in catalysts, FW_{Ru} is molecular weight of Ru and d_{Ru} is density of Ru metal (12.4 g cm^{-3}).

2.2.5. Catalysts Test

Catalytic tests were carried out in a quartz tubular reactor (I.D. = 4 mm) at atmospheric pressure. Temperature and flow rate in the bed was controlled using a thermocouple and calibrated mass flow controllers (MFCs), respectively. For a typical experiment, 50mg of catalyst with particle size 125-250μm was homogeneously mixed with 250mg of glass beads with similar particle size to prevent exothermic heating of the bed. The catalyst was reduced at 250°C (heating rate of 5°C/min) for 2h in a gas mixture of N_2 (75%, v/v) and H_2 (25%, v/v) at 100ml/min of total flow. The system was cooled down to 200°C in N_2 and the gas mixture–containing CO_2 (10%, v/v), H_2 (40%, v/v) and N_2 (50%, v/v)–was introduced into the reactor with a total flow rate of 60ml/min, resulting in a weight-based space velocity of 72000 ml g^{-1} h^{-1}. Product gases were analyzed using an on-line Varian CP-3800 Gas Chromatography equipped with an Agilent CP-Molsieve 5A and PoraPLOT Q column and a TCD. In a typical experiment, the temperature of operation was increased from 200°C, with steps of 25°C, to 400°C. The system was allowed to reach steady state before measuring the CO_2 conversion. It was ensured that no deactivation occurred, by repeating the experiment at 300°C at the end of the experiment. Carbon balance for each experiment was better than 96%. Reaction rates (r) were calculated under differential condition and defined as moles of CO_2 converted per surface area of Ru per second as calculated by following equation:

$$r=\frac{CO_{2_{in}}\times x_{CO_2}}{SA_{Ru}\times W_{cat.}}$$

Where, $CO_{2_{in}}$ is the molar flow of CO_2 at inlet (mol/s), $x_{CO_2}$is fraction of CO_2 converted, SA_{Ru} is active surface area of the Ru per gram catalyst (m^2/g) and $W_{cat.}$ is weight of catalyst (g). It should be noted that internal mass transfer limitations can be ruled out at differential conditions at 250°C or lower temperature, based on the Weisz-Prater criterion.

2.3. Results and discussion

2.3.1. Structural and morphological study

Table 2.1: Structure and physical properties of Ru/CeO_2 with different morphology.

Catalysts	S_{BET} (m^2/g)[a]	CeO_2 crystalline size (nm)[b]	Ru loading (%)[c]	Ru surface area, fresh (m^2/g-cat)	Ru particle size (nm)[d]		Ru dis. (%), Fresh
					Fresh	Spent	
Ru/CeO_2/r	63	13.6	3.7	8.2	2.3	3.1	58
Ru/CeO_2/o	39	19.6	2.2	5.2	2.2	2.3	59
Ru/CeO_2/c	14	36.4	1.5	3.5	2.1	1.9	64

a= measured using N_2-physisorption, b= calculated using Scherrer's eq., c= determined by XRF, d= measured using H_2-TPD.

Figure 2.1 shows the XRD patterns of bare CeO_2 and Ru/CeO_2 with different morphology. All peaks observed can be assigned to the face-centered-cubic fluorite structure of CeO_2 with *Fm-3m* space group (JCPDS 34-0394). Average crystallite sizes of CeO_2 (Table 2.1) were calculated using Scherrer's equation for the most dominant {111} diffraction peak. The trend in the crystallite size agrees well with the trend in surface area of both bare CeO_2 (not shown) and Ru/CeO_2 (Table 2.1). BET surface area of CeO_2 shapes decreases in the order of CeO_2/r > CeO_2/o > CeO_2/c, while the crystal sizes increases in the same order.

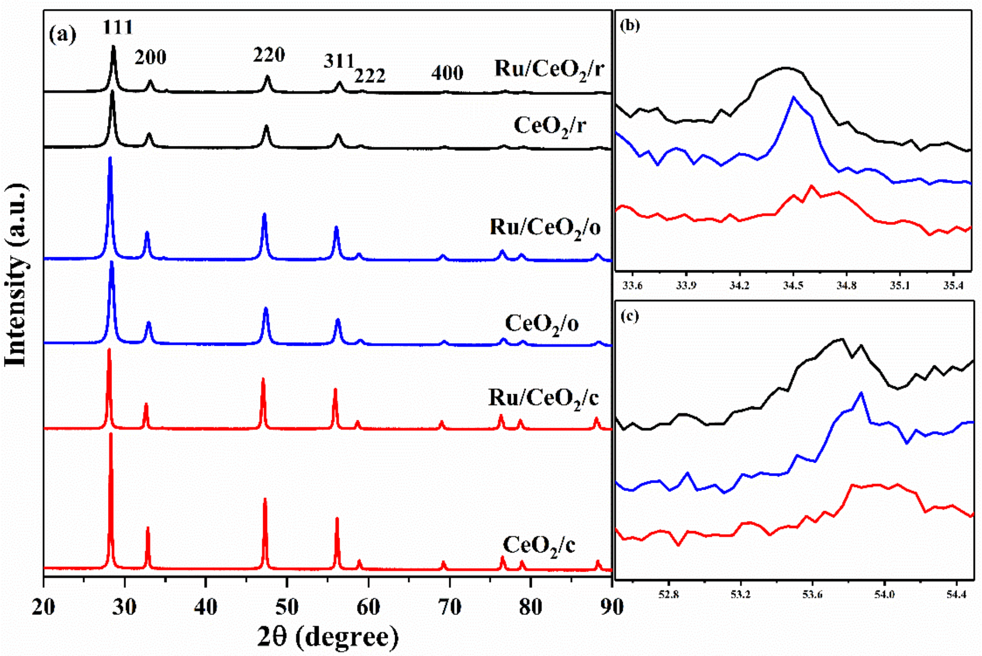

Figure 2.1: XRD patterns (a) of CeO_2 and Ru/CeO_2 catalysts with well-defined facets. Magnified images (b and c) showing RuO_2 peaks around 34 and 54°.

Two additional diffraction peaks around 34° and 54° observed in figure 2.1b and c can be assigned to RuO_2. It is highly dispersed and the peaks are extremely small, hence the averaged crystallite size cannot be estimated. Table 2.1 also presents the BET surface area, Ru loading, Ru metal surface area and averaged metal-particle size of the Ru/CeO_2 samples. It should be noted that the H_2-TPD results are not significantly influenced by any spillover by verifying that longer exposure to H_2 at room temperature did not influence the result. The Ru particle sizes on the three CeO_2 shapes were successfully kept constant despite the different surface areas of the supports, by varying the metal loading.

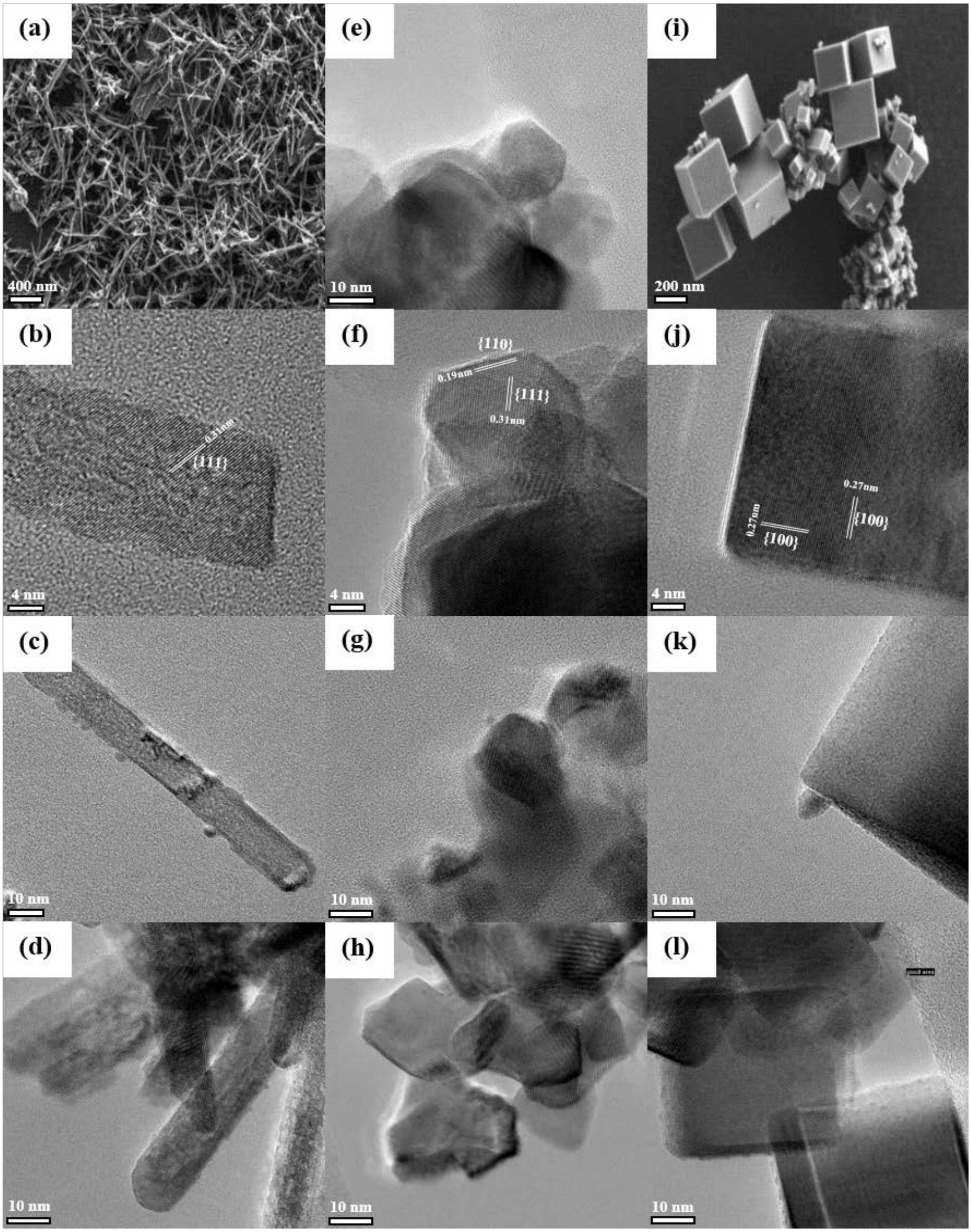

Figure 2.2: SEM images of (a) CeO_2/r, (e) CeO_2/o, (i) CeO_2/c; TEM images of (b) CeO_2/r, (f) CeO_2/o, (g) CeO_2/c; TEM images of RuCeO_2/r (fresh, c and spent, d), Ru/CeO_2/o (fresh, g and spent, h) and Ru/ CeO_2/c (fresh, k and spent, l).

Figure 2.2 represented the electron microscopy results (SEM and TEM). Figure 2.2a exhibits diameters of CeO_2/r between 5 and 10nm as well as lengths of about 200nm, resulting in aspect ratios of more than 20; while particle size of CeO_2/c (Figure 2.2i) ranges between 10 and 200nm. Figure 2.2j display clear {100} lattice fringes for CeO_2/c with interplanar spacing of 0.27nm, while CeO_2/o displayed {111} and {110} lattice fringes (Figure 2.2f) with interplanar spacing of 0.31 and 0.19nm respectively. An interplanar spacing of 0.31nm in CeO_2/r (Figure 2.2b) indicates presence of {111} lattice fringes. Moreover, some dark pits are also observed on CeO_2/r (Figure 2.2c), suggesting there are many defects (13, 17). It has been confirmed with AC-TEM (13) that the exposed facets on CeO_2/c are {100} while CeO_2/r and CeO_2/o expose {111} facets. Wu et. al. (33) reported that the nano-shapes are stable against temperatures up to 500°C, in agreement with the fact that calcination at 500°C is usually applied to obtain well-shapes rods and cubes (34, 35).

Figure 2.2 c, g and k shows no apparent change in the structure of CeO_2 upon Ru loading. Although well disperse Ru particles with typical particle size of 3-4nm are visible on the surface of CeO_2, the number of metal particles measured was insufficient to calculate a significant particle size distribution.

2.3.2. Raman and XPS measurement

Raman spectra of Ru/CeO_2 (Figure 2.3) show a strong F_{2g} mode of CeO_2 fluorite phase at 460cm^{-1} and a weak defect induced mode (D) at 598cm^{-1} (14, 36). Table 2.2 represents the ratio of the peak intensities at 598cm^{-1} and 460cm^{-1} (I_{598}/I_{462}), which is a qualitative measure of oxygen vacancy concentration (37). As this concentration depends on the pretreatment conditions (including drying and calcination), these conditions were kept identical for all the materials. The I_{598}/I_{462} ratio in bare CeO_2 (Table 2.2) dependents on its morphology and decreases in the order of Ru/CeO_2/r > Ru/CeO_2/o > Ru/CeO_2/c. In case of Ru/CeO_2 catalysts, the I_{598}/I_{462} ratio remains morphology dependent with the same order.

Importantly, the I_{598}/I_{462} ratio increases significantly as a result of Ru addition for all shapes.

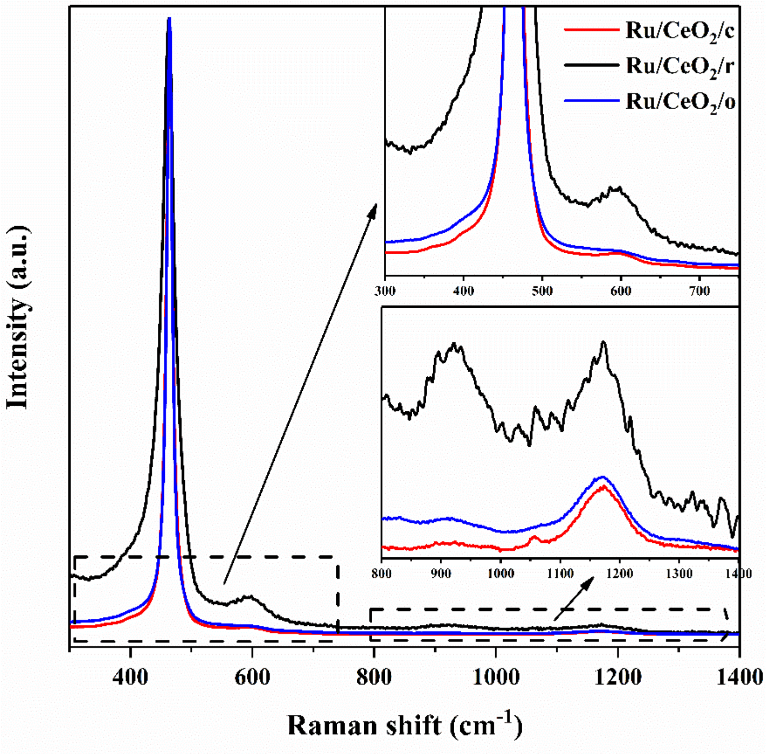

Figure 2.3: Visible Raman spectra of three different Ru/CeO_2 catalysts. Magnified images showing appearance of small peaks due to defects.

In figure 2.3, no bands are detected that could be assigned to RuO_2 (522, 635 and 703cm^{-1}), RuO_3 (800cm^{-1}), RuO_4 (822-881cm^{-1}), RuO_4^{2-} (808cm^{-1}) as well as hydrated RuO_2 (380-440cm^{-1}) (38-41). However, a small band at 950cm^{-1} was detected (inset figure 2.3) which has been assigned to Ru-O-Ce (36, 41). The ratio of peak intensities at 950 and 460cm^{-1} (Table 2.2) therefore is an indication of the interfacial surface area between metal and support, which is decreasing in the order of Ru/CeO_2/r > Ru/CeO_2/c ≥ Ru/CeO_2/o. This order is determined by the Ru loading, because the interfacial surface area scales with the Ru loading, considering that the averaged Ru particle size is constant and assuming that the particle shape in constant as well. In short, the assignment of the Ru-O-Ce peak is consistent with our observations.

Table 2.2: Raman, XPS and CO_2-TPD data of materials.

Samples	Raman		XPS		CO_2 adsorption	
	I_{598}/I_{462}	I_{950}/I_{462}	Ce^{3+}/Ce^{4+}	O_V/O_L	µmol/g	µmol/m^2
CeO_2/r	0.022	-	-	-	425.7	6.1
CeO_2/o	0.021	-	-	-	239.5	5.9
CeO_2/c	0.016	-	-	-	92.8	6.6
Ru/CeO_2/r	0.170	0.058	0.30	0.79	488.1	7.8
Ru/CeO_2/o	0.062	0.028	0.22	0.49	291.5	7.5
Ru/CeO_2/c	0.048	0.020	0.52	0.45	112.9	8.0

Figure 2.4 presents XPS spectra for Ru/CeO_2 catalysts, revealing peaks assigned to O1s, Ru3d and Ce3d. O1s spectra (Figure 2.4a) show two clear oxidation states of surface oxygen. Binding energy at 528.8eV is assigned to lattice oxygen (O_L) and the peak at 530.8eV is characteristic of O^{2-} in oxygen deficient regions (O_V). The O_V/O_L ratio is, therefore, a measure for the concentration of surface oxygen vacancies on CeO_2 nanoparticles (17, 36, 42). Table 2.2 shows that the ratio of O_V/O_L decreases in the order of Ru/CeO_2/r > Ru/CeO_2/o ≥ Ru/CeO_2/c.

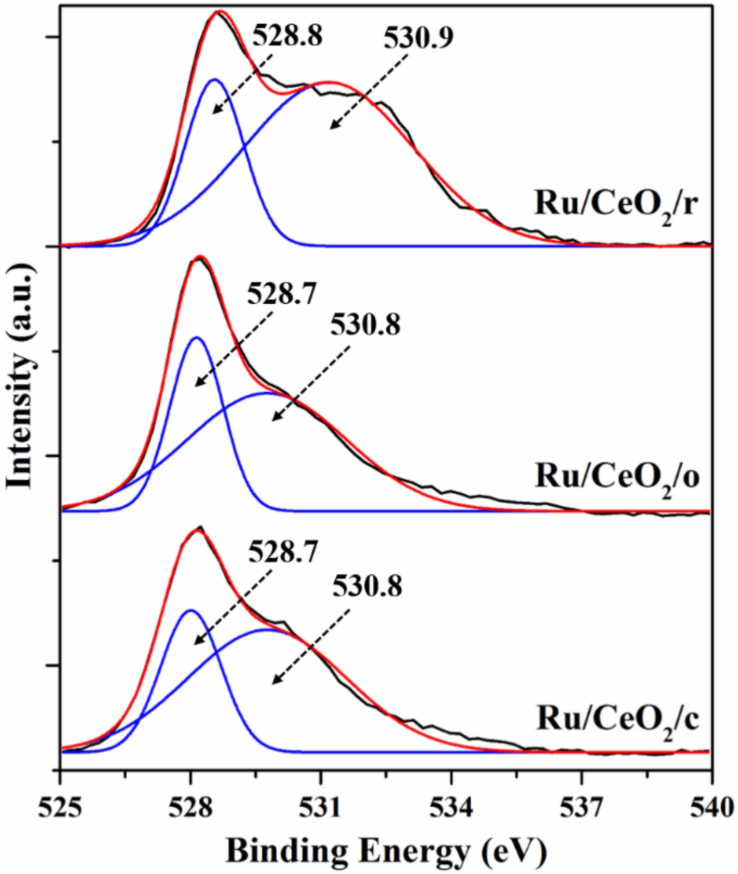

Figure 2.4: Deconvolution of XPS of O 1s for three different Ru/CeO$_2$ catalysts. Black, red and blue lines indicate original spectra, fitted data, and deconvoluted peak, respectively.

Peaks for different oxidation states of Ru (Figure 2.5) were assigned based on literature and Gaussian fitting was used for deconvolution. Table S2.1 presents an overview of the peak positions as reported in literature including standard deviations. Hence, the peak positions were allowed to vary during deconvolution (typically ±0.3eV) based on the variation in literature data. The spectra show three Ru 3d$_{5/2}$ peaks at 280.2 ±0.3, 281.6 ±0.3 and 284.3 ±0.2eV, assigned to the presence of Ru^0, Ru^{4+} and Ru^{6+}, respectively (43, 44). A broad peak around 288eV is a characteristic peak of carbon resulting from the sample holder.

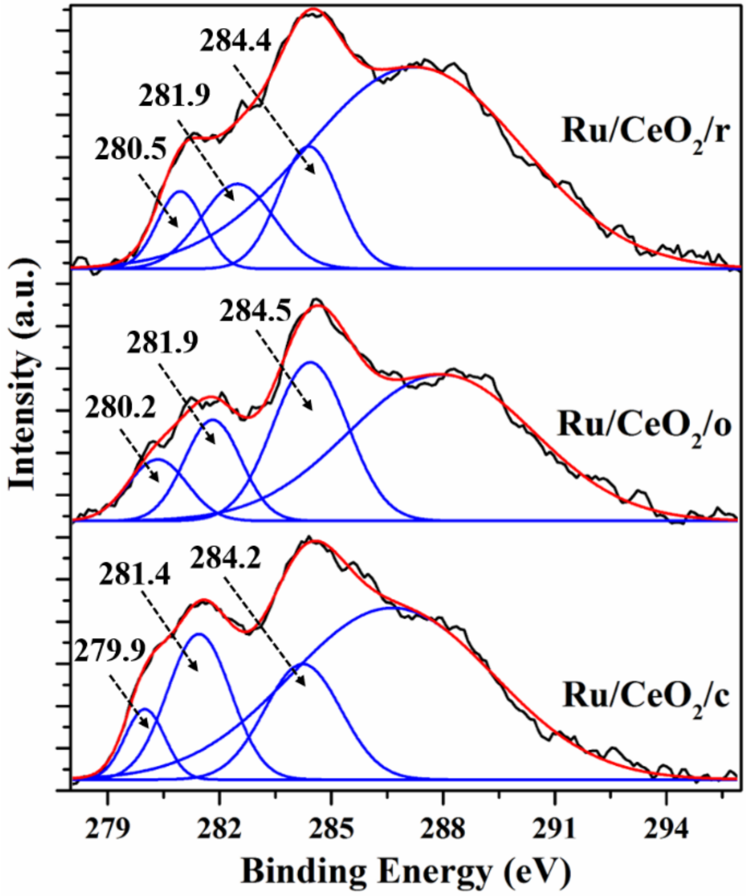

Figure 2.5: Deconvolution of XPS of Ru 3d for three different Ru/CeO_2 catalysts. Black, red and blue lines indicate original spectra, fitted data, and deconvoluted peak, respectively.

Ten different peaks are expected for Ce based on literature (Table S2.2) and indeed figure 2.6 shows a complex peak pattern. Many of the peaks are strongly overlapping, requiring deconvolution using Gaussian fitting. Also in this case, the peaks positions were allowed to vary by typically ±0.7eV. Six of the ten peaks (with binding energy of 881.8 ±0.3, 888 ±0.1, 897.8 ±0.5, 900 ±0.1, 907.2 ±0.4, 916.4 ±0.4eV) can be assigned to Ce^{4+} oxidation state while the remaining peaks (at 880.9, 883.6 ±0.3, 898.5 ±0.5, 901.8 ±0.7eV) arise from Ce^{3+} oxidation state (45). The ratio of the cumulative intensities of all peaks assigned to Ce^{3+} and the cumulative intensities of all peaks assigned to Ce^{4+} is a measure for the Ce^{3+}/Ce^{4+} atomic ratio, as shown in Table 2.2. It shows that Ru/CeO_2/c has the highest Ce^{3+}/Ce^{4+} atomic ratio among the three catalysts followed by Ru/CeO_2/r and Ru/CeO_2/o. Presence of Ce^{3+} is either associated with generation of oxygen vacancies (17, 36) or OH groups on the surface due to adsorption of water in ambient (46).

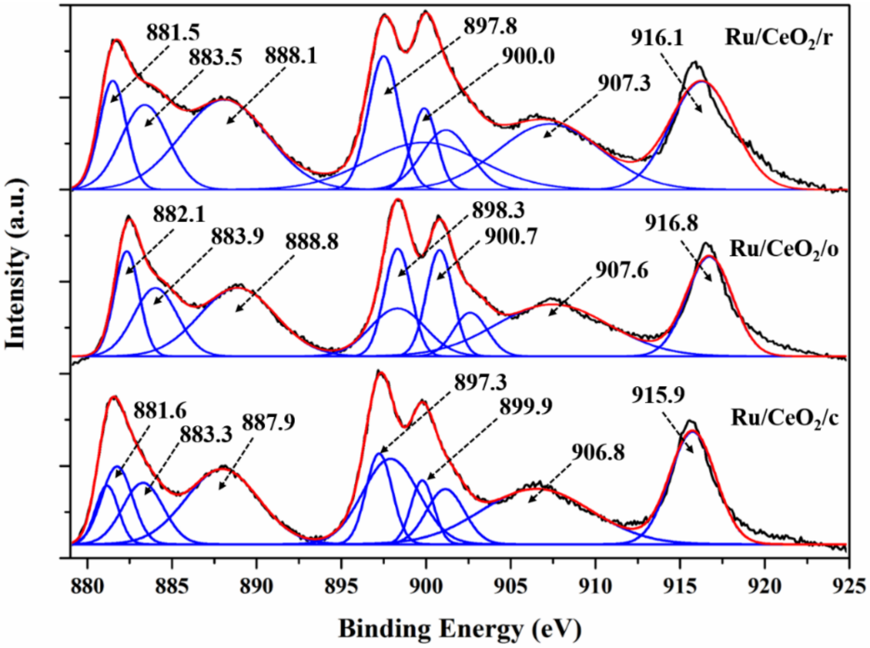

Figure 2.6: Deconvolution of XPS of Ce 3d for three different Ru/CeO_2 catalysts. Black, red and blue lines indicate original spectra, fitted data, and deconvoluted peak, respectively.

2.3.3. H_2-TPR and CO_2-TPD analysis

Reducibility of CeO_2 and Ru/CeO_2 samples was investigated using H_2-TPR (Figure 2.7). It is generally accepted (17, 31) that the reduction peaks below 500°C stem from surface reduction of CeO_2. Figure 2.7 shows maxima at 375°C for CeO_2/c and about 500°C for both CeO_2/o and CeO_2/r. Relative high reactivity of surface oxygen on CeO_2/c is in agreement with the suggestion (47, 48) that the oxygen terminated {100} plane is more accessible and less stable compared to the other surfaces. Bulk reduction of CeO_2 is reported to proceed above 600°C (17, 31), in essence outside the window of observation in figure 2.7, preventing the nanoparticles to lose their specific shapes. H_2 consumption on bare CeO_2, forming oxygen vacancies, was calculated by integrating the TPR signal between 350-550°C. This H_2 consumption, per unit mass of support, decreases in the order CeO_2/r > CeO_2/o > CeO_2/c (Table 2.3). Table 2.3 also shows that the extent of surface reduction, i.e. H_2 consumption per unit surface area of CeO_2, decreases in the same order. All three samples allow removal of oxygen in the order of a sub-monolayer (0.3-0.8 ML), which might be confined to the sub-surface. In short, CeO_2/r reduces deeper compared to cubes and octahedra, despite their high surface area.

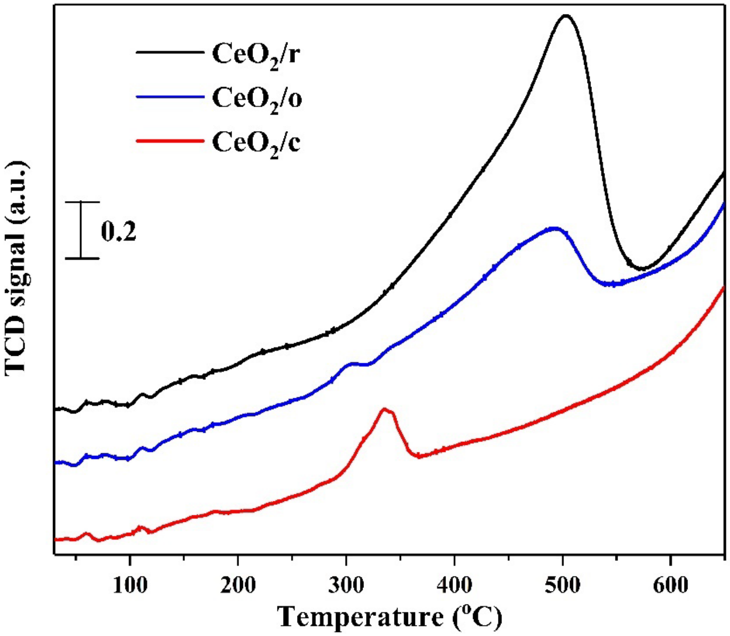

Figure 2.7: H_2-TPR profile of three bare CeO_2 supports. (Wt. of catalysts: 20mg, heating rate: 5°C/min).

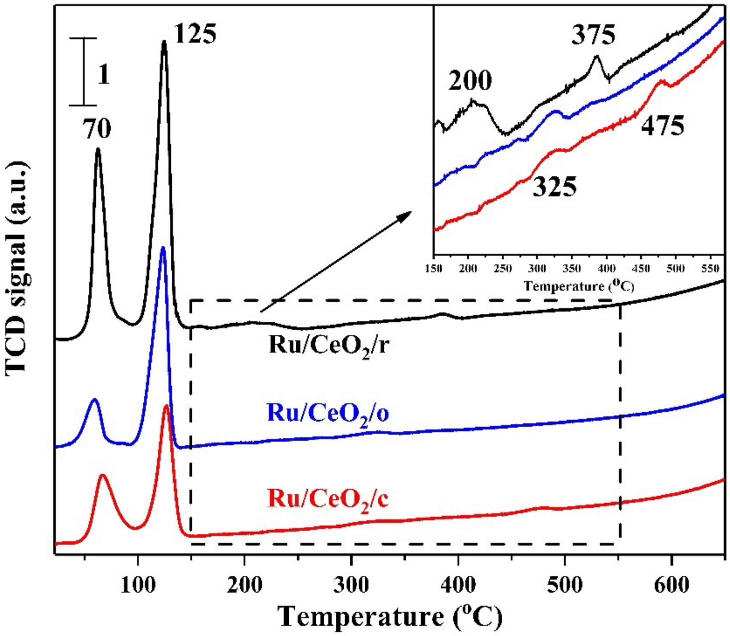

Figure 2.8: H_2-TPR profile of three different Ru/CeO_2 catalysts. (Wt. of catalysts: 20mg, heating rate: 5^{o}C/min).

Two sharp peaks at 75 and 125^{o}C in TPR (Figure 2.8) of Ru/CeO_2 have been assigned to the reduction of RuO_2 with different strengths of interaction with CeO_2 (31, 49). The total H_2 consumption during the reduction of these catalysts was calculated by integrating all peaks, greatly exceeding the H_2 consumption associated with complete reduction of RuO_2 (Table 2.3), with a factor of about 5. This indicates significant H_2 spillover to the CeO_2 support during reduction of RuO_2, either generating oxygen vacancies, and/or generating surface OH groups. H_2 consumption caused by reduction of CeO_2 in Ru/CeO_2 is much higher than for bare CeO_2 and rods (Ru/CeO_2/r) consumes much more H_2 than the other shapes, because of its higher surface area. However, surface area normalized H_2 consumption decreases in the order of Ru/CeO_2/c > Ru/CeO_2/r > Ru/CeO_2/o (Table 2.3). Total H_2 consumption for CeO_2 reduction, assuming negligible contribution from OH formation, accounts for typically 2 to 3 ML for all shapes. Inset of figure 2.8 shows two small peaks at high temperature, resulting from the reduction of CeO_2 surface. It is suggested that (36, 50) these peaks belong to the reduction of surface oxygen species remote from metal particles.

Table 2.3: H_2 consumption based on TPR for CeO_2 as well as Ru/CeO_2 catalysts.

Samples	LT H_2 consumption (µmol/g)		HT H_2 consumption	H_2 consumption during CeO_2 reduction	
	Theoretical[a]	Experimental	(µmol/g)	(µmol/$m^2_{cat.}$)[b]	(µmol/g)
CeO_2/r	-	-	592.1	9.4	592.1
CeO_2/o	-	-	198.6	5.1	198.6
CeO_2/c	-	-	103.6	7.4	103.6
Ru/CeO_2/r	557.7	2460.8	73.3	31.4	1976.4
Ru/CeO_2/o	330.8	1387.6	2.7	27.2	1059.5
Ru/CeO_2/c	225.6	1245.7	15.8	74.0	1035.9

LT: Low temperature (Peaks=75, 125°C), HT: High temperature (Peaks=330-500°C), a= calculated assuming complete reduction $RuO_2+2H_2=Ru+2H_2O$, b= H_2 consumption due to CeO_2 reduction (normalized per m^2 of catalysts).

Figure 2.9 presents CO_2-TPD results on Ru/CeO_2 catalysts, showing two desorption peaks between 100-200 and 300-500°C attributed to weak and moderate basic sites, respectively (51). Total quantity of CO_2 adsorption is summarized in Table 2.2. The amount of CO_2 normalized to the surface area is constant on all three catalysts. Ru seems to increase the amount of CO_2 adsorption slightly for all shapes compared to bare CeO_2. CeO_2/o contains relatively weaker basic sites than CeO_2/r and CeO_2/c, based on ratio of the peak intensities at 150 and 350°C.

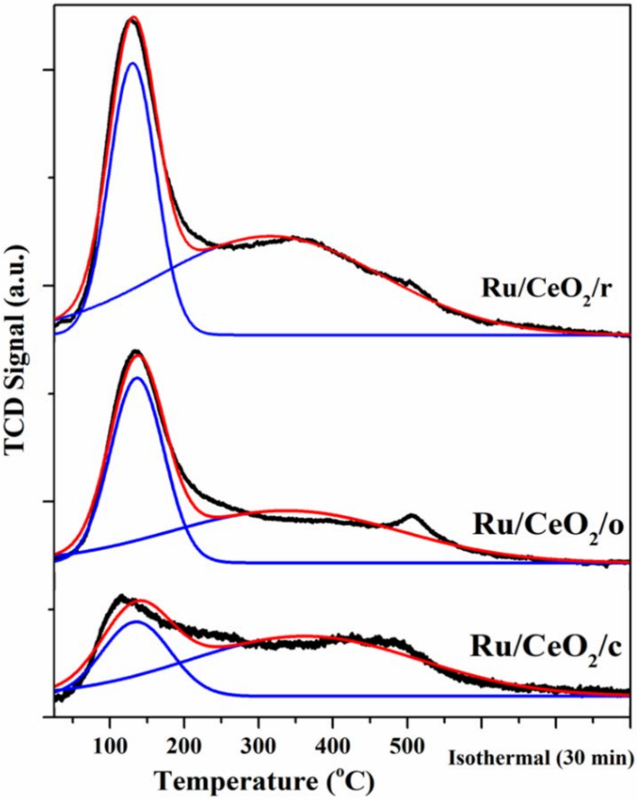

Figure 2.9: CO_2-TPD profile of three different Ru/CeO_2 catalysts. (Wt. of catalysts: 20mg, heating rate: 20°C/min).

2.3.4. Catalytic performance

Performance of catalysts was evaluated in the temperature range between 200 and 400°C. Figure 2.10 shows the CO_2 conversion vs temperature while reaction rate per m^2 of Ru at low conversion is shown in figure 2.11. At 250°C, Ru/CeO_2/r is more active (11.0×10^{-8} mol $s^{-1}m^{-2}_{Ru}$) than Ru/CeO_2/o (7.2×10^{-8} mol $s^{-1}m^{-2}_{Ru}$) and Ru/CeO_2/c (5.1×10^{-8} mol $s^{-1}m^{-2}_{Ru}$). Clearly, this must be an effect of the structure of the support as otherwise the activity expressed per unit Ru surface area would have remained unchanged despite the differences in Ru loading. Ru/CeO_2/r is more active than other two catalysts at higher temperatures as well. Selectivity to CH_4 was higher than 99% in all cases.

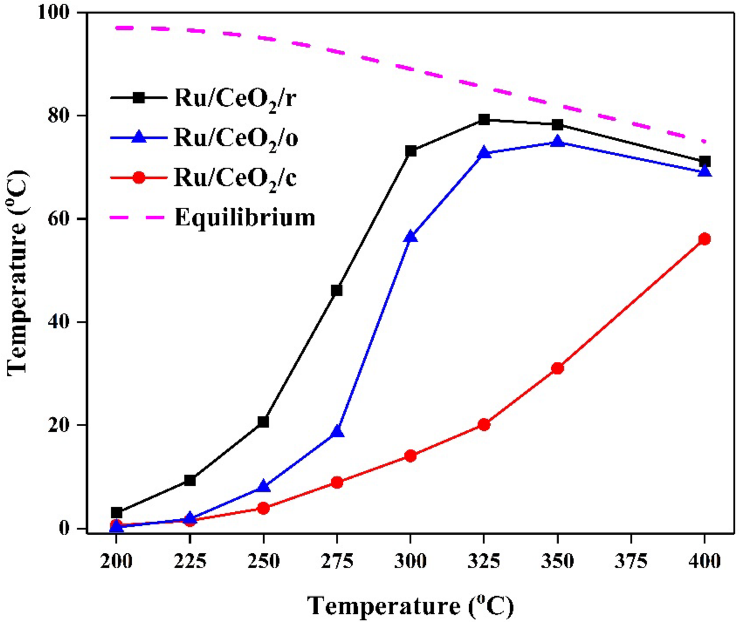

Figure 2.10: CO_2 conversion of three different Ru/CeO_2 catalysts (Cat. wt.: 50mg, GHSV: 72 l g^{-1} h^{-1}, conversion < 20%).

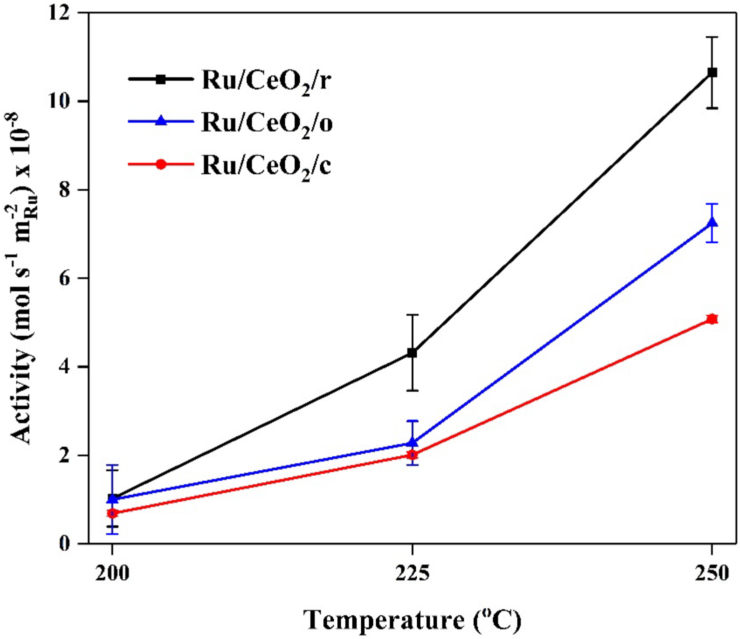

Figure 2.11: Activity of three different Ru/CeO_2 catalysts at differential experiments conditions (Cat. wt.: 50mg, GHSV: 72 l g^{-1} h^{-1}, conversion < 20%).

All three catalysts are stable for 24h time on stream at 350°C (Figure 2.12). Furthermore, as catalysts have been reduced at 250°C before both the catalyst test as well as the TPD experiment, it is reasonable to assume that no sintering will occur during testing at 250°C and lower temperatures. Stability of the catalyst is further supported by the observation that the Ru particle size, based on H_2-TPD (Table 2.1), increases only marginally during catalytic testing up to 400°C for $Ru/CeO_2/r$, whereas no sintering is observed for $Ru/CeO_2/c$ and $Ru/CeO_2/o$. Sintering of Ru is observed exclusively at high reduction temperature (500°C). Morphology of the catalysts also showed no change during catalytic testing according TEM images (Figure 2.2 d, h, l). In short, the catalytic data at temperatures up to 250°C are not influenced by any deactivation.

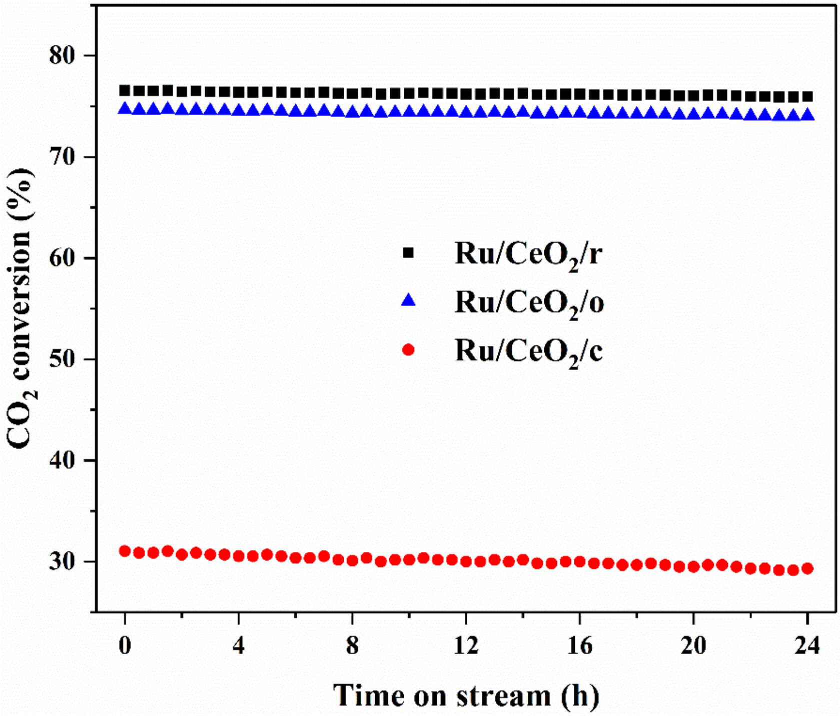

Figure 2.12: Long-term activity of catalysts at 350°C (Cat. wt.: 50mg, GHSV: 72 l g^{-1} h^{-1}, conversion < 20%).

2.4. General Discussion

In this study, we have successfully prepared a series of Ru/CeO_2 catalysts with three different morphologies of CeO_2. Particle size of Ru was kept constant despite the varying surface area of CeO_2. Figure 2.11 presents the activity of the three catalysts at mild temperatures; the activity is best evaluated using the data points obtained at 225°C because the conversion is below 10%, in contrast to data obtained at any higher temperature, and because the accuracy is superior to the data at 200°C. The activity of Ru/CeO_2/r is significantly higher than both Ru/CeO_2/o and Ru/CeO_2/c, as also shown in figure 2.11. Previous study (31) on Ru/CeO_2-nanoshapes for CO_2 methanation reported highest activity for Ru/CeO_2/c, compared to Ru/CeO_2/r and Ru/CeO_2/o, using catalysts with Ru particle sizes varying between 1.8 and 3.7 nm. These experiment were done at much lower GHSV so that differential conditions are achieved only at much lower temperature; nevertheless, high activity of Ru/CeO_2/c compared to Ru/CeO_2/r is observed at all temperatures, in contrast to the results in this study.

This is suggesting that the Ru particle size influences the activity of the catalysts and influences the effects of the CeO_2 morphology as reported in (31). Although there is, to the best of our knowledge, no direct evidence for particle size effect for Ru/CeO_2 for CO_2 methanation, this hypothesis is supported indirectly by a number of claims in the literature. Iablokov et. al. (52) reported that in case of supported Co catalysts with particle sizes between 3 and 10 nm, turnover frequency (TOF) indeed increases with increasing particle size for CO_2 hydrogenation reaction. In another study, the selectivity to CH_4 increases with increasing Ru particle size during CO_2 methanation on Ru/Al_2O_3 (53). Recently, Vogt et.al (54) also reported that the activity for CO_2 methanation follows volcano-curve with increasing particle size for Ni/SiO_2 catalysts. Peng at.al (50) reported that the activity of Pt/CeO_2 catalysts for oxidation of toluene increases with Pt particle size. In any case, the data obtained in this study cannot be compromised by any Ru particle size effect, as the Ru particle size was constant.

In general, pretreatment and experimental conditions influence the concentration of oxygen vacancies in CeO_2. However, by keeping these conditions identical, e.g. by applying identical calcination procedures, it is possible to compare the results obtained on different samples qualitatively. The H_2 consumption during TPR (Figure 2.7) was higher for CeO_2/r compared to CeO_2/c and CeO_2/o. Raman results (Table 2.2) indicate that the initial oxygen vacancy concentration in all bare calcined CeO_2 samples was similar. Thus, the difference in the reducibility according TPR is not caused by differences in the initial oxygen vacancy concentration and is reflecting the reducibility. Furthermore, CeO_2/c reduces at lower temperature compared to CeO_2/r and CeO_2/o. This is in agreement with the fact that CeO_2/c contains relatively unstable oxygen in the {100} surface plane (55), which is thermodynamically relatively easy to reduce.

Ru addition causes a significant increase in the oxygen vacancy concentration in CeO_2 according Raman measurements of unreduced samples (Table 2.2). This might result from the interaction of RuO_x and CeO_2 at the interface (41). The oxygen vacancy concentration, according to Raman, decreases in the order of Ru/CeO_2/r > Ru/CeO_2/o > Ru/CeO_2/c. The trend in the O_V/O_L ratio (Table 2.2) obtained from XPS experiments, representing the oxygen vacancy concentration, agrees well with above trend. However, the ratio of Ce^{3+}/Ce^{4+} (also obtained from XPS) does not follow the same trend. Therefore, the presence of Ce^{3+} is, at least partly, not connected to the presence of oxygen vacancies. Ce^{3+} can also result from the presence surface OH groups and/or carbonate species. This qualitatively agrees with the fact that CeO_2/c favors the formation OH and carbonates as compared to CeO_2/o and CeO_2/r (46). Summarizing, high concentration Ce^{3+} and low O_V/O_L in Ru/CeO_2/c is suggesting higher concentration of OH and/or carbonate groups and lower concentration oxygen vacancy compared to Ru/CeO_2/r and Ru/CeO_2/o. These surface-OH groups might also be responsible for reduction of bare CeO_2/c at mild conditions, as discussed in the previous paragraph.

Addition of Ru lowers the reduction temperature of surface CeO_2 to below 150°C (Figure 2.8), indicating a classical spillover mechanism. Also, the extent of reduction increases significantly compared to bare CeO_2. The amount of H_2 consumed is equivalent to removal of typically 3 ML of oxygen on Ru/CeO_2, compared to only 0.6 ML on bare CeO_2. Clearly, these effects cannot be attributed to only formation of surface-OH or generation of surface oxygen vacancies, or a combination of both effects. At the other hand, the O_V/O_L ratio according XPS (Table 2.2) suggests that vacancy diffusion to the subsurface of CeO_2 is contributing significantly.

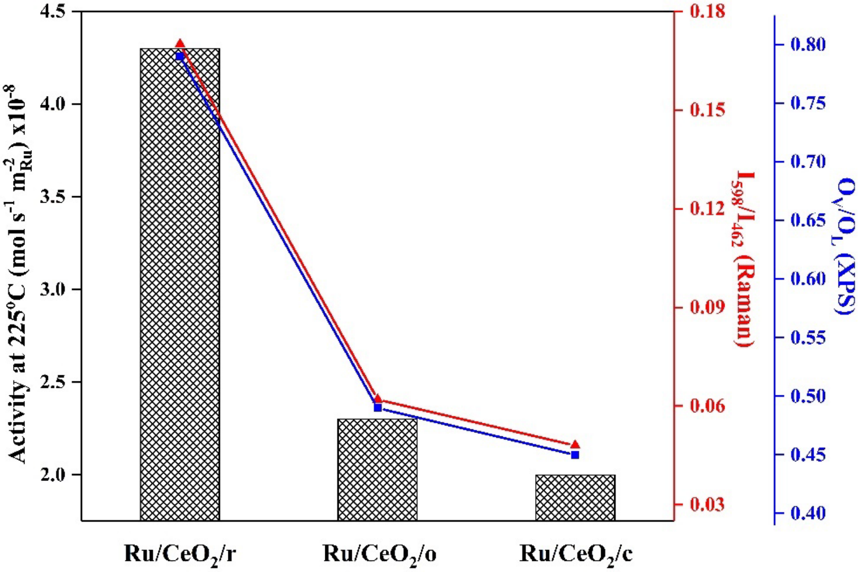

Figure 2.13: Correlation between the activity (at 225°C) and oxygen vacancy concentration of catalysts.

All three catalysts showed good stability by maintaining the Ru dispersion until 250°C, CeO_2 morphology and the catalytic performance during the experiment. Therefore, it seems reasonable to assume that the dispersion measured for the fresh catalysts are a reasonable measure for the dispersion during the catalytic operation. Activity of the catalysts varies greatly in the order Ru/CeO_2/r > Ru/CeO_2/o > Ru/CeO_2/c, as discussed above. This order in activity correlates with the order in the oxygen vacancy concentration after calcination, as can be referred from both Raman spectroscopy (I_{598}/I_{460} ratio, Table 2.2) as well as XPS (O_V/O_L ratio, Table 2.2), both indicating a significantly higher concentration in Ru/CeO_2/r. Figure 2.13 shows that the trend in activity at 225°C, at differential conditions, correlates well with the trend in vacancy concentration obtained from Raman and XPS. Reduction during TPR is resulting in the same trend.

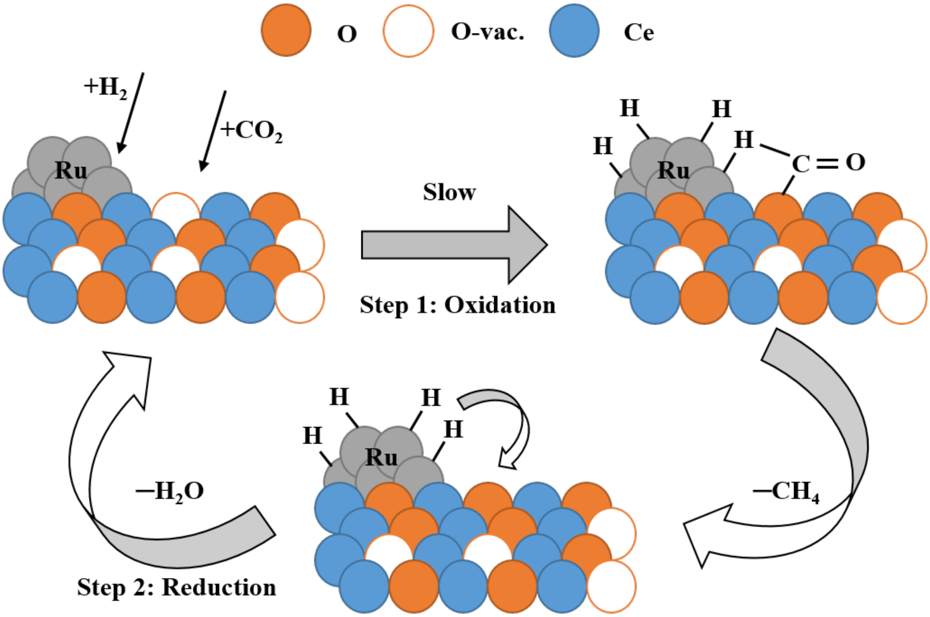

Figure 2.14: Proposed mechanism for the reaction.

The correlation between oxygen vacancy concentration and activity is of course not causal because the actual vacancy concentration during catalysis in a specific catalyst is determined by the reduction-oxidation properties of the reaction mixture at the temperature applied. The generally accepted mechanism for CO_2 methanation on Ru supported on reducible oxides in figure 2.14 involves two key steps, i.e. CO_2 activation by filling an oxygen vacancy (oxidation of the support, step 1) and the regeneration of oxygen vacancy by H_2 (reduction of the support, step 2). It is reasonable to assume that the same order in vacancy concentration also applies at reaction conditions. This argument is independent of the ongoing debate on the more detailed reaction pathway in Scheme 1, i.e. via CO or via formate. The catalyst generating oxygen vacancies most easily exhibits the highest catalytic activity, indicating that activation of CO_2 on oxygen vacancies is the rate determining step.

2.5. Conclusions

This study reports on the influence of the morphology of CeO_2 supports on Ru catalysts for CO_2 methanation, keeping the Ru particle size constant. Addition of Ru promotes the reducibility, increasing the oxygen vacancy concentration comparted to bare CeO_2. TPR, Raman and XPS results demonstrated that the Ru/CeO_2/r contains much more oxygen vacancies compared to Ru/CeO_2/o and Ru/CeO_2/c, both in oxidizing and in reducing conditions. Ru/CeO_2/r, with the highest oxygen vacancy concentration, is the most active catalyst for CO_2 methanation. This suggests that the oxidation step (oxygen vacancy filling by CO_2) is the rate-determining step in the redox cycle.

References

1. Tiziano Montini, Michele Melchionna, Matteo Monai, Paolo Fornasiero. *Chem. Rev.* **2016**, 116, 5987-6041.
2. E. Perry Murray, T. Tsai, S. A. Barnett. *Nature* **1999**, 400, 649-651.
3. Marco Piumetti, Tahrizi Andana, Samir Bensaid, Debora Fino, Nunzio Russo, Raffaele Pirone. *AIChE J.* **2017**, 63, 216-225.
4. Xianjun Du, Dengsong Zhang, Liyi Shi, Ruihua Gao, Jianping Zhang. *J. Phys. Chem. C* **2012**, 116, 10009-10016.
5. M. Melchionna, P. Fornasiero. *Mater. Today* 2014, 17, 349-357.
6. Julia Vecchietti, Adrian Bonivardi, Wenqian Xu, Dario Stacchiola, Juan J. Delgado, Monica Calatayud, Sebastián E. Collins. *ACS Catal.* **2014**, 4, 2088-2096.
7. Mehdi Dejhosseini, Tsutomu Aida, Masaru Watanabe, Seiichi Takami, Daisuke Hojo, Nobuaki Aoki, Toshihiko Arita, Atsushi Kishita, Tadafumi Adschiri. *Energy Fuels* **2013**, 27, 4624-4631.
8. P.X. Huang, F. Wu, B.L. Zhu, X.P. Gao, H.Y. Zhu, T.Y. Yan, W.P. Huang, S.H. Wu, D.Y. Song. *J. Phys. Chem. B* **2005**, 109, 19169-19174.
9. Hao-Xin Mai, Ling-Dong Sun, Ya-Wen Zhang, Rui Si, Wei Feng, Hong-Peng Zhang, Hai-Chao Liu, Chun-Hua Yan. *J. Phys. Chem. B* **2005**, 109, 24380-24385.
10. Chengsi Pan, Dengsong Zhang, Liyi Shi, Jianhui Fang. *Eur. J. Inorg. Chem.* **2008**, 2429-2436.
11. Wei-Qiang Han, Lijun Wu, Yimei Zhu. *J. Am. Chem. Soc.* **2005**, 127, 12814-12815.
12. Chunman Ho, Jimmy C. Yu, Tszyan Kwong, Angelo C. Mak, Sukyin Lai. *Chem. Mater.* **2005**, 17, 4514-4522.
13. Shilpa Agarwal, Leon Lefferts, Barbara L. Mojet, D. A. J. Michel Ligthart, Emiel J. M. Hensen, David R. G. Mitchell, Willem Erasmus, Bruce Anderson, Ezra Olivier, Johannes H. Neethling, Abhaya Datye. *ChemSusChem* **2013**, 6, 1898-1906.
14. Qiguang Dai, Hao Huang, Yu Zhu, Wei Deng, Shuxing Bai, Xingyi Wang, Guanzhong Lu. *Appl. Catal. B* **2012**, 117–118, 360-368.

15. Laura Torrente-Murciano, Alexander Gilbank, Begona Puertolas, Tomas Garcia, Benjamin Solsona, David Chadwick. *Appl. Catal. B* **2013**, 132–133, 116-122.
16. Wang Hong, Zhang Lijuan, L. Miao, Li Yuan, Bai Xue. *J. Rare Earths* **2013**, 31, 565-571.
17. Zhanwei Ma, Shengli Zhao, Xiaoping Pei, Xumao Xionga, Bin Hu. Catal. *Sci. Technol.* **2017**, 7, 191-199.
18. EU Roadmap. Mapping Renewable Energy Pathways towards 2020. EREC **2011**.
19. Karim Ghaib, Fatima-Zahrae Ben-Fares. *Renewable and Sustainable Energy Rev.* **2018**, 81, 433-446.
20. Xiao Chen, Steven L. Suib, Yuji Hayashi, Hiroshige Matsumoto. *J. Catal.* **2001**, 201, 198-205.
21. M.A.A. Aziz, A.A. Jalil, S. Triwahyono, A. Ahmad. *Green Chem.* **2015**, 17, 2647-2663.
22. Xiong Su, Jinghua Xu, Binglian Liang, Hongmin Duan, Baolin Hou, Yanqiang Huang. *J. Energy Chem.* **2016**, 25, 553-565.
23. Inga Kuznecova, Julija Gusca. *Energy Procedia* **2017**, 128, 255-260.
24. Shohei Tada, Teruyuki Shimizu, Hiromichi Kameyama, Takahide Haneda, Ryuji Kikuchi. *Int. J. Hydrogen Energy* **2012**, 37, 5527-5531.
25. Qingquan Lin, Xiao Yan Liu, Ying Jiang, Yong Wang, Yanqiang Huang, Tao Zhang. *Catal. Sci. Technol.* **2014**, 4, 2058-2063.
26. Thien An Le, Min Sik Kim, Sae Ha, Lee Tae Wook Kim, Eun Duck Park. *Catal. Today* **2017**, 293–294, 89-96.
27. Fei Wang, Shan He, Hao Chen, Bin Wang, Lirong Zheng, Min Wei, David G. Evans, Xue Duan. *J. Am. Chem. Soc.* **2016**, 138, 6298-6305.

28. Jun Ren, Hailong Guo, Jinzhou Yang, Zhifeng Qin, Jianying Lin, Zhong Li. *Appl. Surf. Sci.* **2015**, 351, 504-516.
29. Sudhanshu Sharma, K. B. Sravan Kumar, Yash M. Chandnani, V. Sai Phani Kumar, Bhanu P. Gangwar, Aditi Singhal, Parag A. Deshpande. *J. Phys. Chem. C* **2016**, 120, 14101-14112.

30. Alfredo Solis-Garcia, Jose F. Louvier-Hernandez, Armando Almendarez-Camarillo, Juan C. Fierro-Gonzalez. *Appl. Catal. B* **2017**, 218, 611-620.
31. Fei Wang, Changming Li, Xiaoyu Zhang, Min Wei, David G. Evans, Xue Duan. *J. Catal.* **2015**, 329, 177-186.
32. Subramani Velu, Santosh K. Gangwal. *Solid State Ionics* **2006**, 177, 803-811.
33. Zili Wu, Meijun Li, Jane Howe, Harry M. Meyer III, Steven H. Overbury. *Langmuir* **2010**, 26, 16595-16606.
34. Ning Wang, Weizhong Qian, Wei Chu, Fei Wie. *Catal. Sci. Technol.* **2016**, 6, 3594-3605.
35. Sujie Chang, Mo Li, Qing Hua, Lijuan Zhang, Yunsheng Ma, Bangjiao Ye, Weixin Huang. *J. Catal.* **2012**, 293, 195-204.
36. Hao Huang, Qiguang Dai, Xingyi Wang. *Appl. Catal. B* **2014**, 158–159, 96-105.
37. Lianjun Liu, Zhijian Yao, Yu Deng, Fei Gao, Bin Liu, Lin Dong. *ChemCatChem* **2011**, 3, 978-989.
38. Ho Yeung H Chan, Christos G Takoudis, Michael J Weaver. *J Catal.* **1997**, 172, 336-345.
39. N. Weinstock, H. Schulze, A. Müller. *J. Chem. Phys.* **1973**, 59, 5063-5067.
40. Hyun Chol Jo, Kyung Moon Kim, Hyeonsik Cheong, Se-Hee Lee, Satyen K. Deb. Electrochem. *Solid-State Lett.* **2005**, 8, E39-E41.
41. Atsushi Satsuma, Masatoshi Yanagihara, Junya Ohyama, Kenichi Shimizu. *Catal. Today* **2013**, 201, 62-67.
42. Zong Hu, Xiaofei Liu, Dongmei Meng, Yun Guo, Yanglong Guo, Guanzhong Lu. *ACS Catal.* **2016**, 6, 2265-2279.
43. Qiguang Dai, Shuxing Bai, Zhengyi Wang, Xingyi Wang, Guanzhong Lu. *Appl. Catal. B* **2012**, 126, 64-75.
44. Kwangsup Kim, Nicholas Winograd. *J. Catal.* **1974**, 35, 66-72.
45. Klaus-Dieter Schierbaum. *Surf. Sci.* **1998**, 399, 29-38.
46. Shilpa Agarwal, Leon Lefferts, Barbara Mojet. *ChemCatChem* **2013**, 5, 479-489.
47. Daniel G. Araiza, Antonio Gómez-Cortés, Gabriela Díaz. *Catal. Sci. Technol.* **2017**, 7, 5224-5235.

48. Shilpa Agarwal, X. Zhu, Emiel J. M. Hensen, Barbara Mojet, Leon Lefferts. *J. Phys. Chem. C* **2015**, 119, 12423-12433.

49. Samer Aouad, Edmond Abi-Aad, Antoine Aboukaïs. *Appl. Catal. B* **2009**, 88, 249-256.

50. Ruosi Peng, Shujun Li, Xibo Sun, Quanming Ren, Limin Chen, Mingli Fu, Junliang Wu, Daiqi Ye. *Appl. Catal. B* **2018**, 220, 462-470.

51. Shengping Wang, Lifang Zhao, Wei Wang, Yujun Zhao, Guanglin Zhang, Xinbin Ma, Jinlong Gong. *Nanoscale* **2013**, 5, 5582-5588.

52. Viacheslav Iablokov, Simon K. Beaumont, Selim Alayoglu, Vladimir V. Pushkarev, Colin Specht, Jinghua Gao, A. Paul Alivisatos, Norbert Kruse, Gabor A. Somorjai. *Nano Lett.* **2012**, 12, 3091-3096.

53. Ja Hun Kwak, Libor Kovarik, János Szanyi. *ACS Catal.* **2013**, 3, 2449-2455.

54. Charlotte Vogt, Esther Groeneveld, Gerda Kamsma, Maarten Nachtegaal, Li Lu, Christopher J. Kiely, Peter H. Berben, Florian Meirer, Bert M. Weckhuysen. *Nat. Catal.* **2018**, 1, 127-134.

55. Jaeman Han, Hyung Jun Kim, Sangwoon Yoon, Hyunjoo Lee. *J. Mol. Catal. A: Chem.* **2011**, 335, 82-88.

Appendix

Table S2.1: Available literature data on peak position of different Ru oxidation states.

Reference	XPS peak position (eV); Ru3d		
	Ru^0	Ru^{4+}	Ru^{6+}
Ma et.al. [1]	280.2	281.2	282.4
Huang et.al. [2]	280.8	281.8	282.9
Wang et.al. [3]	280.1	281.4	282.9
Kim et.al. [4]	280	280.7	283.3
Liu et.al. [5]	280.2	281.5	282.7
Average of above literature (S.D.)	280.3 (±0.31)	281.3 (±0.41)	282.8 (±0.33)
Present Work (S.D.)	280.2 (±0.30)	281.6 (±0.30)	284.3 (±0.20)

Table S2.2: Available literature data on peak position of different Ce oxidation states.

Reference	XPS peak position (eV); Ce3d									
	Ce^{3+} contribution				Ce^{4+} contribution					
	I	II	III	IV	I	II	III	IV	V	VI
Du et.al. [6]	880.6	884.4	899.3	903.9	882.2	888.6	898	900.7	907.2	916.2
Peng et.al. [7]	880.6	883.9	898.6	901.9	881.9	888.5	897.6	900.3	906.9	916.1
Schierbaum [8]	880.1	884.8	898.8	901	882.3	888.8	898.2	903.5	907.4	916.7
Huang et.al. [2]	880.2	884.6	898.7	902.6	882.4	888.7	897.6	900.1	907.7	916.6
Ni et. al. [9]	NA	883.5	NA	903	881.6	888.5	897.4	900.1	907.4	916.7
Hu et.al. [10]	881.7	885.7	899.1	903	882.9	889	897.6	901.2	907.7	916.8
Average of above literature (S.D.)	880.8 (±0.63)	884.5 (±0.76)	898.9 (±0.29)	903 (±0.70)	882.2 (±0.44)	888.7 (±0.19)	897.7 (±0.30)	900.6 (±0.47)	907.4 (±0.30)	916.5 (±0.29)
Present Work (S.D.)	880.9 (NA)	883.6 (±0.30)	898.5 (±0.50)	901.8 (±0.68)	881.8 (±0.30)	888 (±0.12)	897.8 (±0.50)	900 (±0.12)	907.2 (±0.40)	916.4 (±0.40)

References

1. Zhanwei Ma, Shengli Zhao, Xiaoping Pei, Xumao Xionga, Bin Hu. Catal. *Sci. Technol.* **2017**, 7, 191-199.

2. Hao Huang, Qiguang Dai, Xingyi Wang. *Appl. Catal. B* **2014**, 158–159, 96-105.

3. Ruyue Wang, Yong Wang, Mengqi Ren, Guoxin Sun, Daowei Gao, Yap Ray Chin Chong, Xu Li, Guozhu Chen. *Int. J. Hydrogen Energy* **2017**, 42, 6757-6764.

4. Kwangsup Kim, Nicholas Winograd. *J. Catal.* **1974**, 35, 66-72.

5. Xiaolong Liu, Junlin Zeng, Jian Wang, Wenbo Shiad, Tingyu Zhu. *Catal. Sci. Technol.* **2016**, 6, 4337-4344.

6. Xianjun Du, Dengsong Zhang, Liyi Shi, Ruihua Gao, Jianping Zhang. *J. Phys. Chem. C* **2012**, 116, 10009-10016.

7. Ruosi Peng, Shujun Li, Xibo Sun, Quanming Ren, Limin Chen, Mingli Fu, Junliang Wu, Daiqi Ye. *Appl. Catal. B* **2018**, 220, 462-470.

8. Klaus-Dieter Schierbaum. *Surf. Sci.* **1998**, 399, 29-38.

9. Jinbo Ni, Juan Gao, Hui Wei, Xianya Geng. *J. Mater. Sci. Mater. Electron.* **2017**, 28, 11029-11033.

10. Zong Hu, Xiaofei Liu, Dongmei Meng, Yun Guo, Yanglong Guo, Guanzhong Lu. *ACS Catal.* **2016**, 6, 2265-2279.

Chapter 3

CO_2 methanation on Ru/CeO_2 rods:

Effect of Ru particle size

A paper based on this chapter is in preparation.

Abstract

In this study, Ru/CeO_2 catalysts were prepared with different Ru particle size between 1.7 and 7.4nm. A catalyst with 4.8nm particle size shows the maximum reaction rate of 0.0045 $mol.h^{-1}.m^{-2}_{Ru}$ at 215°C, while exclusively CH_4 is formed. This suggests that the step sites on the Ru surface are involved in the rate-determining step. Based on the literature, the structure-sensitivity in Ru catalysts is assigned primarily to the variation in Ru particle size. However, correlation of activity with the extent of Ru^{4+} dissolution in CeO_2 indicates the possible effect of support via CO_2 activation on oxygen vacancies present in CeO_2. Raman and H_2-TPR results show that Ru^{4+} dissolution increases with RuO_2 loading, while it decreases with increasing reduction temperature. A catalyst with maximum Ru^{4+} dissolution exhibits the highest activity for CO_2 methanation, indicating that the presence of Ru facilitates CO_2 activation via formate formation on oxygen vacancy. Therefore, it is concluded that the two reaction steps, on the Ru surface and on the CeO_2 support, are rate-determining.

3.1. Introduction

The share of electricity from renewables (wind and solar) has increased significantly in the last decade. The total wind capacity across the world is increased from 17 GW in 2000 to 318 GW in 2013 (1). However, these sources of electricity generation are intermittent and require efficient storage of surplus energy. The Power-to-Gas (PtG) technology can convert this surplus electricity into CH_4 gas in two steps. The first step includes the production of H_2 via water dissociation using electrolysis (2) or plasmas (3). In the second step, H_2 is converted to CH_4 (methanation reaction) using external CO or CO_2 source. The resulting CH_4 can be easily injected into the existing gas distribution grid or gas storages. With the advancements in CO_2 capture technologies, catalytic hydrogenation of CO_2 into fuels such as methane (4, 5, 6) is considered to be attractive for CO_2 fixation.

Catalytic CO_2 methanation reaction is exothermic in nature. Generally, catalysts such as Ru, Ni, Pd supported on reducible supports (CeO_2, ZrO_2) exhibit high activity and selectivity towards CH_4 between 300-400^oC (7). Tada et al. (8) reported that the Ni catalysts perform better on reducible supports (CeO_2, TiO_2) compared to non-reducible supports (Al_2O_3, MgO). High activity of reducible supports results from their abundant oxygen vacancies and easy redox cycles (9). Addition of CeO_2 to Ru/ Al_2O_3 catalysts is also reported to promote the activity for CO_2 methanation (10).

In supported metal catalysts, under oxidizing conditions, active metal can dissolve partially in oxide support. The dissolution of Ru into CeO_2 lattice is reported to increase the performance of CeO_2 supported catalysts (11, 12). The effect of dissolution of different metals (Ni, Co, Pd, or Ru) on the CO_2 methanation activity of CeO_2 is studied by Sharma et. al. (12). They reported (12) the best performance for $Ce_{0.95}Ru_{0.05}O_2$ catalysts at 450^oC (55% conversion and 99% selectivity for methane). Upham et. al. (11) reported that the incorporation of Ru affects the degree of surface reduction of CeO_2 and intermediate surface reduction, i.e. not too oxidized or too reduced, resulted in highest activity (11).

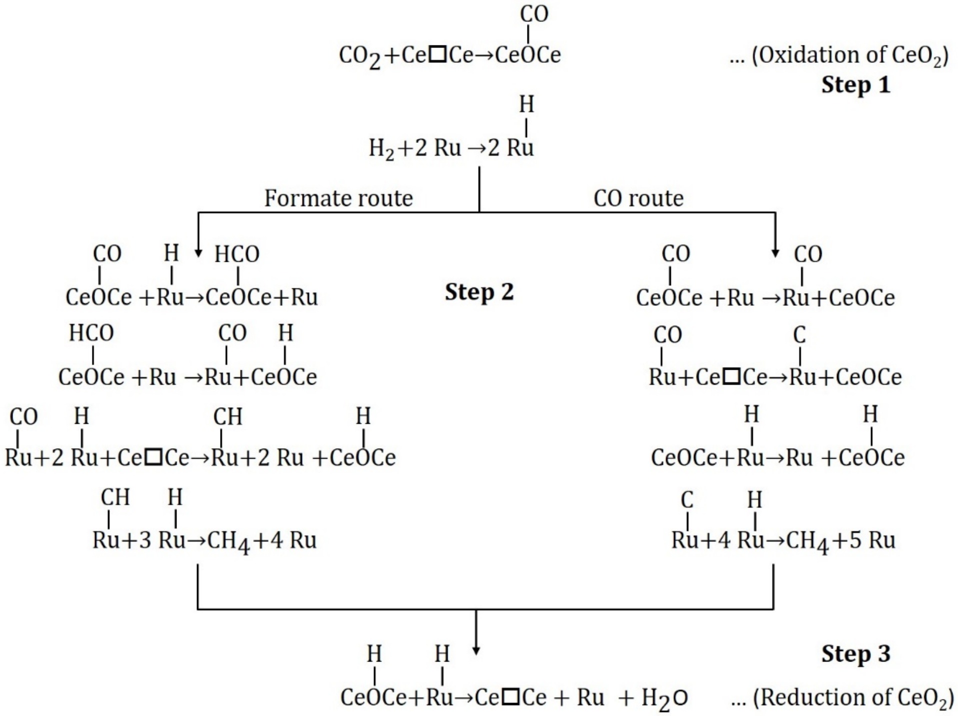

Scheme 3.1: Two possible mechanisms of CO_2 methanation on Ru/CeO_2 catalyst. (Ru is an active metal site, □ is oxygen vacancy). Adapted from our previous publication (16).

The reaction pathway and intermediate species formed during CO_2 methanation is quite debated topic in literature. On metal catalysts supported on non-reducible support, both CO_2 and H_2 dissociate on metal surface to form either formate (13) or CO intermediate (14). Whereas, on metal catalysts supported on reducible support, CO_2 can activate on metal as well as support while H_2 dissociates on active metal. Wang et. al. (14) reports that mechanism of CO_2 methanation follows the CO route on Ru/CeO_2 catalysts, while Solis-Garcia et al. (15) reported that formate is the favorable route on Ni/ZrO_2 catalysts. Both pathways on Ru/CeO_2 catalyst are presented in scheme 3.1, assuming CO_2 activation on the support material exclusively. Both pathways include three common steps, i.e. 1. adsorption of CO_2 on oxygen vacancy of CeO_2, 2.

formation of intermediate on a metal surface, and 3. re-generation of oxygen vacancy via H-spillover.

CeO_2 is generally known for abundant oxygen vacancies and high redox capacity without changing the crystal structure. The effect of the crystal shape of CeO_2 support on the performance of Ru/CeO_2 catalysts has been studied for CO_2 methanation (16, 17). Wang et. al. (17) reported that activity decreases in the order cubes > octahedra > rods. Unfortunately, the particle size of Ru varied on the different nano-shapes. In our recent publication (16), we studied the effect of CeO_2 morphology using Ru/CeO_2 catalysts with constant metal particle size. We reported an opposite trend in activity (rods > octahedra > cubes) compared to Wang, suggesting a significant influence of metal particle size on activity.

Therefore, in this work, we studied the effect of Ru particle size on the performance for CO_2 methanation. The particle size of Ru on CeO_2 nano-rods was varied via the RuO_2 loading and reduction temperature. The catalysts are characterized using H_2 and CO chemisorption, X-ray diffraction, electron microscopy, Raman spectroscopy, and hydrogen temperature programmed reduction (H_2-TPR). The results show that the activity per surface area of Ru indeed depends on Ru particle size. The influence of Ru dissolution in CeO_2 on catalytic activity is also discussed.

3.2. Experimental

3.2.1. Materials

$Ru(acac)_3$ (97%) and $Ce(NO_3)_3.H_2O$ (99%) were purchased from Sigma-Aldrich, while NaOH (99%) was purchased from Merck Millipore. All the materials were used as received. Deionized water (Synergy® systems) was used in all the experimental processes. All the gases, i.e. Hydrogen, nitrogen, and carbon dioxide, used during activity measurements was purchased from Linde with the purity of 99.999%.

3.2.2. Preparation of CeO_2 rods

CeO_2 nano-rods are synthesized using a hydrothermal procedure reported previously (18). Solutions of $Ce(NO_3)_3.H_2O$ (2.17 g in 5 ml water) and NaOH (24 g in 35 ml water) were prepared separately. Both solutions were added and stirred for 30 min under ambient conditions. The resulting reaction mixture was then transferred to a 125 ml Teflon bottle and filled 80% with water. Teflon bottle was sealed tightly in an autoclave and heated at 180^oC for 24h. The precipitate obtained was centrifuged and washed several times using water, to remove NaOH completely. The samples were finally dried (100^oC for 4h) before the calcination at 500^oC (5^oC/min) for 5h in the air (100 ml/min). The sample was stored in ambient.

3.2.3. Preparation of Ru/CeO_2 rods

Wet-impregnation method was used to synthesize Ru/CeO_2 catalysts with different particle size. In a typical synthesis, 3g of CeO_2 was dried overnight at 100^oC and added to 40 ml water under stirring. Varying amount (0.47, 0.83 and 1.18g) of $Ru(acac)_3$ was then added to the above mixture and stirred for 3h at ambient. The precipitate obtained was centrifuged and dried at 100^oC. All the samples were calcined at 500^oC (5^oC/min) for 5h in the air (100 ml/min) and stored under ambient conditions.

3.2.4. Characterization of samples

X-ray diffraction (XRD) patterns were recorded using a Bruker D2 powder diffractometer equipped with a position-sensitive detector over a 2θ range between 10^o and 90^o using Cu Kα radiation, λ= 0.1544nm. Surface area was determined by N_2-adsorption at -196^oC using the BET isotherm (Micromeritics Tristar). The samples were out-gassed in vacuum at 300^oC for 24 h prior to analysis. TEM images were obtained on a Philips CM300ST-FEG electron microscope operated at an acceleration voltage of 300kV. Samples for TEM measurements were ultrasonically dispersed in ethanol, and droplets of the suspension were deposited on a copper grid coated with carbon. The Ru loading on the supports was determined by X-ray fluorescence (XRF, Bruker S8 tiger). Raman spectroscopy measurements were performed using a Bruker Senterra Raman spectrometer, equipped with a cooled charge-coupled-device (CCD) detector. Spectra were recorded using a 532nm laser under ambient conditions and normalized based on the intensity of the main peak at 460cm^{-1}. The power of the incident beam was 2mW with an exposure time of 1 second.

H_2-TPD and H_2-TPR were performed using in-house plug-flow reactor with in-line TCD. For H_2-TPR, about 20mg of the sample was placed in a quartz tube and heated to 150°C in Ar. The sample was kept at that temperature for 1h to remove moisture and adsorbed gases. After cooling down to ambient, the temperature was again increased to 650°C at 5°C/min in 5%H_2/Ar. H_2 uptake was monitored continuously using a TCD, which was calibrated using NiO as the standard. For H_2-TPD, the catalyst was reduced at the desired temperature (Table 3.1) in 5%H_2/Ar for 1 hour followed by flushing in Ar at the same temperature for 30 minutes. The sample was then cooled down and H_2 was adsorbed at 30°C for 30 minutes before the gas was changed to Ar to remove physically adsorbed H_2. Finally, the sample was heated to 500°C (heating rate: 20°C/min) in Ar and desorption of H_2 was monitored. Averaged particle size, dispersion and surface area of Ru was calculated using procedure reported elsewhere (16). It has been confirmed (16, Chapter 4) that the results are not influenced by H-spillover and strong metal support interaction (SMSI).

CO chemisorption was performed on Chemisorb 2750 (Micromeritic) to determine the particle size and surface area of Ru metal. The U-shaped tube was packed with about 50mg sample and reduced at the desired temperature (Table 3.1) in pure H_2. The sample was then flushed with He at the same temperature for 30 minutes and cooled down to 25°C. Pulses of CO with known concentration was then introduced into the reactor and uptake of CO was monitored using online TCD.

3.2.5. Catalytic performance

All the catalytic tests were carried out in quartz tubular reactor (I.D.= 4mm) at atmospheric pressure. In a typical experiment, 50mg of the catalyst with particle size 125-250µm was homogeneously mixed with 250mg of glass beads with similar particle size to prevent hotspot formation. The catalyst was reduced at 250°C (5°C/min heating rate) for 2h in a gas mixture of N_2 (75%, v/v) and H_2 (25%, v/v) at 100ml/min of total flow. The system was cooled down to 200°C in N_2 and the gas mixture [CO_2 (10%, v/v), H_2 (40%, v/v) and N_2 (50%, v/v)] was introduced into the reactor with a total flow rate of 60ml/min, resulting in a weight-based space velocity of 72 l g^{-1} h^{-1}. Product gases were analyzed using an on-line Varian CP-3800 Gas Chromatography equipped with an Agilent CP-Molsieve 5A and PoraPLOT Q column and a TCD. In a typical experiment, the temperature of operation was increased from 200°C to 350°C. The system was allowed to reach steady state before measuring the CO_2 conversion. It was ensured that no deactivation occurred, by repeating the measurement at 300°C at the end of each experiment and also by monitoring activity of best performing catalyst for at 200°C for 8 hours (Figure S3.2). Carbon balance for every experiment was better than 97%. Reaction rates (r) were calculated under the differential condition and defined as moles of CO_2 converted per surface area of Ru per second as calculated by the following equation:

$$r=\frac{CO_{2_{in}}\times x_{CO_2}}{SA_{Ru}\times W_{cat.}}$$

Where, $CO_{2_{in}}$ is the molar flow of CO_2 at the inlet (mol/s), $x_{CO_2}$is a fraction of CO_2 converted, SA_{Ru} is an active surface area of Ru per gram catalyst (m^2/g) and $W_{cat.}$ is the weight of catalyst (g). It should be noted that internal mass transfer limitations can be ruled out at differential conditions at a temperature up to 250°C, based on the Weisz-Prater criterion (calculation shown in supporting information).

3.3. Results and discussion

3.3.1. Physical properties and X-ray diffraction

Table 3.1 presents the metal surface areas of all fresh catalyst based on both H_2-TPD as well as CO chemisorption experiments. The values are in reasonable agreement and it is important to note that the order in the metal surface areas of the six samples is identical according to both techniques. The averaged metal particles sizes are also presented, calculated by assuming hemispherical particles. As would be expected, the metal dispersion decreases with increasing metal loading, as well as with increasing reduction temperature.

Table 3.1: Metal loading and particle size calculated for different catalysts.

Catalysts	Ru loading (%)[a]	$T_{red.}$ (°C)	Ru surface area (fresh catalysts), m^2/g		Ru particle size (fresh catalysts), nm		Ru particle size (spent catalysts), nm[c]
			CO-chem.[b]	H_2-chem.[c]	CO-chem.[b]	H_2-chem.[c]	
Ru/CeO_2	3.0	200	7.6	8.5	2.1	1.7	1.9
Ru/CeO_2	5.3	200	7.2	8.1	4.5	3.2	3.3
Ru/CeO_2	8.0	200	6.9	7.7	5.5	4.8	5.0
Ru/CeO_2	8.0	300	6.5	7.3	6.1	5.3	5.4
Ru/CeO_2	8.0	400	6.0	6.1	6.5	6.3	6.1
Ru/CeO_2	8.0	500	5.6	5.2	6.9	7.4	7.2

a= measured using X-ray fluorescence, b= determined using CO chemisorption, c= determined using H_2-TPD.

Table 3.2: Physical properties of Ru/CeO_2 catalysts.

Catalysts	S_{BET} (m^2/g)[a]	CeO_2 crystalline size (nm)[b]	Lattice parameter (nm)[c]
CeO_2	63	12.9	0.5440
3%Ru/CeO_2	67	13.1	0.5422
5.3%Ru/CeO_2	59	13.5	0.5413
8%Ru/CeO_2	62	13.4	0.5402

a= surface area determined using N_2-physisorption, b= calculated using Scherrer's equation, c= calculated using equation $LP=\sqrt{d^2\times(h^2+k^2+l^2)}$ where d is lattice spacing, calculated using Bragg's equation for most dominant (111) peak and (h, k, l) are Miller indices.

Figure 3.1 shows the XRD patterns of bare CeO_2 and RuO_2/CeO_2 catalysts, confirming the fluorite structure of CeO_2 with *Fm-3m* space group (JCPDS 34-0394). Peaks observed at around 34 and 54° can be assigned to the presence of RuO_2 (16). The crystallite size, calculated using Scherrer's equation for most dominant {111} peak, and surface area of CeO_2 support did not change after the addition of RuO_2 (Table 3.2). However, the lattice parameter (Table 3.2) of CeO_2 calculated using the peak position of the {111} plane decreases with RuO_2 loading. It is reported that the change in lattice parameter is generally caused by the incorporation of active metal, Ru in this case, into CeO_2 lattice (19). This is in line with the fact that the ionic radius of Ru^{4+} (0.062nm) is smaller than that of Ce^{4+} (0.101nm) (20), causing contraction of the lattice upon Ru^{4+} incorporation.

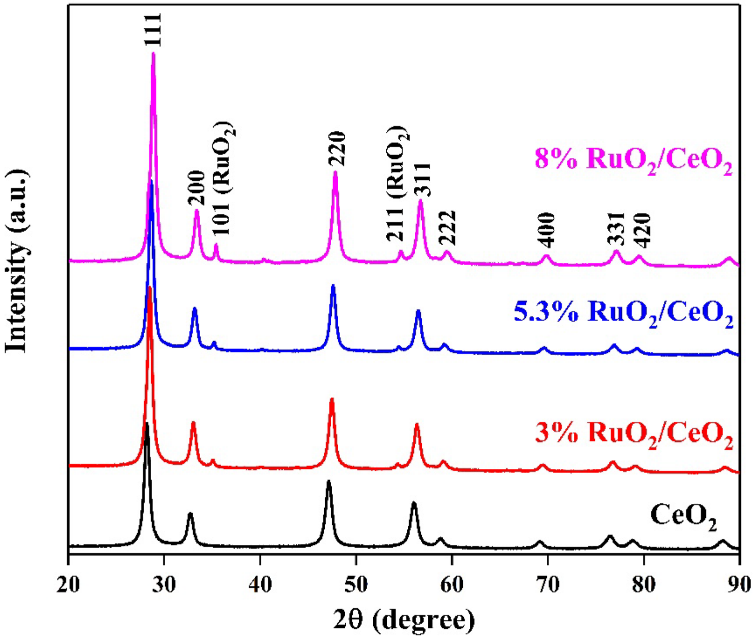

Figure 3.1: X-ray diffraction pattern of rod-shaped CeO_2 (bare) and RuO_2/CeO_2 (with increasing RuO_2 loading).

3.3.2. Scanning/Transmission electron microscopy

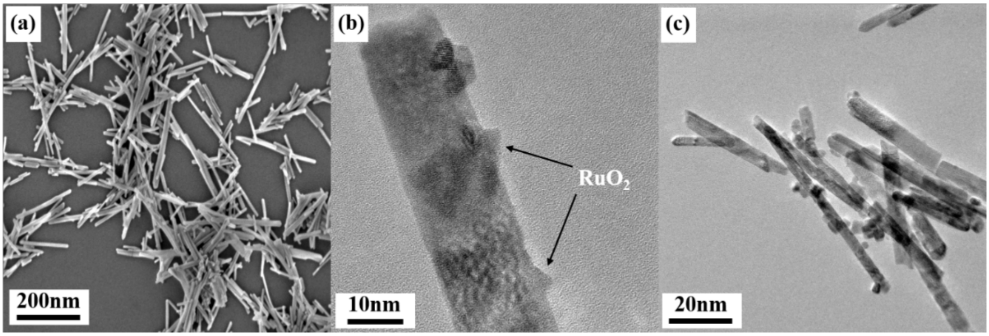

Figure 3.2: (a) SEM image of bare CeO_2, TEM images of RuO_2/CeO_2 catalyst (b) before and (c) after the experiment.

SEM image of bare CeO_2 (Figure 3.2a) after calcination at 500°C shows clear rod shapes, without any deformation due to synthesis procedure (21). The typical diameter of CeO_2 rods was 5-10nm, while the length of rods was about 200nm, resulting in an aspect ratio of 20. In the case of 8%RuO_2/CeO_2, metal nanoparticles were detected on the edge of CeO_2 surface (Figure 3.2b) with a typical particle size of 5nm, consistent with H_2-TPD and CO-chemisorption (Table 3.1). The typical particle size measured for catalysts with low RuO_2 loading (not shown) also agrees with chemisorption results. Although, the number of Ru particles measured for these catalysts was insufficient to calculate a particle size distribution. A TEM image of spent catalyst (Figure 3.2c) confirms that the morphology of CeO_2 and Ru particle size was retained after the experimental procedure.

3.3.3. Raman spectroscopy

Raman spectra of bare CeO_2 is (Figure S3.1) dominated by a strong F_{2g} peak at 460 cm^{-1} of the fluorite phase. Three additional weak peaks are seen at 230, 590 and 1150 cm^{-1}, due to second-order transverse acoustic (2TA) mode, defect-induced D mode, and second-order longitudinal optical (2LO) mode, respectively (19). Since defect-induced D mode arises from the presence of oxygen vacancies, the intensity ratio of D and F_{2g} mode (I_{590}/I_{460}) is considered as a measure for the oxygen vacancy concentration (16, 19).

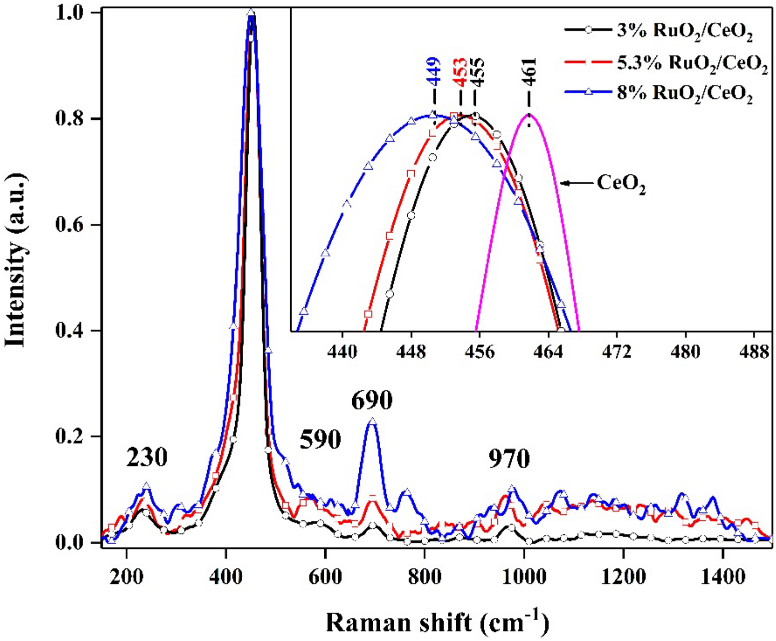

Figure 3.3: Raman spectra of calcined RuO$_2$/CeO$_2$ with increasing Ru loading. All spectra are normalized based on the intensity of the main peak at ~460 cm^{-1}.

Raman spectra of RuO$_2$/CeO$_2$ samples (Figure 3.3), after calcination at 500^{o}C in the air, shows additional peaks at 690 and 970 cm^{-1}. The new bands cannot be attributed to the presence of ruthenium with different oxidation states (800 cm^{-1} for RuO$_3$, 822–881 cm^{-1} for RuO$_4$, 808 cm^{-1} for RuO$_4^{-2}$, 380–440 and 590 cm^{-1} for hydrated RuO$_2$) (22, 23, 24). According to literature (17, 19, 22, 25), these bands at 690 and 970 cm^{-1} can be assigned to the formation of Ru-O-Ce bond. Therefore, the intensity ratio between the bands assigned to Ru-O-Ce bond and F$_{2g}$ band ($I_{690+970}/I_{460}$) represent the extent of Ru dissolution into CeO$_2$ lattice, which is increasing with RuO$_2$ loading (Table 3.3). Inset of figure 3.3 also shows a shift in the peak position of F$_{2g}$ band to lower wavenumber on additional of RuO$_2$, due to change in the distance between Ce-O bond (26, 27). This further confirms the interaction of Ru with CeO$_2$ which is also increasing with RuO$_2$ loading. Table 3.3 shows that the intensity ratio

(I_{590}/I_{460}) of CeO_2, representing oxygen vacancy concentration, remains constant when RuO_2 is added. This is in line with the fact that the oxidation states of Ru and Ce are identical (+4) and substitution of Ce with Ru will not generate any oxygen vacancies.

Raman spectra of 8%Ru/CeO_2 catalysts, reduced at different temperatures, also show peaks at 690 and 970cm^{-1} with varying intensity (Figure 3.4). Table 3.3 shows that the intensity ratio of $I_{690+970}/I_{460}$ decreases significantly with increasing reduction temperature. Since this ratio is correlated to the Ru-O-Ce interaction (17, 19, 22, 25), it is implied that Ru^{4+} species dissolved in CeO_2 lattice are reducing and probably recombining with Ru metal particles.

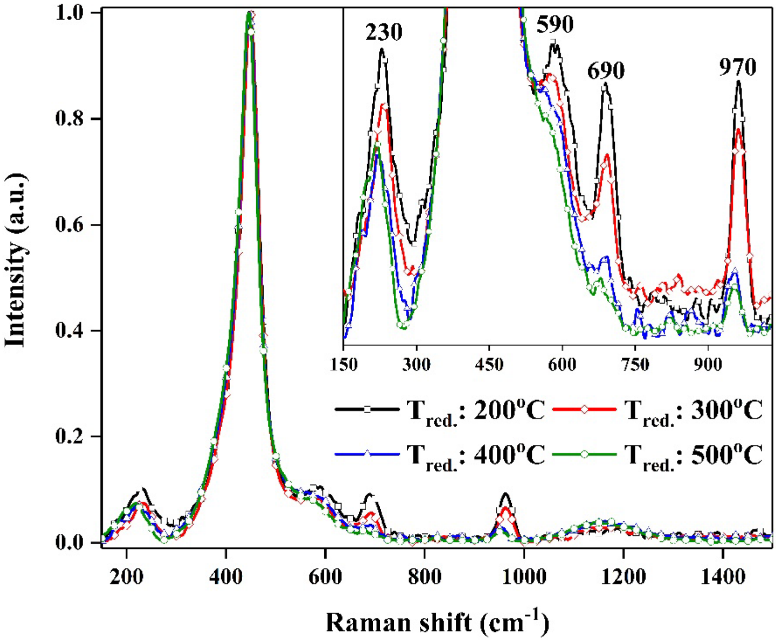

Figure 3.4: Raman spectra of 8% Ru/CeO_2 with increasing reduction temperature. All spectra are normalized based on the intensity of the main peak at ~460 cm^{-1}.

Table 3.3: Raman intensity ratios.

Catalysts	I_{590}/I_{460}	$I_{690+970}/I_{460}$
CeO_2	0.042	-
3%RuO_2/CeO_2	0.039	0.044
5.3%RuO_2/CeO_2	0.045	0.089
8%RuO_2/CeO_2	0.044	0.150
8%Ru/CeO_2-200	0.186	0.132
8%Ru/CeO_2-300	0.172	0.085
8%Ru/CeO_2-400	0.165	0.044
8%Ru/CeO_2-500	0.155	0.032

The intensity of the peak at 590cm^{-1} for reduced 8%Ru/CeO_2 catalysts increased compared to the oxidized catalysts (Figure 3.4), suggesting the formation of oxygen vacancies via H-spillover (Table 3.3) (14). Surprisingly, the ratio of I_{590}/I_{460} decreases with increasing reduction temperatures (Table 3.3), indicating generation of fewer oxygen vacancies at high reduction temperature.

3.3.4. H_2 temperature programmed reduction

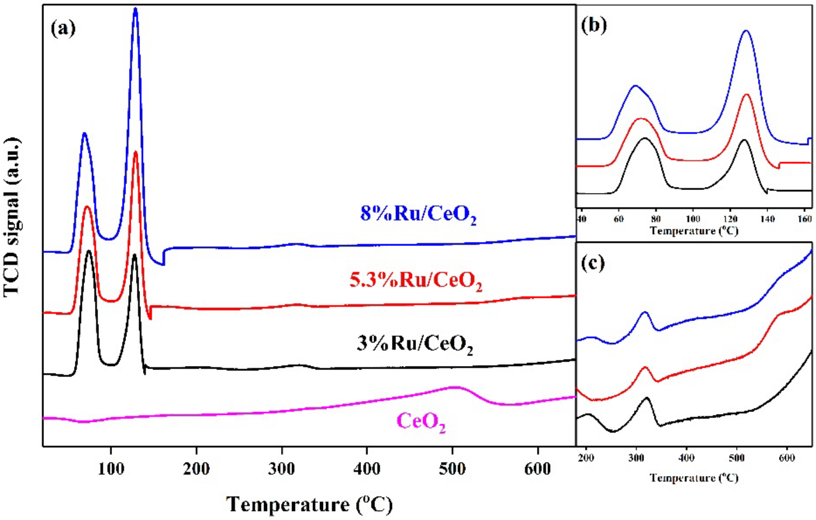

Figure 3.5: (a) H_2-TPR profile of CeO_2 and Ru/CeO_2 with different Ru loading. (b) and (c) are the magnified TPR profile between 40-160°C and 200-650°C, respectively. Wt. of catalysts: 20mg, heating rate: 5°C/min, Gas: 5% H_2/Ar (20 ml/min).

H_2-TPR measurements (Figure 3.5) was used to study the reducibility of catalyst, after the calcination at 500°C in the air. Reduction of bare CeO_2 (Figure 3.5a) occurs with maxima at 500°C with the H_2 consumption of 610 µmol/g, which is equivalent to about 1 monolayer (ML) and is consistent with our previous study (16).

H_2-TPR of RuO_2/CeO_2 samples (Figure 3.5a) shows two sharp-peaks centered at 70 and 125°C, which can be assigned to the reduction of RuO_2. It is suggested that (17), the two different peaks for RuO_2 reduction results due to the different strength of Ru interaction with CeO_2 surface. It is also observed that the first reduction peak shifts slightly to lower temperature with increasing RuO_2 loading (Figure 3.5b), suggesting facile reduction of larger RuO_2 particles. The total consumption of H_2 (Table 3.4) during the reduction of RuO_2 is calculated by integrating the peaks at 70 and 125°C. It is observed that (Table 3.4) the total H_2 consumption during reduction always strongly exceeds the H_2 consumption associated with the complete reduction of RuO_2, indicating a simultaneous reduction of CeO_2 via H-spillover and generating oxygen vacancies. This also explains the disappearance of the peak at 500°C, as observed on bare CeO_2 (Figure 3.5a). The H_2 consumption during the reduction of CeO_2 increases slightly with RuO_2 loading (Table 3.4), suggesting that the formation of oxygen vacancies is facilitated by Ru. Typically, an amount equivalent to 4ML of oxygen was removed during the reduction of CeO_2.

Table 3.4: H_2 consumption for bare and RuO_2 loaded CeO_2 during TPR.

Catalysts	H_2 consumption (µmol/g) to reduce,		
	RuO_2[a]	RuO_2/CeO_2[b]	CeO_2[c]
CeO_2	-	-	610
3%Ru/CeO_2	445	2191	1746
5.3%Ru/CeO_2	801	2581	1780
8%Ru/CeO_2	1200	3021	1821

a= Calculated assuming complete reduction $RuO_2 + 2H_2 = Ru + 2H_2O$, b= measured by integrating all peaks in TPR, c= H_2 consumption associated with the reduction of CeO_2 via H-spillover.

One small additional peak around 300°C was also observed for all three catalysts. We speculate that dissolved Ru^{4+} is segregating from the CeO_2 lattice via reduction at high temperature. The segregated Ru is likely to combine with the Ru metal particles on the surface, although we cannot rule out the formation of a single atom Ru site. The small peak at 300°C might result from the reduction of these Ru species.

3.3.5. Catalysts performance

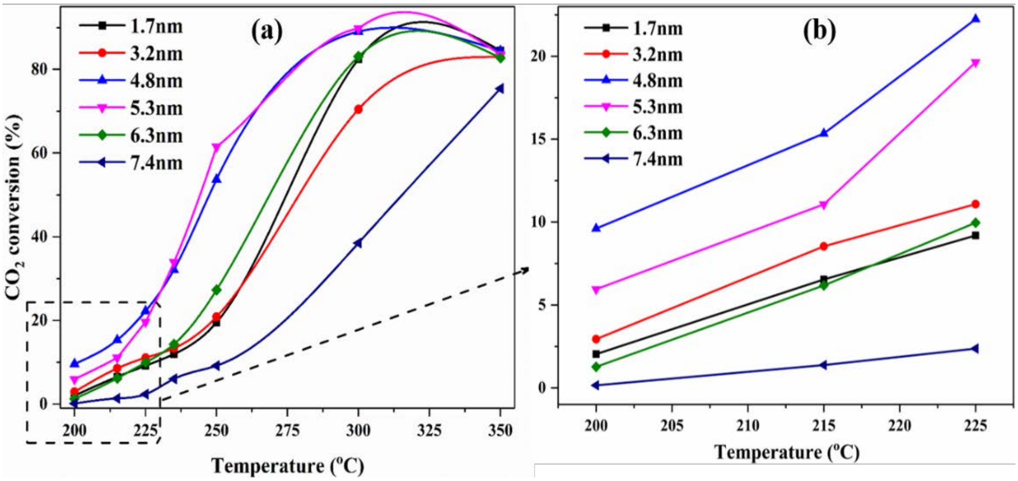

Figure 3.6: (a) CO_2 conversion on Ru/CeO_2 catalysts with increasing Ru particle size. (b) magnified image showing CO_2 conversion between 200-225°C. (weight of catalyst: 50mg, CO_2:10%, H_2: 40% GHSV:72000h^{-1})

Figure 3.6 presents the influence of temperature (200-350°C) on the conversion of CO_2 over Ru/CeO_2 catalysts with different particle size. The reaction rates (Figure 3.7) were calculated at differential conditions (conversion < 20%) to avoid any effects of concentration gradients and water inhibition. Figure 3.7 shows that the activity, normalized on Ru surface area, varies with Ru particle size according a volcano-type curve, with the highest activity observed for 4.8nm Ru/CeO_2 catalysts. CH_4 was the only product observed for all catalysts.

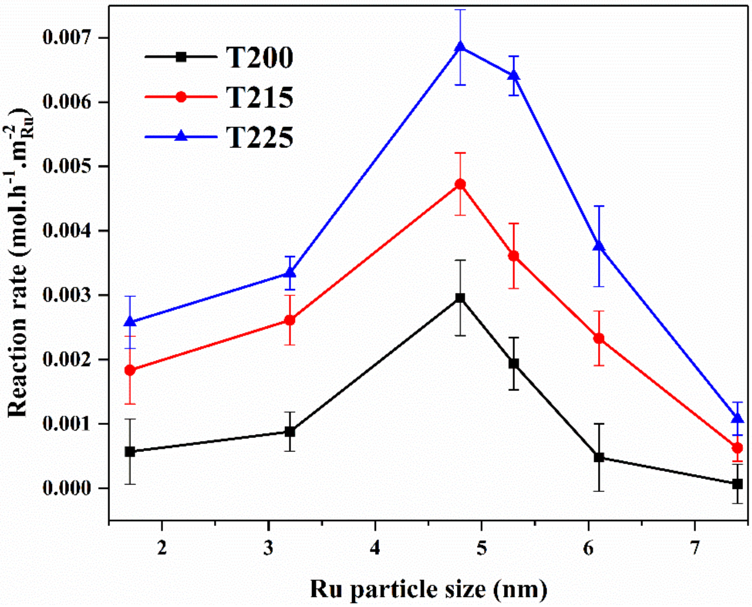

Figure 3.7: Normalized (per m^2 Ru) reaction rates of catalysts with different Ru particle size, calculated under differential conditions. (weight of catalyst: 50mg, CO_2:10%, H_2: 40% GHSV:72000h^{-1})

3.4. General discussion

In this work, we have prepared Ru/CeO_2 catalysts with different Ru particle sizes by varying Ru loading and reduction temperature. The activity of the Ru/CeO_2 is significantly influenced by the Ru particle size, resulting in a volcano-type curve (Figure 3.7).

As the effect of particles size on the performance of Ru supported on CeO_2 has not been studied before, to the best of our knowledge, we will first compare to studies on Ru supported on other reducible oxides. Panagiotopoulou et. al. (28) reported decreasing activity of Ru/TiO_2 catalysts with increasing particle size between 2.1 and 4.5nm. They suggested that flat Ru surfaces present on larger particles facilitate the cleavages of the C-O bond. Also indirect evidence for increasing activity for CO_2 hydrogenation with metal particles size on Ru/TiO_2 between 1.0 and 2.0 nm is observed in a study on competitive hydrogenation of CO and CO_2 (29); increasing activity with metal particle size up to 4.5nm is consistent with the present study. On the other hand, Xu et. al. (30) reports a volcano-type curve for activity of Ru/TiO_2 catalysts, reporting maximum rate per unit Ru surface area at 2.7nm. It should be noted that strong metal-support interaction (SMSI) influences the performance of these TiO_2 supported catalysts (29, 30).

Ru supported on non-reducible oxides has been studied as well. Panagiotopoulou et. al. (28) reported increasing activity per unit Ru surface area for CO_2 methanation on Ru/Al_2O_3 with increasing particle size between 1.3 and 2.2nm, while activity decreases with increasing particle size between 7.4 and 13.6nm. Increasing activity with increasing Ru particle size between 1.0 and 2.0nm is also reported for Ru/$MgAl_2O_4$ (31), ascribed to the electronic structure of Ru nanoparticles. The results reported in both studies agree well with the present study. Furthermore, Truszkiewicz et. al. (32) also reported a volcano-type curve for CO methanation on Ru/C catalysis with Ru particle size between 2.5 and 6.0nm, with maximal activity obtained for 4.5nm Ru particles. Kwak et. al. (33) reported that highly dispersed (mostly atomic) Ru on Al_2O_3 facilitates the formation of CO instead of CH_4, while with decreasing dispersion CH_4 selectivity increases. Since we detect exclusively CH_4, the presence of single atomic sites of Ru can be ruled out.

Structure-sensitivity in CO_2 methanation is also reported using other metals. Vogt et.al (34) reported for Ni/SiO_2 catalysts maximal activity per unit Ni surface area for 2.5 nm particles, which is suggested to be caused by changes in the strength of the adsorption of CO, one of the intermediate species. They concluded that the catalysts with intermediate adsorption strength of CO, not too weak or too strong, exhibits maximum activity per unit Ni surface area. In agreement with this, Chen et. al. (35) reported decreasing activity per unit Ni surface area for Ni/SiO_2 catalysts with increasing Ni particle size larger than 2.7nm.

Summarizing, there is significant support for the hypothesis that the maximal activity of the 4.8nm particles is caused by a direct particle size effect. However, we will discuss below that an effect of the support is still possible. In any case, it is remarkable that the optimal particle size is quite different as compared to Ni. We speculate that step sites are involved in the rate determining step on the Ru particles, based on the fact that relatively large particles (4.8nm) are optimal.

Addition of RuO_2 on CeO_2 results into the partial dissolution of metal in the support, which was confirmed by a decreasing lattice parameter (XRD, Table 3.2) and shift in the 460cm^{-1} peak position in Raman (Figure 3.3), consistent with literature (19, 36). The incorporation of RuO_2 depends significantly on the metal loading as well as the reduction temperature. The metal incorporation in CeO_2 in calcined samples increases in the order 3%RuO_2/CeO_2 < 5.3%RuO_2/CeO_2 < 8%RuO_2/CeO_2, according to the XRD lattice parameter of CeO_2 (Table 3.2). This agrees well the trend in intensity ratio ($I_{690+970}/I_{460}$, Table 3.3) and red-shift in the peak position of F_{2g} band (Figure 3.3) as observed with Raman spectroscopy. The reduction temperature also affects Ru-O-Ce interaction, as dissolved Ru^{4+} species segregate and reduce at high reduction temperatures. Ru dissolution probed with Raman spectroscopy ($I_{690+970}/I_{460}$, Table 3.3) decreases with increasing reduction temperature. In short, the 4.8nm Ru/CeO_2 catalyst contains the highest concentration of dissolved Ru^{4+} which is caused by the high Ru loading and the low reduction temperature of that specific sample.

Nevertheless, Gao et. al. (37) reported that dissociation of CO_2, forming formate (HCOO*) intermediate, is enhanced by dissolving Ru^{4+} in CeO_2, based on DFT calculations, This agrees well with our observation that the catalyst with highest activity shows maximum dissolution of Ru^{4+} (Figure 3.8). Therefore, it is possible that activation of CO_2 on CeO_2 is also rate-determining, in agreement with the conclusion based in the influence of the CeO_2 surface structure on the activity of Ru (16, Chapter 2). Presence of two rate-determining step, each on metal and support, is also observed for Ni/CeO_2 catalysts (Chapter 4).

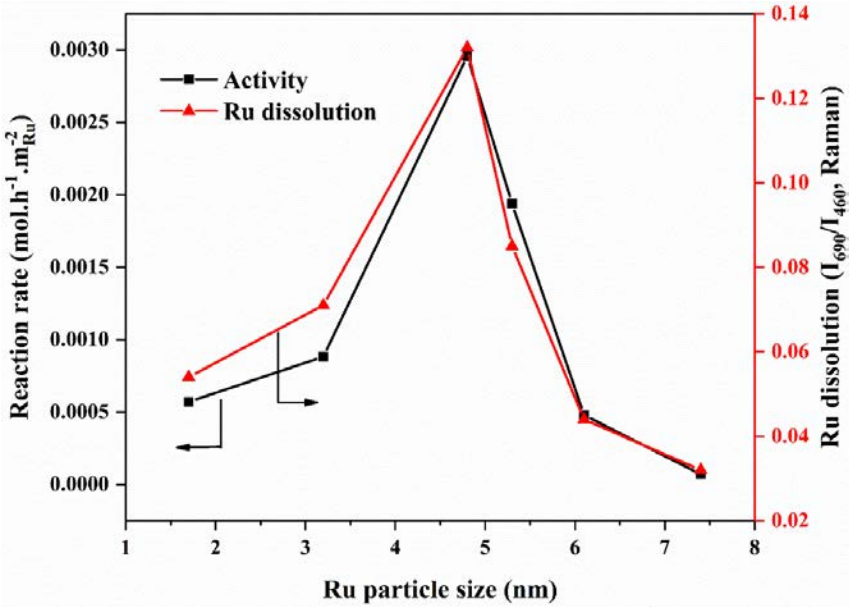

Figure 3.8: Correlation between the activity (at 200°C) and the extent of Ru dissolution of catalysts.

3.5. Conclusions

This study reports on the structure-sensitivity in CO_2 methanation of Ru/CeO_2 catalysts. The activity per Ru surface area depends significantly on the metal particle size, showing a maximum at 4.8nm. This is in good agreement with similar observations for Ru supported on TiO_2 and non-reducible oxides, indicating a direct effect of the metal particle size. The fact that 4.8nm particles are most active, suggests that step sites are involved in the rate determining step. However, the activity also correlates with the extent of Ru^{4+} dissolution in CeO_2, increasing the rate of CO_2 activation on CeO_2, forming formate on an oxygen vacancy. This agrees well with the conclusion in Chapter 2 based on the influence of the surface structure of CeO_2, that reaction of CO_2 with oxygen vacancies is rate determining. Therefore, it is concluded that two reaction steps influence the overall rate of reaction, on the Ru surface and on the CeO_2 support respectively.

References

1. GWEC – Global Wind 2013 Report.

2. K. Ghaib, F.Z. Ben-Fares. *Renewable and Sustainable Energy Rev.* **2018**, 81, 433.

3. X. Chen, S.L. Suib, Y. Hayashi, H. Matsumoto. *J. Catal.* **2001**, 201, 198.

4. Gordon D. Weatherbee, Calvin H. Bartholomew. *J. Catal.* **1981**, 68, 67-76.

5. Michiaki Yamasaki, Hiroki Habazaki, Katsuhiko Asami, Kohichi Izumiya, Koji Hashimoto. *Catal. Commun.* **2006**, 7, 24-28.

6. Fabien Ocampo, Benoit Louis, Anne-Cécile Roger. *Appl. Catal. A*, **2009**, 369, 90-96.

7. Fei Wang, Min Wei, David G. Evans and Xue Duan. *J. Mater. Chem. A* **2016**, 4, 5773-5783.

8. Shohei Tada, Teruyuki Shimizu, Hiromichi Kameyama, Takahide Haneda, Ryuji Kikuchi. *Int. J. Hydrogen Energy* **2012**, 37, 5527-5531.

9. Antonio Ruiz Puigdollers, Philomena Schlexer, Sergio Tosoni, Gianfranco Pacchioni. *ACS Catal.* **2017**, 7, 6493-6513.

10. Shohei Tada, Ochieng James Ochieng, Ryuji Kikuchi, Takahide Haneda, Hiromichi Kameyama. *Int. J. Hydrogen Energy* **2014**, 39, 10090-10100.

11. D. Chester Upham, Alan R. Derk, Sudanshu Sharma, Horia Metiu and Eric W. McFarland. *Catal. Sci. Technol.* **2015**, 5, 1783-1791.

12. Sudhanshu Sharma, Zhenpeng Hu, Peng Zhang, Eric W. McFarland, Horia Metiu. *J. Catal.* **2011**, 278, 297-309.

13. Gabriella Garbarino, Daria Bellotti, Elisabetta Finocchio, Loredana Magistri, Guido Busca. *Catal. Today* **2016**, 277, 21-28

14. Wang, S. He, H. Chen, B. Wang, L. Zheng, M. Wei, D.G. Evans, X. Duan. J. Am. Chem. Soc. 2016, 138, 6298-6305.

15. A. Solis-Garcia, J.F. Louvier-Hernandez, A. Almendarez-Camarillo, J.C. Fierro-Gonzalez. *Appl. Catal. B* **2017**, 218, 611-620.

16. Tushar Sakpal, Leon Lefferts. *J. Catal.* **2018**, 367, 171-180.

17. Wang, F.; Li, C.; Zhang, X.; Wei, M.; Evans, D. G.; Duan, X. *J. Catal.* **2015**, 329, 177–186.

18. Hao-Xin Mai, Ling-Dong Sun, Ya-Wen Zhang, Rui Si, Wei Feng, Hong-Peng Zhang, Hai-Chao Liu, Chun-Hua Yan. *J. Phys. Chem. B* **2005**, 109, 24380–24385.

19. Hao Huang, Qiguang Dai, Xingyi Wang. *Appl. Catal. B* **2014**, 158–159, 96-105.

20. Shannon, R. D. *Acta Cryst.* **1976**, 32, 751–767.

21. Zili Wu, Meijun Li, Jane Howe, Harry M. Meyer III, and Steven H. Overbury. *Langmuir* **2010**, 26, 16595-16606.

22. Atsushi Satsuma, Masatoshi Yanagihara, Junya Ohyama, Kenichi Shimizu. *Catal. Today* **2013**, 201, 62-67.

23. Hyun Chol Jo, Kyung Moon Kim, Hyeonsik Cheong, Se-Hee Lee, and Satyen K. Deb. *Electrochem. Solid-State Lett.* **2005**, 8, E39-E41.

24. N. Weinstock, H. Schulze, and A. Müller. *J. Chem. Phys.* **1973**, 59, 5063.

25. Zhanwei Ma, Shengli Zhao, Xiaoping Pei, Xumao Xiong, Bin Hu. *Catal. Sci. Technol.* **2017**, 7, 191-199.

26. Bingyu Lin, Yi Liu, Lan Heng, Xiuyun Wang, Jun Ni, Jianxin Lin, and Lilong Jiang. *Ind. Eng. Chem. Res.* **2018**, 57, 9127-9135.

27. Ning Wang, Weizhong Qian, Wei Chu and Fei Wei. *Catal. Sci. Technol.* **2016**, 6, 3594-3605.

28. Paraskevi Panagiotopoulou, Dimitris I. Kondarides, Xenophon. E. Verykios. *Appl. Catal. B* **2009**, 88, 470-478.

29. Ali M. Abdel-Mageed, Daniel Widmann, Sine E. Olesen, Chorkendorff, R. Jürgen Behm. *ACS Catal.* **2018**, 8, 6, 5399-5414.

30. Jinghua Xu, Xiong Su, Hongmin Duan, Baolin Hou, Qingquan Lin, Xiaoyan Liu, Xiaoli Pan, Guangxian Pei, Haoran Geng, Yanqiang Huang, Tao Zhang. *J. Catal.* **2016**, 333, 227-237.

31. Zbigniew Kowalczyk, Kazimierz Stołecki, Wioletta Raróg-Pilecka, Elżbieta Miśkiewicz, Ewa Wilczkowska, Zbigniew Karpiński. *Appl. Catal. A* **2008**, 342, 35-39.

32. Elżbieta Truszkiewicz, Kacper Zegadło, Damian Wojda, Bogusław Mierzwa, Leszek Kępiński. *Top. Catal.* **2017**, 60, 1299–1305.

33. Ja Hun Kwak, Libor Kovarik, and János Szanyi. *ACS Catal.* **2013**, 3, 2449-2455.

34. Charlotte Vogt, Esther Groeneveld, Gerda Kamsma, Maarten Nachtegaal, Li Lu, Christopher J. Kiely, Peter H. Berben, Florian Meirer, Bert M. Weckhuysen. *Nat. Catal.* **2018**, 1, 127–134.
35. Ching-Shiun Chen, Canggih Setya Budi, Hung-Chi Wu, Diganta Saikia, Hsien-Ming Kao. *ACS Catal.* **2017**, 7, 8367-8381.
36. Qiguang Dai, Shuxing Bai, Zhengyi Wang, Xingyi Wang, Guanzhong Lu. *Appl. Catal. B* **2012**, 126, 64-75.
37. Chen Guo, Shuxian Wei, Sainan Zhou, Tian Zhang, Zhaojie Wang, Siu-Pang Ng, Xiaoqing Lu, Chi-Man Lawrence Wu, Wenyue Guo. *ACS Appl. Mater. Interfaces* **2017**, 9, 26107-26117.

Appendix

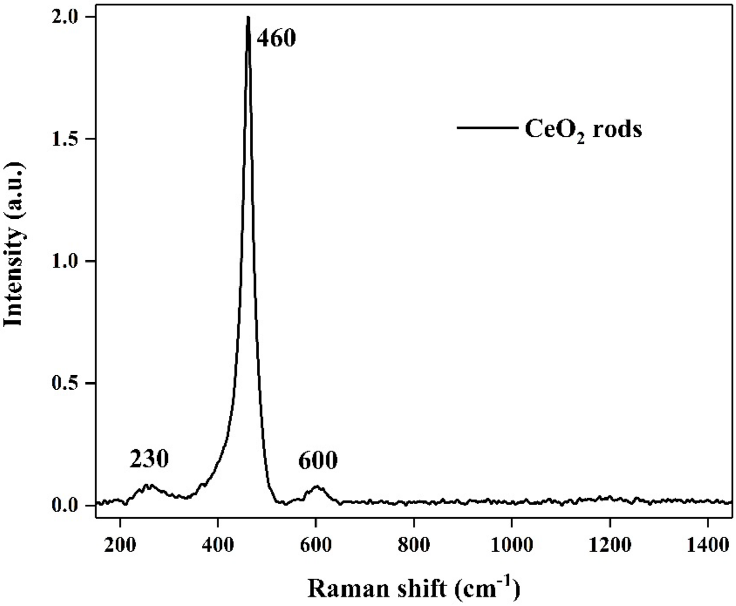

Figure S3.1: Raman spectra of bare CeO$_2$ rods.

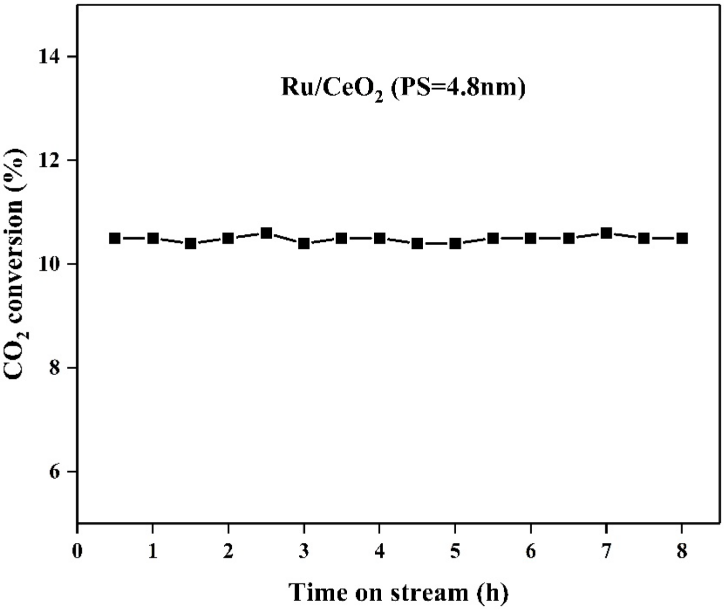

Figure S3.2: Stability study of Ru/CeO$_2$ catalysts with 4.8nm particle size over 8h time on stream. (Temperature: 200°C, weight of catalyst: 50mg, H_2:CO_2=4, GHSV=48000h^{-1})

Weisz-Prater criterion (Φ) for internal mass transfer limitation

$$\Phi=\frac{\rho_p \times r_{w,p}^{obs} \times d_p^2}{36 \times D_e \times C_s} \times [\frac{n+1}{2}]$$

Where, ρ_p is density of CeO_2 particles (kg/m^3), $r_{w,\,p}^{obs}$ is specific reaction rate (mol/kg$_{cat.}$/s), dp is catalyst particle diameter (m), De is effective diffusion coefficient (m^2/s) and Cs is concentration at external surface (mol/m^3).

ρ_p = density of CeO_2 × porosity of CeO_2
Where, Density of CeO_2 is 7.22×10^3
porosity (0.5) is calculated using pore volume of catalysts.
Therefore, $\rho_p = 3.61 \times 10^3$ kg/cm^{-3}

$De = Dm \times \frac{\varepsilon}{\tau}$
Where, Dm is diffusion coefficient (cm^3/s), ε is porosity (0.5), τ is Tortuosity (assumed to be 2).
Therefore, $De = 2.65 \times 10^{-6}$ m^2/s.

Catalyst particle size (average)= 187.5μm = 1.875×10^{-4} m.

Concentration at external surface C_s=4.5 mol/m^3

Specific rate of reaction at 215°C = 1.96×10^{-2} mol/kg$_{cat.}$/s

n = order of reaction (generally, 1)

$$\Phi = \frac{3.61 \times 10^3 \times 1.96 \times 10^{-2} \times 3.52 \times 10^{-8}}{36 \times 2.65 \times 10^{-6} \times 4.5}$$

$$\Phi = \frac{24.91 \times 10^{-1}}{429.3}$$

$$\Phi = 0.006$$

Φ < 0.15, confirming no internal mass transfer limitation.

Chapter 4

Ni/CeO$_2$ catalysts for CO$_2$ methanation: effect of CeO$_2$ morphology and Ni particle size

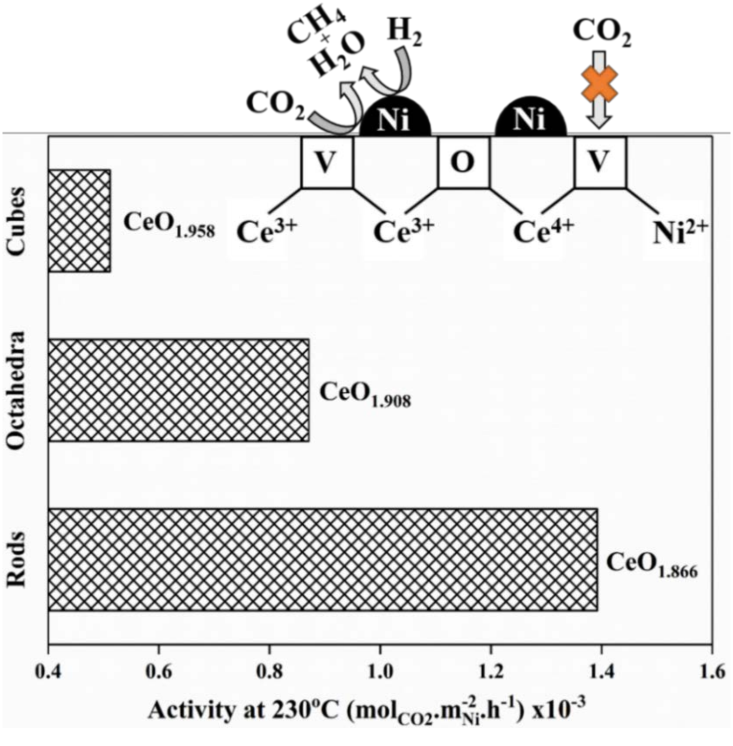

This chapter has been submitted and is currently under revision as, T. Sakpal and L. Lefferts. Ni/CeO$_2$ catalysts for CO$_2$ methanation: effect of CeO$_2$ morphology and Ni particle size. *ACS Catalysis*, **2019.**

Abstract

The performance of Ni catalysts supported on CeO_2 for CO_2 hydrogenation to methane is studied, reporting on the influence of both Ni particle size as well as the morphology of nano-shaped CeO_2 support materials. The Ni particle size, varied between 2.5 and 4.7nm, influences the performance significantly. The highest reaction rate normalized per unit surface area of Ni of was obtained with 2.9nm Ni/CeO_2 cubes at 270°C (7.54×10^{-3} mol $h^{-1} m^{-2}_{Ni}$). This is attributed to increasing CO adsorption on increasing Ni particle size and Ni particles of 2.9nm possess favorable intermediate CO adsorption strength. Too weak adsorption on smaller particles causes insufficient activation of the CO bond whereas too strong adsorption on larger particles causes CO poisoning. Regarding CeO_2 morphology, Ni/CeO_2 rods outperforms the cube and octahedra shaped catalysts with identical Ni particle sizes. Keeping the Ni particle size is necessary and this has not been considered yet in literature for hydrogenation reactions, including CO_2 hydrogenation. Two types of oxygen vacancies are formed in all catalysts; (I) vacancy formed due to Ni^{2+} incorporation, which are not redox active and irrelevant, and (II) redox active vacancies formed via to H-spillover. Characterization results confirmed that the concentration of redox active vacancies increases with NiO loading. The activity of the catalysts correlates with the reducibility of Ni/CeO_2 supported on different CeO_2 morphologies, suggesting that reactive adsorption of CO_2 on CeO_2 is a rate-determining step. However, the influence of the Ni particle size clearly shows that a hydrogenation step of a carbon-containing species on the Ni surface also influences the overall activity.

4.1. Introduction

The concentration of CO_2 in the atmosphere is increasing rapidly since the industrial revolution and already crossed the 400 ppm mark, causing an increase in the earth's temperature due to the greenhouse gas effect. Coal-fired power plants are one of the main contributors to CO_2 emissions. Therefore, renewable energy, e.g. based on wind and solar, has attracted much attention in the last decade. However, the energy obtained from these sources are intermittent, fluctuating on time scales of both day and night, as well as over seasons during the year. Therefore, efficient technology is required to store the surplus energy for use during periods with low supply (1). Power-to-Gas (P2G) technology emerged as a potential candidate, since it can use surplus energy to dissociate H_2O to H_2 via electrolysis, storing H_2 as CH_4 via CO_2 methanation (2). Plasma-driven H_2O splitting (3, 4) is a possible alternative to H_2O electrolysis. In both the cases, CO_2 methanation would enable more efficient storage of H_2, since CH_4 can be easily liquefied, stored safely and distributed using existing infrastructure (5).

CO_2 methanation has been studied extensively over the years, because of its fundamental academic interest with the potential commercial application (6). Since the reaction is exothermic ($\Delta H = -165$ kJ/mol), operation at a low temperature is preferred to maximize the conversion, also avoiding the formation of CO.[7] Catalysts like Ni, Ru, Cu, Pd and Rh on metal oxide supports, e.g. Al_2O_3, SiO_2, MgO, ZrO_2, CeO_2, TiO_2, and zeolites, have been studied for this reaction and the state-of-the-art has been discussed in recent reviews (7–9). Clearly, Ni catalysts are especially of interest due to its abundance and low price (10). Ni supported on CeO_2 showed maximum CO_2 methanation activity and selectivity, compared to other commonly-used support materials, due to its high reducibility (5, 11). The reaction mechanisms proposed for this reaction proceeds via either formate or CO as a key intermediate (12–15). However, all proposed mechanisms have three steps in common as shown in scheme 4.1; 1. adsorption of CO_2 on CeO_2, filling an oxygen vacancy, 2. formation of

CO on the metal surface, and 3. regeneration of oxygen vacancy by H_2 (16).

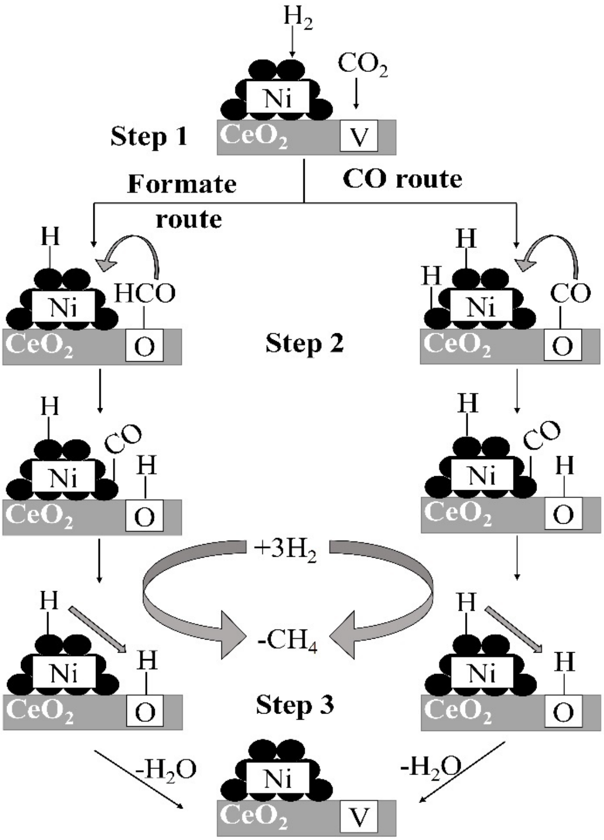

Scheme 4.1: Mechanism of CO_2 methanation via formate and CO pathways. (V is oxygen vacancy)

CO_2 methanation activity of Ni/CeO_2 is correlated to its reducibility and oxygen storage capacity, which can be affected by morphology, dispersion, and electronic properties of the active metal. The surface area of Ni, as well as CeO_2, plays a key role on the performance of Ni/CeO_2 catalysts. The activity of catalysts increases with both surface area of CeO_2 (17) as well as with Ni surface area (18,19). It is also reported (20) that CO_2 can dissociate on the surface of Ni as well as on oxygen vacancy of CeO_2 to generate CO, resulting in higher activity compared to non-reducible supports like Al_2O_3 and SiO_2.

CeO$_2$ is generally known for high redox capacity without changing the crystal structure, leading to abundant oxygen vacancies (21). CeO$_2$ crystals with different nano-shapes expose specific facets at their surfaces, inducing differences in redox properties and catalytic activity for a variety of reactions. Cubes (CeO$_2$/c) mainly expose (100) facets while rods (CeO$_2$/r) and octahedra (CeO$_2$/o) predominantly expose (111) facets (22), although discussion on the exact assignments is ongoing. The effect of shape of CeO$_2$ support on performance of supported metal catalysts has been studied for many reactions like CO oxidation (23, 24), water gas shift (22, 25), reforming reactions (26), and HCl oxidation (27). Unfortunately, many of these studies have not considered rigorously any possible effects of the metal particle size on the activity. Ideally, the metal particles on the different nano-shapes of CeO$_2$ have the same dimension to determine the effect of the support structure. Table S1.1 from chapter 1 presents an overview of work done so far to the best of our knowledge and it is noted that in most studies the metal particle size was not kept constant or sometimes not reported at all (Table S1.1). We could not find any study with constant metal particle size for hydrogenation and reforming reactions.

More specifically for CO$_2$ methanation, Bian et. al. (28) reported that for Ni/CeO$_2$, rods are more active than cubes, whereas the opposite is reported by Wang et al. (29) for Ru/CeO$_2$ catalyst, in agreement with our previous study (16). This clearly suggests that the activity is not determined by CeO$_2$ morphology exclusively. As discussed above, metal particle sizes varied in both the studies (28, 29), like in the studies of the above-mentioned reactions (23-27).

Therefore, in this work we report that the TOF of Ni on CeO$_2$ depends indeed on particle size. Thus, we studied the effect of the CeO$_2$ nano-shapes with catalyst with identical metal particle sizes, which then allows to corrolate the activity of the catalyst with the redox properties of the support.

4.2. Experimental

4.2.1. Chemicals

Nickel (II) nitrate hexahydrate (99.99%) and cerium (III) nitrate hexahydrate (99.99%) were purchased from Sigma-Aldrich, while sodium hydroxide (99%) was purchased from Merck Millipore. No further treatment was done before use. Deionized water (Synergy® systems) was used in all preparation procedure.

4.2.2. Synthesis of CeO_2 nano-shapes

Different shapes of CeO_2 were synthesized using a hydrothermal procedure reported previously (22,30). Two separate reaction mixtures were prepared by adding 2.17g of cerium nitrate and 24g of sodium hydroxide in 5 and 35ml water, respectively. Sodium hydroxide solution was then added dropwise to the cerium nitrate solution and kept stirring for another 30min. Finally, the solution was transferred to a Teflon bottle (125ml), filling it for 80%. The Teflon bottle was sealed tightly in a stainless steel autoclave and kept in an oven at the appropriate temperature for 24h (100°C for cubes or 180°C for rods). The resulting precipitate was centrifuged and washed with water several times, to remove sodium hydroxide completely. Materials were dried in an oven at 100°C for 4h and calcined at 500°C (5°C/min) for 5h in flowing air (100ml/min). CeO_2/o, with a particle size less than 50nm, was purchased from Sigma-Aldrich and calcined using the same procedure.

4.2.3. Synthesis of NiO/CeO_2 catalysts

Two series of NiO/CeO_2 catalysts were synthesized using a precipitation-deposition method. The pH and mixing time of solution was varied to achieve different Ni particle size (31). In the first series, three catalysts were prepared using different morphologies of the support (cubes, rods, and octahedra) keeping the Ni particle size constant. In the second series, five catalysts with increasing Ni particle size were prepared on cubes. In a typical synthesis, 3g of CeO_2 sample was added to 60ml of water under stirring. In another flask, 0.744g (5 wt%) nickel nitrate was dissolved in 20ml water and then slowly added to the CeO$_2$ solution under stirring. The pH of the solution was adjusted to 8 by adding 0.1M sodium hydroxide solution. The reaction mixture was stirred at room temperature for different times (55, 165 and 315 min for CeO$_2$/c, CeO$_2$/o and CeO$_2$/r respectively). For cube-shaped catalysts with different Ni particle size, almost the same procedure was employed. However, the pH of the solution was varied between 7.9 and 8.3 to obtain different Ni particle sizes. All the catalysts were centrifuged and dried at 100^{o}C for 3h, followed by calcination at 500^{o}C (5^{o}C/min) for 5h in flowing air (100ml/min).

4.2.4. Characterization of samples

BET (Micromeritics Tristar) isotherms by N$_2$ physisorption were used to determine the surface area of catalysts. Samples were out-gassed at 300^{o}C in vacuum for 24h prior to measurement. X-ray diffraction (XRD) patterns were recorded using a Bruker D2 powder diffractometer equipped with a position-sensitive detector over a 2θ range between 20^o and 90^o using Cu Kα radiation, λ= 0.1544nm. TEM images of the catalysts were obtained using a Philips CM300ST-FEG electron microscope operated at an acceleration voltage of 300kV. X-ray fluorescence (XRF, Bruker S8 tiger) was used to determine the concentration of NiO in the samples. XPS was performed using a PHI QUANTERA SXM spectrometer. Raman spectroscopy measurements were performed using a Bruker Senterra Raman spectrometer, equipped with a cooled charge-coupled-device (CCD) detector and a 532nm laser. The power of the incident beam was 2mW with an exposure time of 1 second.

Temperature-programmed measurements were performed using an in-house constructed plug-flow reactor with in-line TCD. For H$_2$-TPR, about 20mg of the sample was packed in a quartz tube and heated to 150^{o}C in Ar for 1h to remove moisture and adsorbed gases. After cooling down to ambient, the temperature was again increased to 650^{o}C at 5^{o}C/min in 5%H$_2$/Ar (20ml/min). H$_2$ uptake was monitored continuously using a TCD, which was calibrated using NiO as the standard. For H$_2$-TPD, the catalyst was reduced at 400^{o}C in 5%H_2/Ar and then cooled down in Ar. H_2 was adsorbed at 30°C for 30 min before the gas was changed to Ar to remove physically adsorbed H_2. Finally, the sample was heated to 500°C (20°C/min heating rate) in Ar and desorption of H_2 was monitored. Averaged Ni particle size, dispersion, and surface area were calculated assuming hemispherical particles; further details are reported elsewhere (16). It has been ensured that the results are not influenced by strong metal-support interaction (classical SMSI) and H-spillover, by varying the time of H_2 adsorption at 30°C.

4.2.5. Catalytic performance

Catalytic activity is measured in a quartz tubular reactor with a 4mm internal diameter at atmospheric pressure. Calibrated mass flow controllers (MFCs) were used to control the flow rates, while the temperature in the bed was controlled using a thermocouple. In a typical experiment, about 50mg of the catalyst with a particle size between 125 and 300μm was homogeneously mixed with 250mg of glass beads (105-210μm) to prevent the formation of hotspots. Prior to the test, the catalyst was reduced at 400°C (5°C/min) for 2h in a gas mixture of N_2 (75%, v/v) and H_2 (25%, v/v) at 100ml/min of total flow. The system was cooled down to 200°C in N_2 and the reaction gas mixture [CO_2 (10% v/v), H_2 (40% v/v) and N_2 (50% v/v)] was introduced into the reactor with a total flow rate of 40ml/min (WHSV= 48 l/g/h). Product gases were analyzed using an on-line Gas Chromatography (Varian CP-3800) equipped with an Agilent CP-Molsieve 5A and PoraPLOT Q column and a TCD. In a typical experiment, the temperature of operation was increased stepwise from 200 to 400°C. The system was allowed to reach steady state before measuring the CO_2 conversion. It was ensured that no deactivation occurred, by repeating the measurement at 230°C at the end of the experiment, after operating at 400°C. The reproducibility of results was confirmed by repeating the experiment using fresh catalysts. Carbon balance for each experiment was better than 95%. Reaction rates (r), expressed in mole CO_2 $h^{-1}m_{Ni}^{-2}$, were calculated under differential conditions according to the following equation,

$$r=\frac{CO_{2_{in}}\times x_{CO_2}}{SA_{Ni}\times W_{cat.}}$$

Where, $CO_{2_{in}}$ is the molar flow of CO_2 at the inlet (mol/h), $x_{CO_2}$is a fraction of CO_2 converted, SA_{Ni} is an active surface area of the Ni per gram catalyst (m^2/g-cat) and $W_{cat.}$ is the weight of catalyst (g). Internal mass transfer resistance is negligible under an operating condition, based on a calculation of the Weisz–Prater criterion.

4.3. Results and Discussion

4.3.1. Physical properties and X-ray diffraction

The constant averaged particle size of Ni (3 ±0.2nm) on three different shapes of CeO_2 was achieved by adjusting the NiO loading, proportional to the surface area of the support (Table 4.1). Consequently, the Ni surface area increases with the NiO loading. Another series of catalysts with Ni particle size between 2.5 and 4.7 nm was achieved by varying the NiO loading on CeO_2/c support while keeping the total Ni surface area constant (Table 4.1).

Table 4.1: Structure and physical properties of Ni/CeO_2.

Catalyst	S_{BET} (m^2/g)	NiO loading (%)^a	Average Ni PS (nm)^b	Ni disp. (%)^b	Ni surface area ($m^2/g_{cat.}$)^b	Lattice parameter (nm)^c
NiO/CeO_2/r	63	3.0	3.2 ±0.11	32	7.4	0.5357
NiO/CeO_2/o	40	2.4	3.1 ±0.10	33	5.6	0.5395
NiO/CeO_2/c	14	1.4	2.5 ±0.10	40	3.8	0.5411
NiO/CeO_2/c	12	1.6	2.9 ±0.12	34	3.7	0.5406
NiO/CeO_2/c	12	2.1	3.8 ±0.20	27	3.7	0.5398
NiO/CeO_2/c	14	2.4	4.2 ±0.18	24	3.7	0.5390
NiO/CeO_2/c	15	2.7	4.7 ±0.24	22	4.0	0.5383

a= measured using XRF, b= determined using H_2-TPD, c= calculated using equation $LP=\sqrt{d^2\times(h^2+k^2+l^2)}$ where d is lattice spacing, calculated using Bragg's equation and (h, k, l) are Miller indices.

Face-centered cubic fluorite structure of CeO_2 with $Fm\text{-}3m$ space group is confirmed by XRD (Figure S4.1) (JCPDS 34-0394). The averaged crystallite size, calculated using Scherrer's equation for the dominant {111} plane, increases in the order CeO_2/r > CeO_2/o > CeO_2/c, which is consistent with decreasing BET surface area in the same order (Table 4.2). Lattice parameter (Table 4.2) for the {111} plane decreases in the order CeO_2/c > CeO_2/o > CeO_2/r. Since the ionic radius of Ce^{3+} (0.115nm) is larger than Ce^{4+} (0.101nm), lattice expansion is expected upon reduction, forming Ce^{3+} and oxygen vacancies (23), suggesting that CeO_2/r contains less Ce^{3+} than the other two shapes.

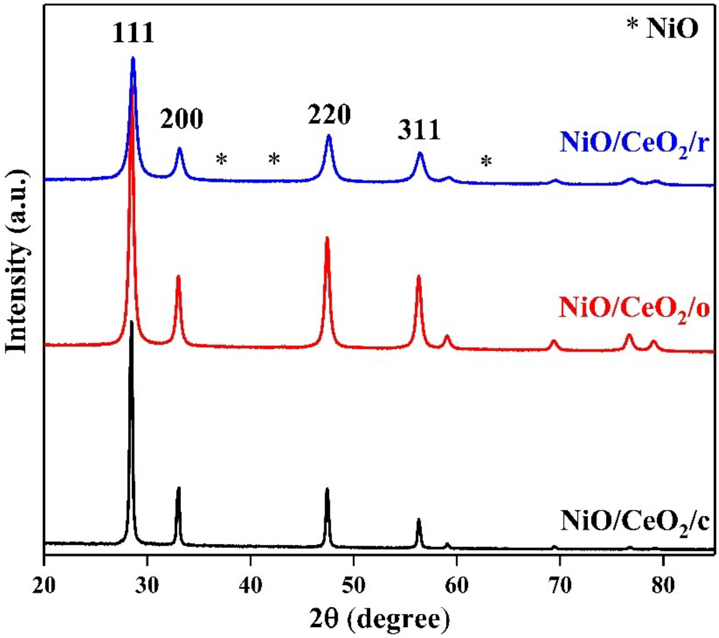

Figure 4.1: XRD patterns of NiO/CeO_2 catalysts with well-defined facets. * indicates the diffraction angles of NiO, which are below the detection limit.

NiO appears to be highly dispersed, as NiO diffraction peaks at 37, 42 and 62° are below the detection limit (Figure 4.1). Lattice parameter calculated for NiO/CeO_2 (Table 4.1) is significantly smaller than that of bare CeO_2 (Table 4.2), indicating diffusion of Ni^{2+} into the CeO_2 lattice. As the effective ionic radius of Ni^{2+} (0.083nm) is smaller than that of Ce^{4+} (0.101nm) (32), CeO_2 undergoes lattice contraction when forming $Ni_xCe_{1-x}O_{2-\delta}$ solid solution (33). The decrease in the lattice parameter is relatively large for NiO/CeO$_2$/r (0.06) compared to both NiO/CeO$_2$/o and NiO/CeO$_2$/c (0.04), leaving the order in the lattice parameter unchanged (cubes > octahedra ≥ rods). This is probably due to the higher NiO loading on rods. This agrees well with the observation that increasing the NiO loading on CeO$_2$ cubes also causes increasing lattice contraction (Table 4.1).

Table 4.2: Physical properties of bare CeO$_2$.

Catalysts	S_{BET} (m^2/g)	CeO$_2$ crystallite size (nm)^a	Lattice parameter (nm)^b
CeO$_2$/r	65	12.7	0.5420
CeO$_2$/o	41	18.6	0.5433
CeO$_2$/c	15	25.8	0.5442

a= calculated using Scherrer's equation, b= calculated using equation $LP=\sqrt{d^2\times(h^2+k^2+l^2)}$ where d is lattice spacing, calculated using Bragg's equation and (h, k, l) are Miller indices.

4.3.2. Transmission electron microscopy

TEM images (Figure 4.2a, d, g) show the morphology of CeO$_2$/c, CeO$_2$/o, and CeO$_2$/r. Shapes are known to be stable up to a temperature of 500°C (34,35) and no deformation of shapes is observed in this study. CeO$_2$/r with an interplanar spacing of 0.32nm indicates the presence of {111} lattice fringes (Figure 4.2i), while CeO$_2$/c expose mainly {100} lattice fringes with an interplanar spacing of 0.27nm (Figure 4.2a). It has been confirmed previously using AC-TEM that the exposed facets on CeO$_2$/c are {100} while CeO$_2$/r and CeO$_2$/o exposed {111} facets,[22] although it should be noted that discussion on this is ongoing.

TEM images of NiO/CeO$_2$ (Figure 4.2b, e, h) shows NiO particles of typically 3nm, agreeing well with the particle size calculated based on H$_2$-TPD (Table 4.1). Unfortunately, the particle size distribution could not be determined because of poor contrast between Ce and Ni.

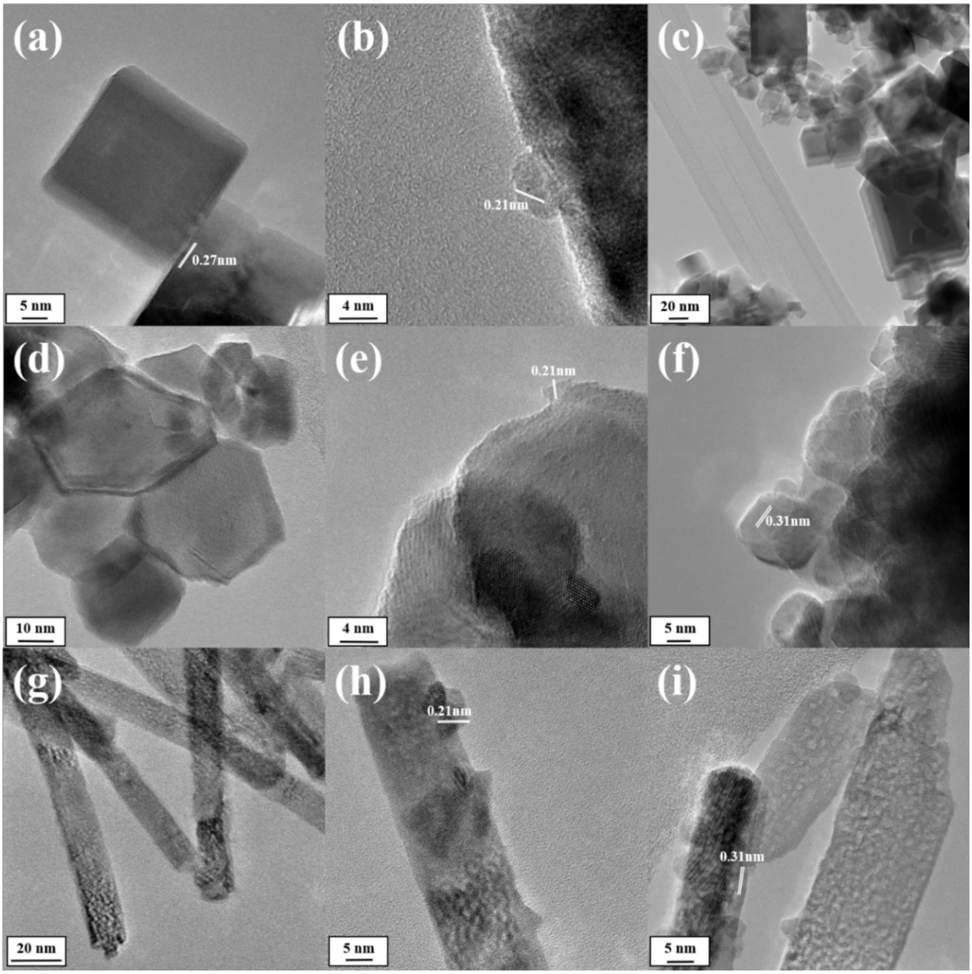

Figure 4.2: TEM images of nano-shaped CeO_2 (a, d, g) and NiO/CeO_2 catalysts, fresh (b, e, h) and used (c, f, i). Cube, octahedra and rod shapes are presented in (a, b, c), (d, e, f) and (g, h, i) respectively.

4.3.3. H_2 temperature-programmed reduction

The H_2-TPR profile (Figure 4.3a) of bare CeO_2 is similar to results reported previously (16). Peaks observed between 350 and 500°C are assigned to surface reduction, while bulk CeO_2 reduces at temperatures above 650°C (36). The relatively sharp peak at low temperature for CeO_2/c is confirming the high reactivity and accessibility of oxygen anions positioned out-of-plane in the (100) facets (37). H_2 consumption, calculated by integrating the peaks between 350 and 550°C, is also similar to our previous study, decreasing in the order CeO_2/r (510 μmol/g) > CeO_2/o (170 μmol/g) > CeO_2/c (110 μmol/g). In all three samples, the amount of oxygen removed is less than 1ML. The composition of the CeO_2 shapes after reduction in TPR is in the order $CeO_{1.956}$ for rods, $CeO_{1.986}$ for octahedra and $CeO_{1.99}$ for cubes. This confirms that the reduction of bare CeO_2 is morphology dependent and CeO_2/r forms more oxygen vacancies than other two shapes (38).

Table 4.3: H_2-TPR data of NiO/CeO_2.

Catalysts	H_2 consumption (μmol/g-cat.) to reduce				Reduction degree [e]
	NiO/CeO_2 [a] (A)	NiO [b] (B)	O_2^- species [c] (C)	CeO_2 [d] (A-B-C)	
NiO/CeO_2/r/3.2	3865	402	1909	1554	$CeO_{1.866}$
NiO/CeO_2/o/3.1	1878	321	492	1065	$CeO_{1.908}$
NiO/CeO_2/c/2.9#	794	214	90	490	$CeO_{1.958}$
NiO/CeO_2/c/2.5	705	187	56	462	$CeO_{1.960}$
NiO/CeO_2/c/2.9#	794	214	90	490	$CeO_{1.958}$
NiO/CeO_2/c/3.8	951	281	44	626	$CeO_{1.946}$
NiO/CeO_2/c/4.2	1111	321	56	734	$CeO_{1.936}$
NiO/CeO_2/c/4.7	1200	361	66	773	$CeO_{1.934}$

a= measured by integrating all peaks in TPR, b= calculated assuming complete reduction of NiO (incorporation of NiO into CeO_2 is not considered), c= estimated by integrating first (α) peak in TPR, d= H_2 consumption associated with reduction of CeO_2 via H-spillover, e= composition of CeO_{2-x} at the end of reduction, assuming x=0 before reduction (contribution of α peak is not considered in calculation). # represents identical samples.

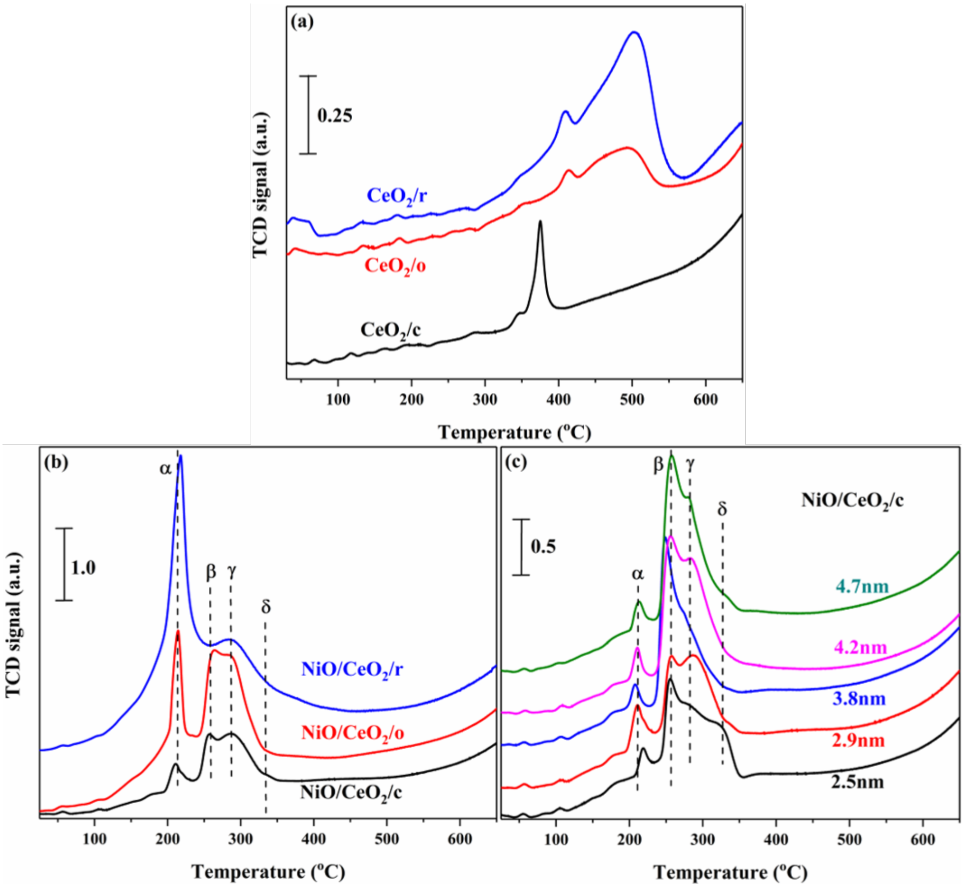

Figure 4.3: H_2-TPR profile of CeO_2 and NiO/CeO_2 with different morphologies: (a) bare CeO_2, (b) NiO/CeO_2 and (c) $NiO/CeO_2/c$ with different Ni particle size. Catalysts wt.: 20 ±0.5 mg, heating rate: 5°C/min, Gas: 5%H_2/Ar (20 ml/min).

H_2-TPR profile of NiO/CeO_2 (Figure 4.3b, c) shows four peaks (α, β, γ, and δ), similar to TPR results reported in the literature. The peak at 220°C (α) is assigned to surface active oxygen (O_2^-) adsorbed on oxygen vacant sites (28, 39–41), which are formed due to the incorporation of Ni^{2+} in the CeO_2 lattice, replacing Ce^{4+}. There is no general agreement on the assignments of β, γ and δ peaks in literature. It has been speculated that the extent of interaction of NiO with CeO_2 and the size of NiO clusters give rise to different peaks (40, 41). Stepwise reductions of NiO, i.e. $NiO \rightarrow Ni^{\delta+} \rightarrow Ni^0$, is also suggested to result in two different peaks (39, 42). H_2 consumption for the NiO/CeO_2 catalysts is reported in Table 4.3, calculated by integrating all four (α, β, γ, and δ) peaks. All catalysts consumed significantly more H_2 than would be required for complete reduction of NiO, presented as theoretical H_2 consumption in Table 4.3. This is providing clear evidence for spillover of H_2 to CeO_2 and its partial reduction (41, 43). The absence of peaks above 400°C also implies that the peaks observed at a relatively high temperature in bare CeO_2 (Figure 4.3a) have shifted to a lower temperature, especially for NiO/CeO_2/r and NiO/CeO_2/o. The amount of oxygen removed during the reduction is well above a monolayer for all samples, indicating significant diffusion of oxygen vacancies to the bulk of CeO_2 (44).

The H_2 consumption according to the first peak (α) in TPR of NiO/CeO_2 (Figure 4.3b) decreases in the order rods > octahedra > cubes (Table 4.3); after normalization based on the surface area, the same order remains (not shown). This shows that rods contain the highest concentration of oxygen vacant surface sites, caused by extensive incorporation of Ni^{2+}.

The reduction degree of CeO_2 in NiO/CeO_2 catalysts (Table 4.3) was calculated based on the total H_2 consumption, after subtraction of the H_2 consumption associated with a reduction of NiO as well as the α peak. The reduction degree decreases in the order rods > octahedra > cubes, indicating generation of more oxygen vacancies on rods via H-spillover. Typically, 2 to 3 ML of oxygen is removed from CeO_2 cubes during TPR, apparently via H-spillover from Ni to the CeO_2 surface. The consumption of H_2 increases with increasing Ni loading on all catalysts, also after correcting for H_2 consumption caused by NiO reduction (Table 4.3) as described above.

4.3.4. Raman spectroscopy

Raman spectra of CeO_2 and NiO/CeO_2 (Figure 4.4) at ambient temperature show a strong band at 460cm^{-1} due to F_{2g} band of CeO_2 fluorite phase. Please note that the Raman spectra are normalized using the intensity of the main peak at 460 cm^{-1}. The weak band at around 600cm^{-1} is assigned to defect induced (D) mode (45), indicative for the presence of oxygen vacancies. Therefore, the intensity ratio of I_D/I_{F2g} is considered as a measure for the oxygen vacancy concentration in the catalyst (46). This I_D/I_{F2g} ratio for bare CeO_2 (Figure 4.4a, Table 4.4) decreases in the order rods > octahedra ≈ cubes, suggesting that CeO_2/r contains the highest concentration of oxygen vacancies.

Table 4.4: Raman and XPS data of varying morphologies of CeO_2 and NiO/CeO_2.

Sample	Raman I_D/I_{F2g}	XPS	
		$Ce^{3+}_{conc.}$	O_V/O_L
CeO_2/r	0.07	0.22	0.32
CeO_2/o	0.012	0.19	0.30
CeO_2/c	0.014	0.21	0.36
NiO/CeO_2/r	0.94	0.26	0.39
NiO/CeO_2/o	0.41	0.25	0.36
NiO/CeO_2/c	0.07	0.23	0.37

The presence of NiO on CeO_2 causes a significant increase in the I_D/I_{F2g} ratio (Figure 4.4b, Table 4.4). This confirms the diffusion of Ni^{2+} into CeO_2 lattice (45), generating oxygen vacancies due to the charge difference between Ni^{2+} and Ce^{4+}. The I_D/I_{F2g} ratio (Table 4.4) depends significantly on the shape of CeO_2, decreasing in the order rods > octahedra > cubes. High oxygen vacancy concentration in NiO/CeO_2/r might be the result of the increasing extent of incorporation of Ni^{2+} in CeO_2, due to higher NiO content (47). The same effect is observed when increasing Ni particle size on cubes (Figure 4.4c).

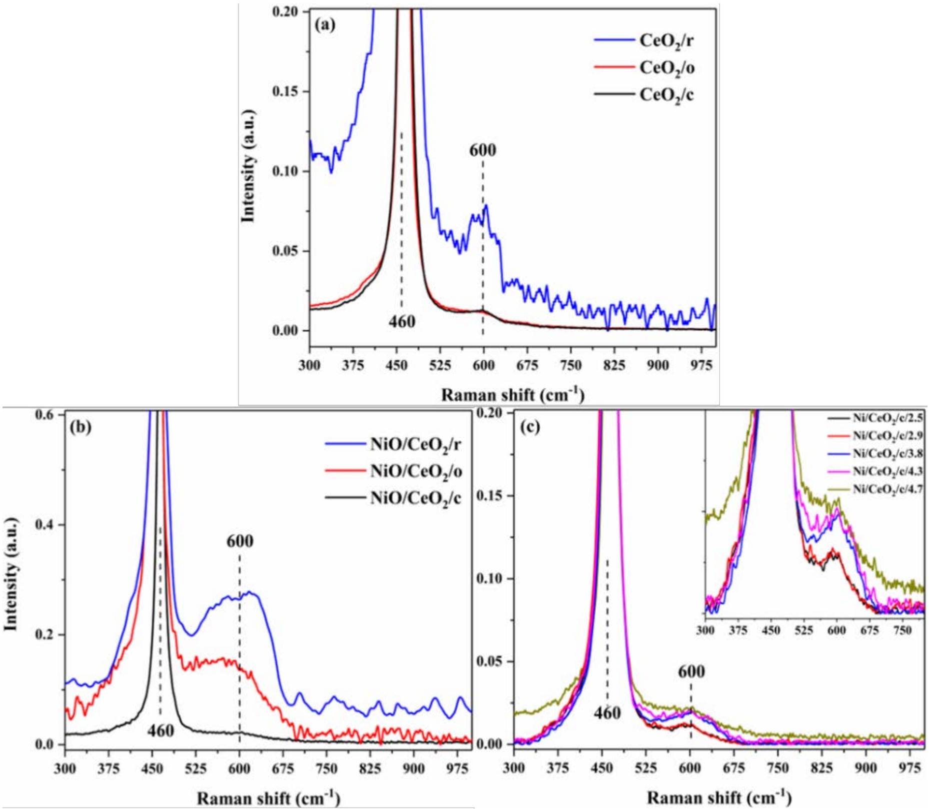

Figure 4.4: Raman spectra (ex-situ) of samples with different morphologies of (a) bare CeO_2, (b) NiO/CeO_2 and (c) $NiO/CeO_2/c$ with different Ni particle size. All spectra are normalized based on the intensity of the main peak at 460 cm^{-1}.

4.3.5. X-ray photoemission spectroscopy

The surface composition and oxidation states of CeO_2 and NiO/CeO_2 have been measured with XPS. Ce3d spectra of CeO_2 (Figure S4.2) and NiO/CeO_2 (Figure 4.5) show two distinct oxidation states of cerium in a rather complex spectrum. Six peaks centered at 882.3, 888.7, 896.0, 900.8, 907.2 and 916.6eV are assigned to Ce^{4+} whereas three peaks at 885.1, 898.2 and 903.3eV are due to Ce^{3+} (48). All nine peaks were quantified by deconvolution assuming Gaussian peak shape, keeping the peak positions fixed. The concentration of Ce^{3+} was quantified in Table 4.4 using the method described in literature (28,33), resulting in similar values for the three bare CeO_2 shapes. The Ce^{3+} concentration increases slightly on the addition of NiO for all three samples.

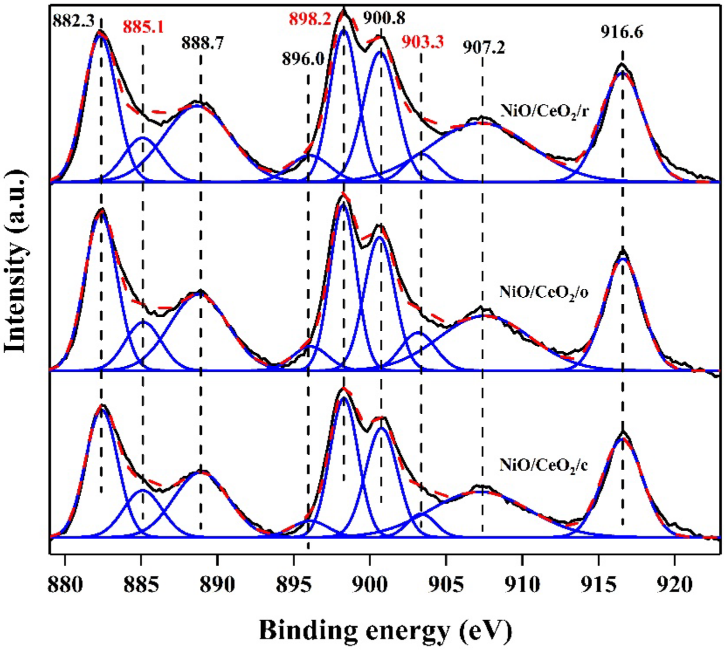

Figure 4.5: XPS spectra of samples with different morphologies of NiO/CeO_2, showing Ce 3d line. Binding energy in red color indicates the Ce^{3+} contribution. (Black line: experimental data, red dashed–line: fitted curve, blue line: de-convoluted peaks)

Figure 4.6a and Figure S4.3 present O1s spectra deconvoluted in 3 peaks, assuming Gaussian peak shape. The peak positioned at 529.2eV can be assigned to lattice oxygen (O_L) which has no neighboring oxygen vacancies. The peak at 531.3eV is characteristic for oxygen (O_V) with oxygen vacancies in close proximity (49). Therefore, the ratio of O_V/O_L can be considered as a measure for the concentration of oxygen vacancies present on the sub-surface. Table 4.4 presents O_V/O_L ratios for bare CeO_2 and for NiO/CeO_2, varying only slightly with the morphology of CeO_2. A minor peak at 533.1eV has been assigned to surface hydroxyl groups or carbonate groups (50).

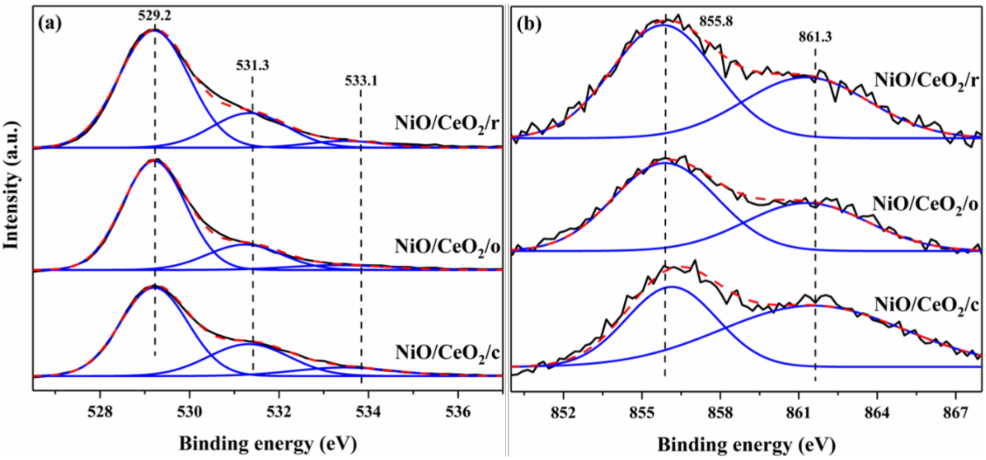

Figure 4.6: XPS spectra of NiO/CeO_2 with different morphologies, showing the O 1s line (a) and the Ni 2p line (b). (Black line: experimental data, red dashed–line: fitted curve, blue line: de-convoluted peaks)

Ni2p spectra (Figure 4.6b) shows the main peak around 855.8eV for all three catalysts, corresponding to the Ni $2p_{3/2}$ line and a satellite peak around 861.3eV. Both peaks are characteristic peaks of Ni^{2+} species present in NiO (41).

4.3.6. Performance of catalysts

Figure 4.7 presents the CO_2 conversion during methanation, starting at 200°C followed by stepwise increasing up to 400°C. The measurement was repeated at 230°C at the end of the experiment to ensure that no deactivation occurred. Clearly, Ni/CeO_2/r is more active than catalysts supported on cubes and octahedra. The selectivity to CH_4 was at least 99% in all three catalysts producing less than 1% CO (not shown). TEM images of spent catalysts (Figures 4.2c, f, i) confirms that CeO_2 retain its shape during catalytic measurements between 200 and 400°C.

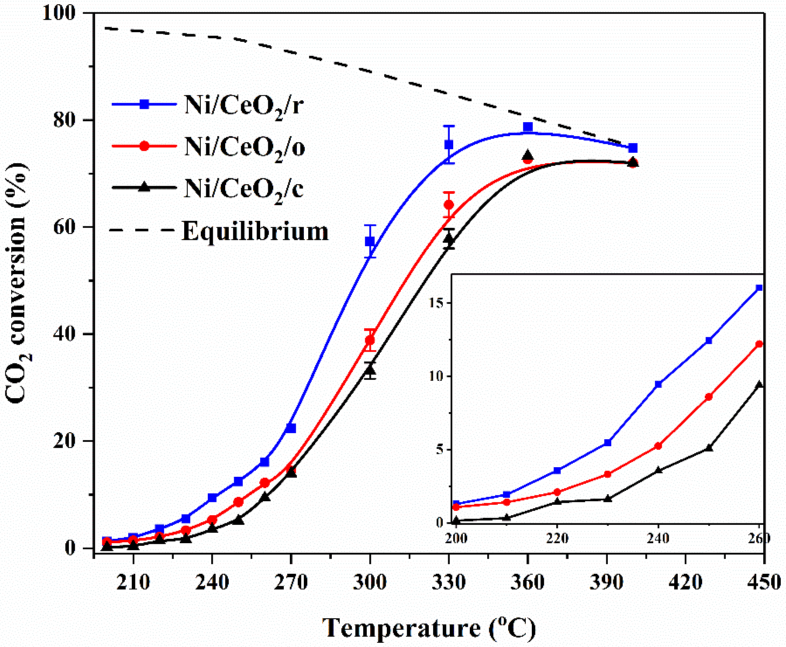

Figure 4.7: CO_2 conversion with respect to the temperature of Ni/CeO_2 catalysts. Inset figure represents the magnified view of CO_2 conversion at low temperatures (200-260°C). (wt. of catalyst: 50mg, $H_2:CO_2=4$, GHSV=48000h^{-1})

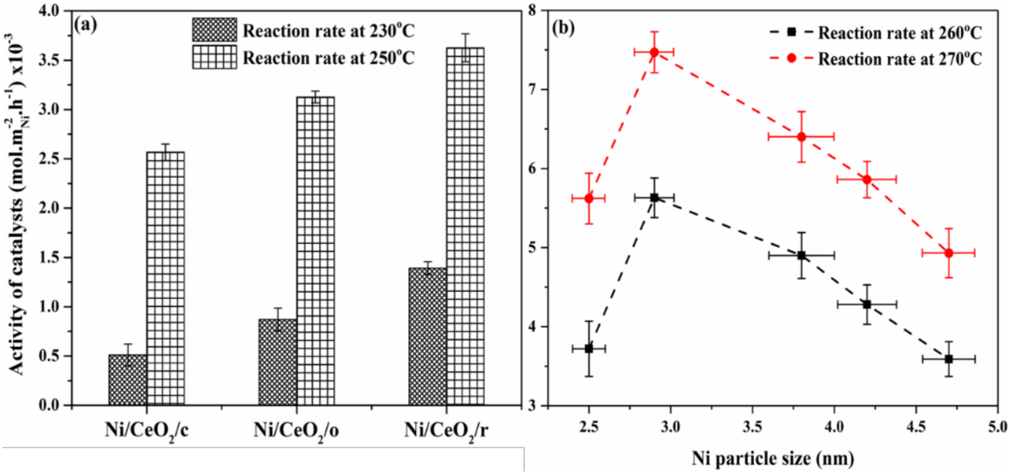

Figure 4.8: Activity of Ni/CeO_2 with (a) different morphologies and (b) different Ni particle size on cube-shaped CeO_2. (wt. of catalyst: 50mg, $H_2:CO_2=4$, GHSV=48000h^{-1}).

Figure 4.8 presents the activity of the Ni/CeO$_2$ catalysts under differential conditions, obtained at relatively low temperatures. At 250°C (Figure 4.8a), rods (3.63×10^{-3} mol $h^{-1}m_{Ni}^{-2}$) showed the highest reaction rate followed by octahedra (3.13×10^{-3} mol $h^{-1}m_{Ni}^{-2}$) and cubes (2.56×10^{-3} mol $h^{-1}m_{Ni}^{-2}$). Figure 4.8b shows that 2.9nm particles exhibit the highest activity per unit of Ni surface area for catalysts supported on cubes. Both smaller, as well as larger particles, have less catalytic activity. Figure 4.9 shows limited but significant CO formation (up to 3%) on the smallest Ni particles, while CO formation was below the detection limit for catalysts with Ni particles larger than 3nm.

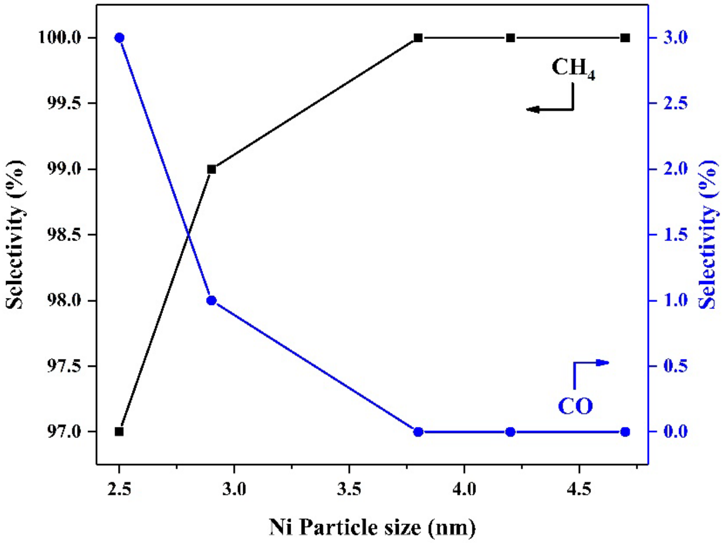

Figure 4.9: Selectivity for CH$_4$ and CO of Ni/CeO$_2$ catalysts with increasing Ni particle size (wt. of catalyst: 50mg, temperature: 270°C, GHSV=48000h^{-1})

4.4. General Discussion

Effect of CeO$_2$ morphology was studied while keeping the Ni particle size constant on cubes, rods and octahedra-shaped CeO$_2$, while the effect of Ni particle size was studied on cube-shaped CeO$_2$.

In general, Ni/CeO$_2$ catalysts are known to be excellent catalysts for CO$_2$ methanation due to high activity, selectivity and low cost. Unfortunately, there are only a few studies reporting performance under or close to differential conditions. Ratchahat et. al. (51) reported an activity of 0.63 $mol.h^{-1}.g_{Ni}^{-1}$ (T=200°C, Ni=10%, S.V.=60 l/h/g) while Atzori et. al. (52) obtained 2.96 $mol.h^{-1}.g_{Ni}^{-1}$ (T=300°C, Ni=15%, S.V.=72 l/h/g). Moreover, an activity of 0.2 $mol.h^{-1}.g_{Ni}^{-1}$ (T=230°C, Ni=5%, S.V.=24 l/h/g) has been also reported for Ni/CeO_2 catalyst (28). Similar CO_2 concentration (10%, v/v) was used for these studies, comparable with our work. The Arrhenius plot (Figure S4.4) shows good agreement with the result of Bian et. al. (28), while Ratchahat et. al. (51) reports a much higher activity caused by a very high metal surface area. The figure also shows a small but significant difference in the apparent activation barrier for the different CeO_2 shapes, which is also comparable to the literature (28).

4.4.1. Effect of Ni particle size

The activity of the catalysts supported on cubes varies with the averaged Ni particle size according to a volcano-type curve; 2.9nm Ni particles show the highest activity per m^2 Ni surface area (Figure 4.8b). The effect of Ni particle size on the performance of CO_2 methanation catalysts was studied previously, using various supports. Previous work on zirconia supported catalysts, including Y-stabilized zirconia, is unfortunately limited to much larger Ni particles and no clear trend between particle size and reaction rates per m^2 Ni is reported (53, 54). In contrast, Chen et. al. (55) reported decreasing activity (per m^2 Ni) of Ni/SiO_2 catalysts with increasing Ni particle size (2.7-4.7nm). The highest activity was observed for the 2.7nm catalyst, in good agreement with our results; unfortunately, this study don’t report on Ni particles smaller than 2.7nm.

Moreover, Vogt et. al. (56) also reported that 2.5nm Ni particles show the highest activity for SiO_2 supported Ni when the Ni particles size between 1.1 and 6.9nm. They suggest this is correlated to the strength of CO adsorption on Ni, which is increasing with particle size. Yao et. al. (57) indeed reported increasing strength of CO adsorption, resulting in high CO coverage on large Ni particles. As discussed in the introduction, CO is an intermediate in the reaction scheme, irrespective of the reaction pathway (Scheme 4.1). Following the argument of Vogt et. al. (56), the activity of small Ni particles is limited due to too weak adsorption of CO, causing not only weak activation of the CO bond but also some CO desorption. Large particles, on the other hand, adsorb CO too strongly, decreasing the reactivity according to Sabatier's principle. Importantly, the rate of conversion is further suppressed because of poisoning with CO, hampering chemisorption of H_2. Ni particles of 2.9nm seem most active due to the appropriate intermediate strength of adsorption of CO, similar to what is reported for silica supported catalysts. This explanation is in line with the observation that CO is detected exclusively on small Ni particles as shown in Figure 4.9. It should be noted though that the highest activity reported by Vogt (56) (5.6×10^{-3} mol $h^{-1}m_{Ni}^{-2}$) for 2.5nm Ni particles on silica at 400°C is significantly lower than the activity of Ni on CeO$_2$ in this study (7.5×10^{-3} mol $h^{-1}m_{Ni}^{-2}$) for 2.9nm Ni particles at much lower temperature 270°C. Further experimental condition i.e. H_2 and CO_2 concentrations are similar. In short, the effect of Ni particle size on activity for CeO$_2$ and SiO$_2$ supported catalyst is similar, but the activity of CeO$_2$ supported catalysts is much higher, which will be discussed later in terms of the bi-functional role of CeO$_2$ support.

4.4.2. Effect of CeO$_2$ morphology

The discussion above implies that any effect of the shape of the CeO$_2$ support on catalyst activity can be judged only if the Ni dispersion and thus particle size are kept constant. Since the activity in this study is normalized on the Ni surface area, the difference in the activity is strictly associated with the morphology of CeO$_2$ and is not influenced by the Ni loading: activity decreases in the order of rods > octahedra > cubes (Figure 4.8a), whereas the apparent activation barrier also decrease in the same order (Figure S4.4). The same trend in the activity was also reported by Bian et. al. (28) using Ni/CeO$_2$ catalysts. Although the variation in Ni dispersion does not influence the order of activity of Ni/CeO$_2$ nano-shapes (rods > cubes), the magnitude of the effect is influenced as the ratio between the activities of rods and cubes at 230°C observed by Bian (1.8) is smaller compared to our observations (2.5). In contrast, for Ru on CeO_2, the effect of metal particles size is so large that the order in the activity of Ru on different CeO_2 shapes reversed.[16,29] We will now discuss possible underlying reasons for the effect of CeO_2 shape on activity.

Raman (I_{F2g}/I_D, Table 4.4) and H_2-TPR (Figure 4.3a, Table 4.3) data for bare CeO_2 are very similar to our previous study (16). It was concluded that the trend in the oxygen vacancy concentration after calcination, as well as the extent of reduction during TPR, decreases in the order rods > octahedra > cubes. The same trend in the oxygen vacancy concentration is also confirmed by XRD, based on changes in the lattice parameter (Table 4.2). On the other hand, XPS analysis (Ce^{3+} concentration and O_V/O_L ratio, Table 4.4) indicate similar oxygen vacancy concentration in the sub-surface of all three shapes of CeO_2.

Two types of oxygen vacancies need to be considered for Ni/CeO_2 catalysts, i.e. vacancies formed due to the Ni^{2+} incorporation by replacing Ce^{4+} ions and vacancies formed via reduction of Ce^{4+} to Ce^{3+} with H_2, which is possible at mild temperatures via H-spillover. The first type of oxygen vacancy formed due to the incorporation of metal ions (M^{2+} or M^{3+}) is consistent with the literature (58–60). High concentration of NiO generates more oxygen vacancies, as confirmed with XRD (lattice contraction, Table 4.1) and Raman spectroscopy (Figure 4.4c) for $NiO/CeO_2/c$. Lattice contraction according to XRD (lattice parameter, Table 4.1) indicates decreasing incorporation of Ni^{2+} in the order rods > octahedra > cubes. Raman spectroscopy (I_{F2g}/I_D, Table 4.4) results confirm that the oxygen vacancy concentration decreases in the same order. The same trend was also observed for the oxygen vacancies on the surface induced by incorporation of Ni^{2+}, detected as the α-peak at 220°C in H_2-TPR (Figure 4.3b), assigned to the removal of O_2^- species adsorbed on these sites. In short, characterization results of calcined NiO/CeO_2 confirms high oxygen vacancies concentrations in both surface and bulk of rods, due to the presence of more NiO compared to octahedra and cubes. It should be noted that these oxygen vacancies formed due to Ni^{2+} incorporation are not likely to participate in a catalytic redox cycle. XPS analysis shows only a minor increase in O$_V$/O$_L$ ratio (Table 4.4) for three catalysts after NiO addition. Remarkably, the O$_V$/O$_L$ ratio seems not to probe oxygen vacancies induced by Ni^{2+} incorporation.

The second type of oxygen vacancies, i.e. associated with Ce^{3+} cations, are redox active and can participate in the catalytic cycle. XPS analysis of calcined catalysts showed no considerable difference in Ce^{3+} concentration (Table 4.4) for different morphologies, suggesting similar oxygen vacancy concentration for all three catalysts before reduction. The concentration of this type of oxygen vacancy increases significantly during the reduction step, enhanced by H-spillover, which is consistent with the literature (52). Reactivity of catalysts during reduction was similar since all three catalysts reduced in the same temperature window between 150 and 350°C (Figure 4.3), although the extent of reduction was different for different shapes of CeO$_2$ (Table 4.3). The trend in the reduction degree of Ni/CeO$_2$ decreases in the order rods > octahedra > cubes (Table 4.3), indicating that more oxygen vacancies are generated in rods during TPR.

The trend in the activity of catalysts (rods > octahedra > cubes) agrees well with the trend in the reduction degree during H$_2$-TPR, suggesting that facile formation of oxygen vacancies, i.e. high reducibility, leads to high activity for methanation. The same trend has been reported previously for Ni on ZrO$_2$ modified Al$_2$O$_3$, (61) as well as in our previous work (16) on Ru/CeO$_2$.

This would suggest, as discussed before,[16] that reactive adsorption of CO$_2$ at an oxygen vacancy (step 1, Scheme 4.1) is rate determining. Previous literature also suggests only one rate-determining step for Ni and Ru supported on CeO$_2$ catalysts in CO$_2$ methanation (12, 62). However, the Ni metal particle size is influencing the reaction rate and apparently another step on the Ni surface is also rate-determining. We suggest adsorbed H and a C-containing species, i.e. CO, COH$_x$ or CH$_y$, are involved. Competitive adsorption of H with these C-containing species influences the rate of this step. In short, both reactive adsorption of CO_2 on defective CeO_2 as well as a hydrogenation step on the Ni surface determine the overall rate. Direct CO_2 dissociation on the Ni surface also contribute.

4.5. Conclusions

This study reports on the effect of Ni particle size and CeO_2 morphology on the performance in CO_2 methanation. The activity is particle size dependent and 2.9nm Ni particles result in the highest activity per unit Ni surface area. The particle size effect is assigned to variation in the CO adsorption strength with particle size, which is consistent with the formation of CO as a byproduct exclusively on the smallest Ni particles. Larger particles adsorb CO too strongly causing poisoning of the Ni surface and consequently too low H coverage, whereas smaller particles adsorb CO too weakly causing slow C-O dissociation.

Rigorous comparison of the activity of catalysts on different CeO_2 nano-shapes is only possible if the metal particle size kept constant. This is now clearly demonstrated for CO_2 hydrogenation over CeO_2 supported Ru[16] and Ni in this study. Many of the studies on the effect of CeO_2 morphology have not considered this and further research would be needed to clarify this point. For CO_2 hydrogenation, the activity of 3nm Ni particles on CeO_2 is morphology dependent, decreasing in the order rods > octahedra > cubes. Characterization results reveal the presence of two types of oxygen vacancies: vacancies formed due to the incorporation of Ni^{2+} (redox-inactive) and vacancies formed via reduction of CeO_2 during reduction via H-spillover (redox-active). The activity of the catalyst increases with the increasing facile formation of redox-active oxygen vacancies.

The activity of Ni on CeO_2 is therefore influenced by at least two rate-determining steps, i.e. reactive adsorption of CO_2 on redox active sites at the CeO_2 surface, as well as by hydrogenation of a carbon-containing intermediate on the Ni surface.

Reference

(1) Janna V. Veselovskaya, Pavel D. Parunin, Olga V. Netskina, Lidiya S. Kibis, Anton I. Lysikov, Aleksey G. Okunev. *Energy* **2018**, 159, 766–773.

(2) Karim Ghaib, Fatima-Zahrae Ben-Fares. *Renewable and Sustainable Energy Rev.* **2018**, 81, 433–446.

(3) Hao Zhang, Fengsen Zhu, Xiaodong Li, Kefa Cen, Changming Du, Xin Tu. *Plasma Chem. Plasma Process.* **2016**, 36, 813–834.

(4) Xiao Chen, Steven L Suib, Yuji Hayashi, Hiroshige Matsumoto. *J. Catal.* **2001**, 201, 198–205.

(5) Shohei Tada, Teruyuki Shimizu, Hiromichi Kameyama, Takahide Haneda, Ryuji Kikuchi. *Int. J. Hydrogen Energy* **2012**, 37, 5527–5531.

(6) A. D. Tomsett, T. Hagiwara, A. Miyamoto, T. Inui. *Appl. Catal.* **1986**, 26, 391–394.

(7) Xiong Su, Jinghua Xu, Binglian Liang, Hongmin Duan, Baolin Hou, Yanqiang Huang. *J. Energy Chem.* **2016**, 25, 553–565.

(8) Karim Ghaib, Korbinian Nitz, Fatima-Zahrae Ben-Fares. *ChemBioEng Rev.* **2016**, 3, 266–275.

(9) M. A. A. Aziz, A. A. Jalil, S. Triwahyono, A. Ahmad. *Green Chem.* **2015**, 17, 2647–2663.

(10) Muhammad Younas, Leong Loong Kong, Mohammed J. K. Bashir, Humayun Nadeem, Areeb Shehzad, Sumathi Sethupathi, *Energy Fuels* **2016**, 30, 8815−8831.

(11) Thien An Le, Min Sik Kim, Sae Ha Lee, Tae Wook Kim, Eun Duck Park. *Catal. Today* **2017**, 293–294, 89–96.

(12) Fei Wang, Shan He, Hao Chen, Bin Wang, Lirong Zheng, Min Wei, David G. Evans, Xue Duan. *J. Am. Chem. Soc.* **2016**, 138, 6298−6305.

(13) Jun Ren, Hailong Guo, Jinzhou Yang, Zhifeng Qin, Jianying Lin, Zhong Li. *Appl. Surf. Sci.* **2015**, 351, 504–516.

(14) Sudhanshu Sharma, K. B. Sravan Kumar, Yash M. Chandnani, V. Sai Phani Kumar, Bhanu P. Gangwar, Aditi Singhal, Parag A. Deshpande. *J. Phys. Chem. C* **2016**, 120, 14101−14112.

(15) Alfredo Solis-Garcia, Jose F. Louvier-Hernandez, Armando Almendarez-Camarillo, Juan C. Fierro-Gonzalez. *Appl. Catal. B* **2017**, 218, 611–620.

(16) Tushar Sakpal, Leon Lefferts. *J. Catal.* **2018**, 367, 171–180.

(17) Guilin Zhou, Huiran Liu, Kaikai Cui, Hongmei Xie, Zhaojie Jiao, Guizhi Zhang, Kun Xiong, Xuxu Zheng. *Int. J. Hydrogen Energy* **2017**, 42, 16108–16117.
(18) Lea R. Winter, Elaine Gomez, Binhang Yan, Siyu Yao, Jingguang G. Chen. *Appl. Catal. B* **2018**, 224, 442–450.
(19) Yang Yu, Zhoufeng Bian, Fujiao Song, Juan Wang, Qin Zhong, Sibudjing Kawi. *Top. Catal.* **2018**, 61, 1514–1527.
(20) Guilin Zhou, Huiran Liu, Kaikai Cui, Aiping Jia, Gengshen Hu, Zhaojie Jiao, Yunqi Liu, Xianming Zhang. *Appl. Surf. Sci.* **2016**, 383, 248–252.
(21) B. Murugan, A. V. Ramaswamy. *J. Am. Chem. Soc.* **2007**, 129, 3062–3063.
(22) Shilpa Agarwal, Leon Lefferts, Barbara L. Mojet, D. A. J. Michel Ligthart, Emiel J. M. Hensen, David R. G. Mitchell, Willem J. Erasmus, Bruce G. Anderson, Ezra J. Olivier, Johannes H. Neethling, Abhaya K. Datye. *ChemSusChem* **2013**, 6, 1898–1906.
(23) Nisha Singhania, E. A. Anumol, N. Ravishankar, Giridhar Madras. *Dalton Trans.* **2013**, 42, 15343–15354.
(24) Zong Hu, Xiaofei Liu, Dongmei Meng, Yun Guo, Yanglong Guo, Guanzhong Lu. *ACS Catal.* **2016**, 6, 2265−2279.
(25) Laura Torrente-Murciano, Francisco-Javier Garcia-Garcia. *Catal. Commun.* **2015**, 71, 1–6.
(26) Xianjun Du, Dengsong Zhang, Liyi Shi, Ruihua Gao, Jianping Zhang. *J. Phys. Chem. C* **2012**, 116, 10009−10016.
(27) Chenwei Li, Yu Sun, Igor Djerdj, Pascal Voepel, Carl-Christian Sack, Tobias Weller, Rüdiger Ellinghaus, Joachim Sann, Yanglong Guo, Bernd M. Smarsly, Herbert Over. *ACS Catal.* **2017**, 7, 6453−6463.
(28) Zhoufeng Bian, Yi Meng Chan, Yang Yu, Sibudjing Kawi. *Cat. Today* **2018**, DOI: 10.1016/j.cattod.2018.04.067.
(29) Fei Wang, Changming Li, Xiaoyu Zhang, Min Wei, David G. Evans, Xue Duan. *J. Catal.* **2015**, 329, 177–186.
(30) Hao-Xin Mai, Ling-Dong Sun, Ya-Wen Zhang, Rui Si, Wei Feng, Hong-Peng Zhang, Hai-Chao Liu, Chun-Hua Yan. *J. Phys. Chem. B* **2005**, 109, 24380–24385.
(31) Päivi Mäki-Arvela, Dmitry Yu Murzin. *Appl. Catal. A* **2013**, 451, 251-281.
(32) R. D. Shannon. *Acta Cryst.* **1976**, 32, 751–767.

(33) Xin Liao, Yin Zhang, Martyn Hill, Xin Xia, Yongxiang Zhao, Zheng Jiang. *Appl. Catal. A* **2014**, 488, 256–264.

(34) Oleksii S. Bezkrovnyi, Piotr Kraszkiewicz, MacIej Ptak, Leszek Kepinski. *Catal. Commun.* **2018**, 117, 94-98.

(35) Zili Wu, Meijun Li, Jane Howe, Harry M. Meyer III, and Steven H. Overbury. *Langmuir* **2010**, 26, 16595–16606.

(36) Francesca Giordano, Alessandro Trovarelli, Carlade Leitenburg, Massimiliano Giona. *J. Catal.* **2000**, 193, 273–282.

(37) Shilpa Agarwal, X. Zhu. Emiel J. M. Hensen, Barbara L. Mojet, Leon Lefferts. *J. Phys. Chem. C* **2015**, 119, 12423−12433.

(38) Zhentao Feng, Quanming Ren, Ruosi Peng, Shengpeng Mo, Mingyuan Zhang, Mingli Fu, Limin Chen, Daiqi Ye. *Cat. Today* **2018**, DOI: j.cattod.2018.06.039.

(39) Hale Ay, Deniz Üner. *Appl. Catal. B* **2015**, 179, 128–138.

(40) Ke Tang, Wei Liu, Jing Li, Jinxin Guo, Jingcai Zhang, Shuping Wang, Shengli Niu, Yanzhao Yang. *ACS Appl. Mater. Interfaces* **2015**, 7, 26839−26849.

(41) Carlos Alberto Chagas, Eugenio F. de Souza, Robinson L. Manfro, Sandra M. Landi, Mariana M. V. M. Souza, Martin Schmal. *Appl. Catal. B* **2016**, 182, 257–265.

(42) Shan Xu, Xingbin Yan, Xiaolai Wang. *Fuel* **2006**, 85, 2243–2247.

(43) Araceli Romero-Núñeza, Gabriela Díaz. *RSC Adv.* **2015**, 5, 54571–54579.

(44) Hui-Ying Li, Hai-Feng Wang, Yang-Long Guo, Guan-Zhong Lu, P. Hu. *Chem. Commun.* **2011**, 47, 6105–6107.

(45) Pal, P.; Singha, R. K.; Saha, A.; Bal, R.; Panda, A. B. *J. Phys. Chem. C* **2015**, 119, 13610−13618.

(46) Lianjun Liu, Zhijian Yao, Yu Deng, Fei Gao, Bin Liu, Lin Dong. *ChemCatChem* **2011**, 3, 978–989.

(47) Pei Zhao, Feng Qin, Zhen Huang, Chao Sun, Wei Shen, Hualong Xu. *Catal. Sci. Technol.* **2018**, 8, 276–288.

(48) Klaus-Dieter Schierbaum. *Surf. Sci.* **1998**, 399, 29–38.

(49) Tomo Hasegawa, Syed Mohammad Fakruddin Shahed, Yasuyuki Sainoo, Atsushi Beniya, Noritake Isomura, Yoshihide Watanabe, Tadahiro Komeda. *J. Chem. Phys.* **2014**, 140, 044711.

(50) Lj Kundakovic, David R. Mullins, Steven H. Overbury. *Surf. Sci.* **2000**, 457, 51–62.

(51) Sakhon Ratchahat, Masao Sudoh, Yuji Suzuki, Wataru Kawasaki, Ryo Watanabe, Choji Fukuhara. *J. CO_2 Util.* **2018**, 24, 210–219.
(52) Luciano Atzori, Maria Giorgia Cutrufello, Daniela Meloni, Daniela Monaci, Daniela Cannas, Delia Gazzoli, Maria Franca Sini, Paolo Deiana, Elisabetta Rombi. *Int. J. Hydrogen Energy* **2017**, 42(32), 20689–20702.
(53) Jagadesh Kopula Kesavan, Igor Luisetto, Simonetta Tuti, Carlo Meneghini, Giovanna Iucci, Chiara Battocchio, Settimio Mobilio, Stefano Casciardi, Renata Sisto. *J. CO_2 Util.* **2018**, 23, 200-211.
(54) Kechao Zhao, Weihan Wang, Zhenhua Li. *J. CO_2 Util.* **2016**, 16, 236-244.
(55) Ching-Shiun Chen, Canggih Setya Budi, Hung-Chi Wu, Diganta Saikia, Hsien-Ming Kao. *ACS Catal.* **2017**, 7, 8367−8381.
(56) Charlotte Vogt, Esther Groeneveld, Gerda Kamsma, Maarten Nachtegaal, Li Lu, Christopher J. Kiely, Peter H. Berben, Florian Meirer, Bert M. Weckhuysen. *Nat. Catal.* **2018**, 1, 127–134.
(57) Yunxi Yao, Zhen Yan, Long Chen, Zihao Zhou, Li Liu, D. Wayne Goodman. *Catal. Lett.* **2012**, 142, 1437–1444.
(58) Xiong-Shan Liu, Xu-Dong Wang, Man Yao, Wei Cui, Hui Yan. *Catal. Commun.* **2015**, 63, 35–40.
(59) Kai Yu, Da Lei, Yajun Feng, Haochen Yu, Yue Chang, Yanbing Wang, Yaqi Liu, Gui-Chang Wang, Lan-Lan Lou, Shuangxi Liu, Wuzong Zhou. *J. Catal.* **2018**, 365, 292–302.
(60) Michael Nolan. *J. Mater. Chem.* **2011**, 21, 9160–9168.
(61) Mengdie Cai, Jie Wen, Wei Chu, Xueqing Cheng, Zejun Li. *J. Nat. Gas Chem.* **2011**, 20, 318-324.
(62) M. V. Konishcheva, D. I. Potemkin, S. D. Badmaev, P. V. Snytnikov, E. A. Paukshtis, V. A. Sobyanin, V. N. Parmon. *Top. Catal.* **2016**, 59, 1424–1430.

Appendix

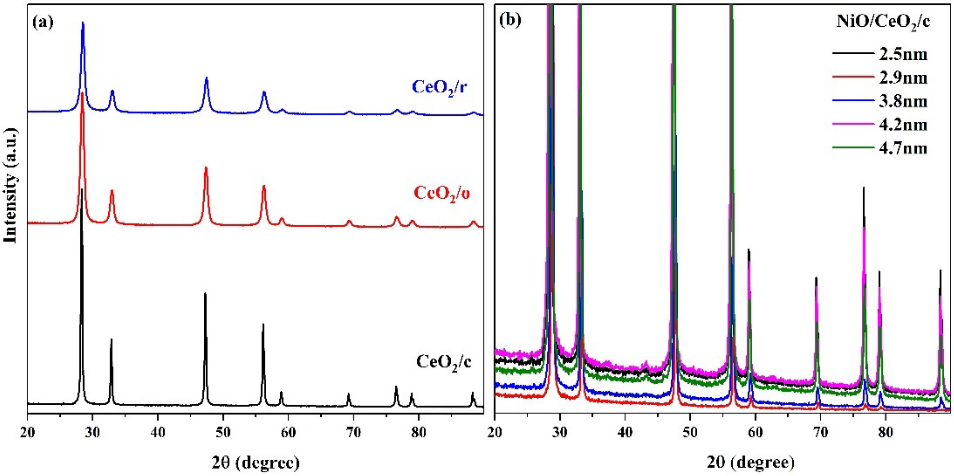

Figure S4.1: XRD patterns of (a) CeO_2 supports with well-defined facets and (b) NiO/CeO_2/c catalysts with different Ni particle size.

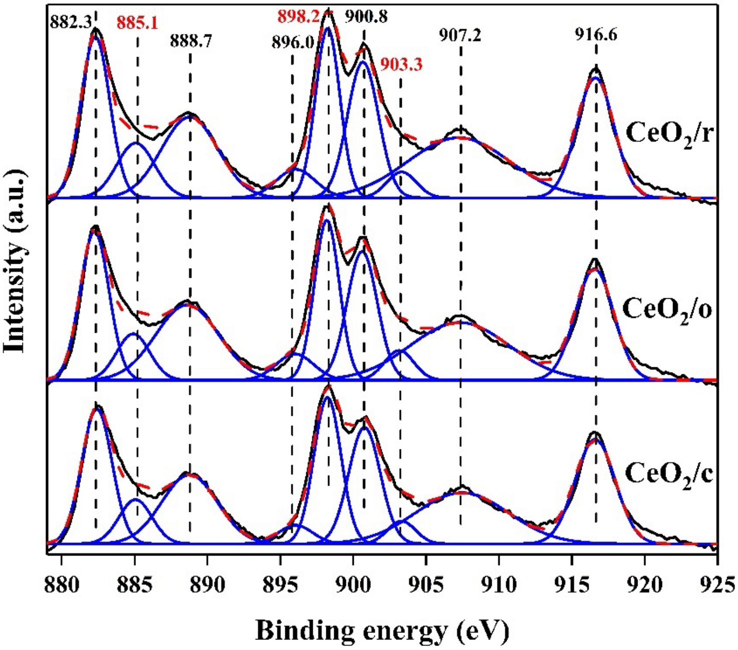

Figure S4.2: XPS spectra of Ce 3d for different morphologies of CeO_2. Binding energy in red color indicates the Ce^{3+} contribution. (Black line: experimental data, red dashed–line: fitted curve, blue line: de-convoluted peaks)

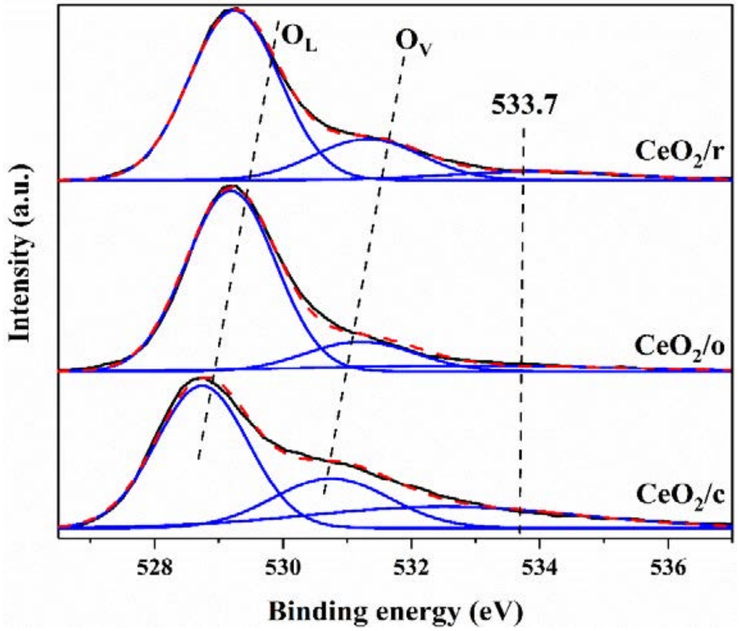

Figure S4.3: XPS spectra of O 1s for different morphologies of CeO2. (Black line: experimental data, red dashed–line: fitted curve, blue line: de-convoluted peaks)

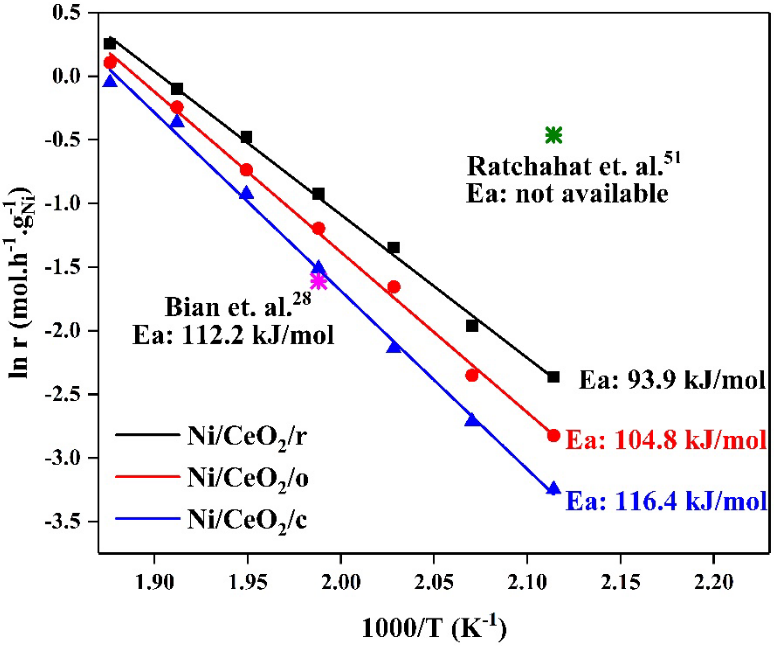

Figure S4.4: Arrhenius plot for the CO2 methanation over Ni/CeO2 catalysts with various CeO2 morphology. * represents data from literature. CO2 conversion was less than 20%.

Chapter 5

Conclusions and Perspective for future work

5.1. Conclusions

CO_2 methanation is considered as a promising reaction to store energy, as it forms CH_4 with simple C1 chemistry. Ru and Ni are the best catalysts among other tested catalysts for this reaction, due to their high activity, selectivity, and stability. Different support materials are also studied, which can be classified into reducible (e.g. CeO_2, ZrO_2, TiO_2) and non-reducible (e.g. Al_2O_3, SiO_2). CeO_2 based materials have attracted a lot of attention in recent past due to their bi-functional role, i.e. to support metal nanoparticles as well as activate CO_2 molecules. CeO_2 can easily switch between 3+ and 4+ oxidation state, without phase change, by releasing or accepting oxygen from its lattice. This unique redox property and presence of abundant oxygen vacancies make CeO_2 and CeO_2-based materials an excellent catalyst for CO_2 methanation.

Different nano-shapes of CeO_2, including cubes, rods, octahedra, and spheres, with well-defined crystal planes on the surface are reported in literature. The physical and redox properties of these CeO_2 nano-shapes differ significantly from each other, resulting in varying catalytic activity. Although, while comparing the activity of different shapes for CO_2 methanation, the effect of metal (Ni and Ru) particle size is often neglected. Ru-based catalysts showed cubes are more active than rods (1), whereas the opposite is reported for Ni-based catalyst (2). This suggests that the activity is not determined by CeO_2 morphology exclusively and might be influenced by the variation in metal particle size.

Therefore, in this study, we report that the activity of CO_2 methanation indeed depends on the metal (Ni and Ru) particle size. Hence, the effect of CeO_2 morphology on the activity of CO_2 methanation was studied by keeping the particle size constant on all CeO_2 shapes.

The first part of this thesis is dedicated to the effects of CeO_2 morphology and metal particle size using Ru/CeO_2 catalysts. **In chapter 2**, the effect of CeO_2 morphology is reported using Ru based catalysts. The performance of rod, octahedra, and cube-shaped CeO_2 supported on Ru, with constant particle size, is studied for CO_2

methanation. The highest activity of 11.0×10^{-8} mol $s^{-1}m_{Ru}^{-2}$ was observed for rod-shaped Ru/CeO_2 catalysts. The characterization results conclude that the addition of Ru increases the reducibility of bare CeO_2, lowering reduction temperature and generating more oxygen vacancies. The H_2 consumption measured using H_2-TPR shows oxygen removal equivalent to about 3ML, implying diffusion of vacancies into the subsurface or bulk of CeO_2. H_2-TPR, Raman, and XPS result further confirm that the rod-shaped Ru/CeO_2 possess higher oxygen vacancy concentration than cubes and octahedra, after oxidative as well as reductive conditions. The catalyst (Ru/CeO_2 rods) with most oxygen vacancies also exhibits the highest reaction rates, indicating that the oxidation of CeO_2 via CO_2 adsorption is a rate-determining step of the redox cycle. The trend in activity observed in this study is completely opposite to the trend reported by Wang. et. al. (1) using the same Ru/CeO_2 catalysts system. This confirms the significant influence of Ru particle size on the activity of catalysts.

To support the claims made in the previous chapter, in **chapter 3** we studied the structure-sensitivity in CO_2 methanation using rods-shaped Ru/CeO_2 catalysts. The activity of the catalysts shows a significant effect of Ru particle size, where 4.8nm Ru/CeO_2 catalyst exhibits the highest activity of 0.0045 mol $h^{-1}m_{Ru}^{-2}$ at 215^{o}C. The primary cause for the structure-sensitivity in Ru based catalysts can be assigned to the variation Ru particle size itself. Although, one cannot rule out an effect of CeO_2 support on the activity of catalysts via its redox properties. Raman and TPR results confirm that the dissolution of Ru^{4+} increases with metal loading and it decreases with increasing reduction temperature. The trend in Ru dissolution agrees well with the trend in activity per Ru surface area, suggesting that the presence of Ru opens a fast pathway to activate CO_2 via formation of a HCOO* intermediate. Therefore, from first part of thesis, we conclude that the CO_2 methanation reaction is structure-sensitive over Ru/CeO_2 catalysts and one should keep the particle size constant when studying the effect of CeO_2 morphology. Moreover, there are two rate-determining steps influencing the overall reaction rate, one on Ru and one on CeO_2 surface respectively.

In the second part of this thesis (**chapter 4**), CeO_2 morphology effect and influence of metal particle size is elucidated using Ni/CeO_2 catalysts. Catalysts with different Ni particle size (2.5-4.7 nm) shows different activity, with 2.9nm Ni catalysts showing the maximum activity of 7.54×10^{-3} mol $h^{-1}m_{Ni}^{-2}$ at 270°C. The highest activity of 2.9nm Ni particles is attributed to the intermediate strength of CO adsorption. The CO is one of the intermediate species formed on the active metal surface during the reaction. While weak CO adsorption on small Ni particles causes insufficient activation of the CO bond, bigger Ni particles cause CO poisoning due to strong adsorption of CO.

The effect of CeO_2 morphology was studied, keeping the Ni particle size (3nm) constant. Ni/CeO_2 rods showed the highest activity for CO_2 methanation compared to cubes and octahedra. Two types of oxygen vacancies were detected for all Ni/CeO_2 catalysts. Vacancies created by dissolution of Ni^{2+} ion into CeO_2 lattice are redox inactive and irrelevant, while those formed during reduction process via H-spillover are redox active. It should be noted that the oxygen vacancies are not formed in Ru/CeO_2 catalysts due to Ru^{4+} dissolution, as the oxidation state of Ce and Ru is same. The concentration of redox-active oxygen vacancies increases with increasing NiO loading and Ni/CeO_2 rods showed the highest concentration of oxygen vacancy.

The correlation between activity and reducibility of Ni/CeO_2 catalysts with different morphology suggests that activation of CO_2 on oxygen vacancies is a rate-determining step. Although, the impact of the Ni particle size of activity also indicates that a hydrogenation step of a carbon-containing species on the Ni surface also influences the overall activity. The presence of two rate-determining steps on Ni/CeO_2 catalysts is consistent with the conclusions for Ru/CeO_2 catalysts, reported in first part of the thesis.

The trend in activity reported in chapter 4 agrees with the trend reported by Bian et. al. (2) using Ni/CeO_2 catalysts. Even though the variation in Ni dispersion does not influence the order of activity of Ni/CeO_2 nano-shapes (rods > cubes), the magnitude of effect is significantly influenced by Ni dispersion as the ratio between the activities of rods and cubes observed by Bian (1.8) is smaller compared to our observations (2.5).

From this work, it is clear that the activity of catalysts for CO_2 methanation can be influenced significantly by the particle size of Ru and Ni. Due to variation in metal dispersion, Wang et. al. (1) and Bian et. al. (2) observed the opposite trend in activity of different shapes of CeO_2 for the same reaction using Ru- and Ni-based catalysts, respectively. We, on the other hand, observed the same trend in the activity of CeO_2 cubes and rods for both Ru and Ni catalysts. Furthermore, the magnitude of the effect is also similar for Ru/CeO_2 (2.3) and Ni/CeO_2 (2.5) catalysts studied in this thesis.

The direct influence of metal particle size could also contribute to the structure-sensitivity of catalysts for CO_2 methanation. In **chapter 3 and 4**, we discussed different literature reported on particle size effects in Ru and Ni catalysts supported on reducible and non-reducible oxides. It has been made clear that the different sizes of metal particles lead to the difference in its electronic structure, population of low coordination sites and strength of CO interaction, which significantly affects the activity per metal surface area of catalysts. In this thesis, we only focused on the particle size effects on the properties of support and correlated those properties to the activity of catalysts.

5.2. Perspective for future work

Throughout this work, we correlate the activities of different catalysts to the oxygen vacancies present in them. We measured the concentration of these oxygen vacancies under oxidative and reductive conditions. However, the concentration of vacancy during reaction will be different, as it depends on the rate of reduction step and rate of oxidation step. Hence, in order to form a solid correlation between redox properties and activity, it is really important to measure the vacancy concentration during the catalytic reaction. Raman spectroscopy (3) and XPS under operando conditions can help to measure the actual trend in oxygen vacancy concentration during the reaction. Operando X-ray absorption near edge spectroscopy (XANES) is also a potential candidate, as it measures the Ce^{3+} concentration during the reaction (4). The vacancy concentration measured at the time of reaction will also give a better understanding of the reaction mechanism and rate determining step.

In order to achieve constant particle size, we varied the metal loading on different nano-shapes of CeO_2. However, we also changed the concentration of metal on different CeO_2, which still can influence the activity of catalysts via Ru dissolution in CeO_2. To avoid this, it is recommended to synthesize CeO_2 nano-cubes which has surface area comparable to nano-rods. In fact, some literature has shown microwave-assisted (5) or template-free (6) hydrothermal synthesis approach in CeO_2 nano-shapes with high surface area. This will allow us to use the same concentration of metal without changing particle size. Performance comparison of these type of catalysts will give a better understanding of morphology dependency of CeO_2 nano-shapes.

Addition of another oxide, such as NiO, CuO, Bi_2O_3, and ZrO_2, is known to increase the oxygen vacancies of CeO_2 due to charge difference in cations. Although vacancies generated by Ni^{2+} or Cu^{2+} are redox inactive, as we discussed in chapter 4. However, mixed oxides of CeO_2 with Bi^{3+} and Zr^{4+} cations are more reducible which increases the activity of pristine CeO_2 (7, 8). Therefore, it would be good to check the influence of these cations on the redox properties and performance of CeO_2 nano-shapes.

Identification of metal particle size is a key element of these types of studies. We measured particle size using chemisorption techniques, which gives us the average size of all the metal particles. However, high-resolution TEM analysis with EDX will give a better measurement of particle size together with particle size distribution (9, 10). It will also help to precisely identify the crystal planes present in different shapes of CeO_2. Using advanced TEM microscope we could see step-sites and edge-sites on the metal surface, allowing us to get a better understanding of structure-sensitivity in Ni and Ru catalysts.

As already discussed in the general introduction (Chapter 1), the particle size of active metal is also neglected while studying the structure-dependent activity for various reactions. It would be interesting to check the trend in activities of CeO_2 nano-shapes for reactions like water gas shift and steam reforming of alcohols, keeping the metal particle size constant. It is already seen from Table S1.1 that the variation in metal particle size has resulted in a different trend in activities of CeO_2 nano-shapes for above-mentioned reactions.

After the submission and approval of the thesis, we did additional TEM-EDX and XRD experiments, in order to answer the question raised by one of the referees of our ACS Catalysis paper. New results showed that the averaged Ni particle size reported in the thesis using H_2-TPD is not correct, especially for cube-shaped catalysts. We observed that some bigger particles up to 20nm are also present (Figure 5.1), making the conclusions of chapter 4 incorrect.

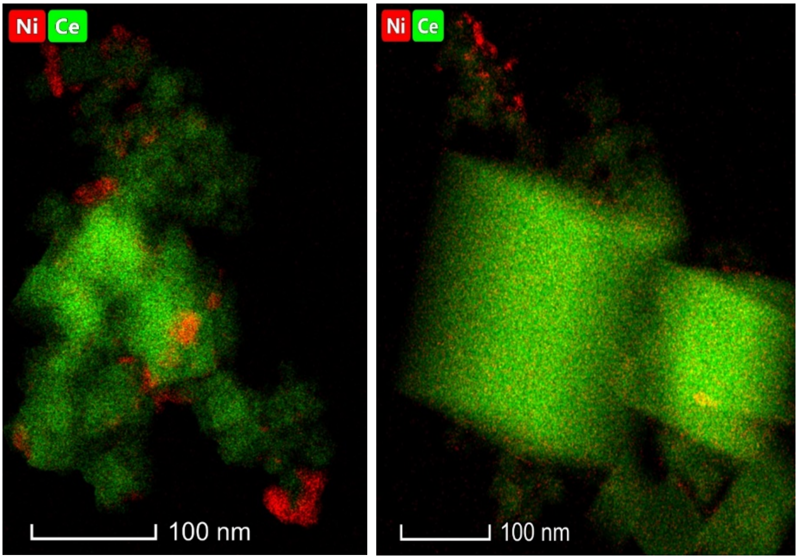

Figure 5.1: TEM-EDX analysis of cube-shaped NiO/CeO_2 catalysts with NiO particles ranging from 5-15nm. NiO loading was 2.7%.

Therefore, we looked at the H_2-TPD profile of each catalyst carefully (figure 5.2) and compared it with the literature. It is reported that (11, 12) the peak centered at 150°C, assigned to the desorption of H_2 on the CeO_2 surface, can influence the dispersion of Ni. Figure 5.2 also shows that the 150°C peak is more pronounced than high-temperature peaks, especially for cube-shaped catalysts. Therefore, it is required to re-interpret the data by neglecting the H_2 adsorption associated with 150°C peak while calculated Ni particle size.

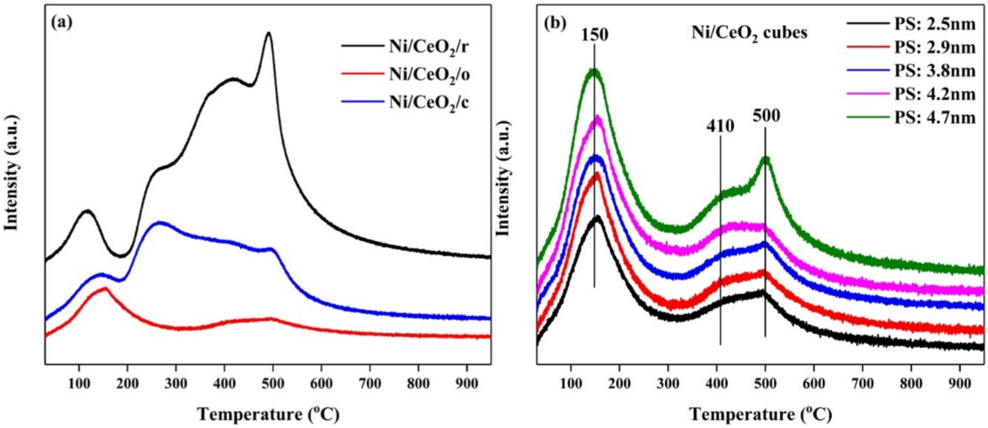

Figure 5.2: H_2-TPD profile of Ni/CeO_2 catalysts with varying CeO_2 morphology (left) and Ni particle size (right).

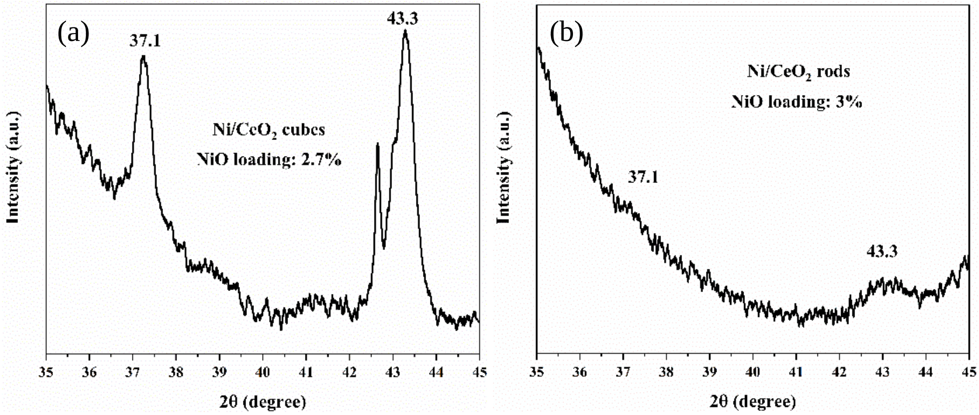

Figure 5.3: XRD patterns of Ni/CeO2 cubes and rods with highest NiO loading of 2.7 and 3% respectively. Scanning steps was ~5000, while scanning time was 5 seconds per step.

We also repeated the XRD analysis with better resolution, in order to improve the NiO signal and calculate it's the crystallite size. XRD of Ni/CeO_2/c (Figure 5.3a) shows two diffraction peaks at around 37 and 43°, assigned to the NiO. The crystallite size calculated using peak broadening was between 15-20nm, consistent with TEM-EDX results. In the case of Ni/CeO_2/r (Figure 5.3b), no clear peaks were observed at 37 and 43°. This implies that the particles of NiO on rods are quite small, though quantitative estimation cannot be done using the XRD. Unfortunately, TEM-EDX for the rod-shaped catalyst is not yet available.

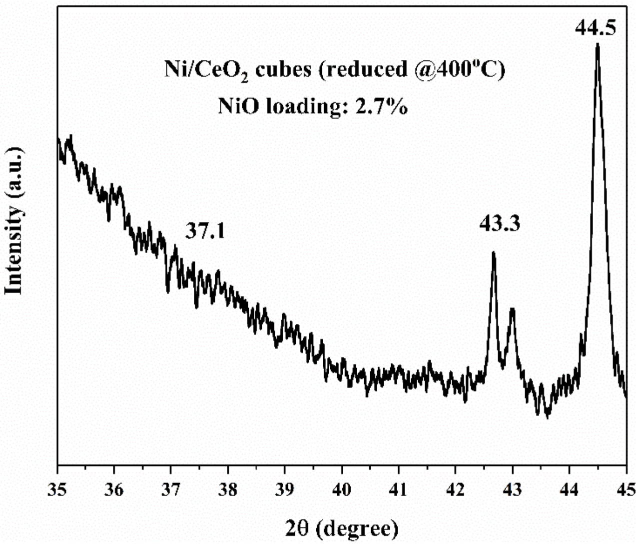

Figure 5.4: XRD patterns of Ni/CeO_2 cubes with NiO loading of 2.7%, after reduction at 400°C. Scanning steps was ~5000, while scanning time was 5 seconds per step.

Another reason behind the discrepancy in the particle size could be the re-dispersion of metal particles during reduction. XRD of cube-shaped catalyst performed after the reduction shows a peak at 44.5° (figure 5.4), with the crystallite size was about 25nm. This confirms that there is no re-dispersion of NiO during reduction. To understand the situation better, we are going to do TEM-EDX and XRD for all other catalysts. We are also going to do the H_2-chemisorption, under static condition, in the University of Cadiz to reconfirm the H_2-TPD data. Furthermore, based on availability, we might also use NO chemisorption and EXAFS analysis to estimate the average Ni particle size.

Based on these result, it is understood that the H_2-TPD results are affected by H_2 adsorption on CeO_2 surface. The impact of this H_2 adsorption the Ni particle size is significant on cube-shape catalysts, while on the rods-shaped catalyst is affected by lesser extent. All in all, it seems that we need to re-interpret the data and change the message of the story before sending the revision of the manuscript. In any case, reliable statistics about the Ni particle size is important to make solid conclusions.

References

1. Fei Wang, Changming Li, Xiaoyu Zhang, Min Wei, David G. Evans, Xue Duan. *J. Catal.* **2015**, 329, 177-186.
2. Zhoufeng Bian, Yi Meng Chan, Yang Yu, Sibudjing Kawi. *Catal. Today*, 10.1016/j.cattod.2018.04.067.
3. Qingyue Wang, King Lun Yeung, Miguel A. Bañares. *J. Catal.* **2018**, 364, 80-88.
4. Fei Wang, Shan He, Hao Chen, Bin Wang, Lirong Zheng, Min Wei, David G. Evans, and Xue Duan. *J. Am. Chem. Soc.* **2016**, 138, 6298-6305.
5. Feng Gao, Qingyi Lu, Sridhar Komarneni. *J. Nanosci. Nanotechnol.* **2006**, 6, 3812-3819.
6. Hepeng Zhang, Bo Yang, Huan Li, Chen Wu, Wenbin Wang, Baoliang Zhang, Qiuyu Zhang, Chongyin Zhang. *Cryst. Res. Technol.* **2018**, 53, 1700233.
7. Martin S. C. Chan, Herme G. Baldovi, J. S. Dennis. *Catal. Sci. Technol.* **2018**, 8, 887-897.
8. Damma Devaiah, Lankela H. Reddy, Sang-Eon Park, Benjaram M. Reddy. *Catal. Rev.* **2018**, 60, 177-277.
9. Sumeya Bedrane, Claude Descorme, Daniel Duprez. *J. Mater. Chem.* **2002**, 12, 1563-1567.
10. Elif Demir, Serdar Akbayrak, Ahmet M. Önal, Saim Özkar. *ACS Appl. Mater. Interfaces* **2018**, 10, 6299-6308.
11. Xin Liao, Yin Zhang, Junqiu Guo, Lili Zhao, Martyn Hill, Zheng Jiang, Yongxiang Zhao. *Catalysts* **2017**, 7(9), 272-286.
12. Karl Sohlberg, Sokrates T. Pantelides, Stephen J. Pennycook. *J. Am. Chem. Soc.* **2001**, 123, 27, 6609-6611.

Scientific Contributions

List of Publications

1. T. Sakpal and L. Lefferts. Structure-dependent activity of CeO_2 supported Ru catalysts for CO_2 methanation. *J. Catal.*, 367, **2018**, 171-180.

2. T. Sakpal and L. Lefferts. Ni/CeO_2 catalysts for CO_2 methanation: effect of CeO_2 morphology and Ni particle size. *ACS Catalysis*, **2019**. (*Under revision*)

3. T. Sakpal and L. Lefferts. CO_2 methanation on Ru/CeO_2 rods: Effect of Ru particle size. (*In preparation)*

Oral Contributions

1. Catalysis and Process Engineering (CPE) cluster meeting. Ni/CeO_2 catalysts for CO_2 methanation: effect of CeO_2 morphology and Ni particle size. University of Twente, **2018**.

2. Netherland's Catalysis and Chemistry Conference (NCCC-XX). Structure-dependent activity of CeO_2 supported Ru catalysts for CO_2 methanation. Noordwijkerhout, **2019**.

Poster Contributions

1. Netherland's Catalysis and Chemistry Conference (NCCC-XVII). Efficient electric energy storage: plasma catalytic approach. Noordwijkerhout, **2016**.

2. Mesa$^+$ day. Activity and stability of ceria supported Ni catalysts in CO_2 methanation using renewable H_2. University of Twente, **2016**.

3. Netherland's Catalysis and Chemistry Conference (NCCC-XVIII). Activity and stability of ceria supported Ni catalysts in CO_2 methanation using renewable H_2. Noordwijkerhout, **2017**.

4. Mesa$^+$ day. Structure dependent activity of CeO_2 supported Ru catalysts for CO_2 methanation. University of Twente, **2017**.

5. Europacat. Structure dependent activity of CeO_2 supported Ru catalysts for CO_2 methanation. Florence, **2017**.

6. Conference on Advances in Catalysis for Energy and Environment (CACEE). Structure dependent activity of CeO_2 supported Ru catalysts for CO_2 methanation. Mumbai, **2018**.

7. Netherland's Catalysis and Chemistry Conference (NCCC-XIX). Structure dependent activity of CeO_2 supported Ru catalysts for CO_2 methanation. Noordwijkerhout, **2018**.

Acknowledgments

January 14, 2015. That's when I first arrived in the Netherlands to start with my Ph.D. There was snow to welcome me at the airport, which I was seeing for the first time in my life for real. Since then it took me 50 months to finish my dissertation. Obliviously one cannot finish a Ph.D. on its own and mine was no different. Therefore, here I am taking this opportunity to thank all the people who have helped me during my journey. 50 months is a long period and I have a weak memory, so if I miss few names please bear with me.

Leon, I owe you many thanks for offering a Ph.D. position in CPM group. The efforts you put in the discussions really helped me to get nice scientific chapters. Your motivation, support, freedom in research, and patience with me is really appreciated. I have learned many things from you which not only improved me as a researcher but also as a person. I will be always grateful to you for that. I also enjoyed the summer bbq at your house every year. I know Ineke is the chief organizer of that event, I am grateful to her too.

I also like to express my gratitude to my graduation committee for reading my work and a fruitful discussion during the defense ceremony. Thank you Prof. Guido Mul, Prof. Andre ten Elshof, Dr. Jimmy Faria, Prof. Emiel Hensen, Prof. Bert Weckhyusen, and Prof. Jan Grunwaldt.

I was fortunate enough to work with three best secretaries CPM have during my stay. Maaike, you helped me a lot at the start of my Ph.D., I will never forget the Christmas we celebrated at your home, thank you for the invitation. Jacqueline, I see you every day on my phone, all thanks to Instagram, Facebook and your passion for photography (You are simply best in it). Thank you for arranging the Copenhagen trip so nicely. The person who always transmits positive vibes is you, Dorothy. You handled the CPM exceptionally well, the group is really going to miss you after you start with your new group. Thank you for looking after me.

Bert also deserves a big share of appreciation. It's not only the technical part, but you helped me a lot with taxation, explaining/filling official paperwork. Your knowledge of the subject and problem-solving skills is phenomenal. Thank you for being supportive and helping me throughout the Ph.D.

Karin and Tom, thank you for all the analysis as well as teaching me the operation of a few techniques. Karin, I enjoyed working with you while fixing Chemisorption machine. You made XRF learning quite easy for me, Tom.

Rico, Mark, and Gerard were my analysis partners from Nanolab. All the data provided by you helped me to get nice chapters. I remember sitting in a dark TEM room for hours to see a few nanoparticles, which really taught me patience. A big thank you to all three of you.

I was fortunate enough to blessed with excellent bachelor students, such as Mark, Alexandra, Rens, and Thomas. You all were really passionate about research and learning. I hope you will do great in your respective career.

CPM has become my family over the years because of its former and current members. Pramod, your every small help at the start of Ph.D. is appreciated. Because of you, I worked a little extra on Saturdays. Thank you, Seshan for the inspiring talks on the coffee table. Kamilla, thank you for introducing me the board games, your Saboteur gift is still my favorite. Roger, the guy who introduced me with the liqueur of god, thank you. Pengyu, thank you for all your help in the lab. A big thanks to you, Maria and Rolf for renovating our house. Shilpa you helped me a lot while scientific discussion as well as teaching me Raman and FTIR setup. Also, thank you and James for all Saturday Badminton. Joline, Sonbo, Marta, Reza, Kaisa, Nuria, Daniel, Pengcheng, Kevin, Shahab, Ratih, Wouter, Danny, Chau – Thank you all. I am grateful for the wonderful moments that we have shared in the lab, at the coffee table, during borrels, group trips, international dinner, and conferences. You all guys made my journey easy with your company. Meeting international people, getting to know them and share a laugh with them are some highlights of these last four years.

A special thanks to my paranymphs, Guido and Rolf. Thank you for arranging fun activities in our group, it helped me to relax. Guido, I am very happy for you and Michela for having a baby. I am sure, you will make a good father. Rolf, you do know a lot of stuff. I learned many new and interesting stories from you, especially history related. And thank you for arranging Sinterklass in our group, I had fun every year.

I would also like to thank my best friends; Mangesh, Durgesh, Hrishikesh, and Nitin for sharing many memories with me for more than 10 years. Thank you Mangesh for your motivation and support during my Ph.D., it means a lot to me. Lalit, thank you for all your help here in the Netherlands and by the way you made that Spain trip unforgettable forever. Pushkar and Prachi, thank you for all the dinners we had, the festival we celebrated and keeping us company.

I cannot thank my parents enough. They are the main source of my inspiration. I have seen their struggles, to some extent, which keeps me motivated whenever I fill down. I thank them for believing in me and giving me all the freedom to pursue my goals. I also thank my brother and sister for their consistent love.

Finally, I thank my adorable wife, Anupriya. You have loved me during my best and worst, I admire that about you. With you, all the problems of my life looked small. Also, you give me the strength to fight against all odds. I am very excited about the next chapter of our life and promised to love you forever.

ISBN: 978-90-365-4781-9